Theory of fast electron transport for fast ignition

2014 Nucl. Fusion 54 054003

(http://iopscience.iop.org/0029-5515/54/5/054003)

IOP Publishing | International Atomic Energy Agency Nuclear Fusion
Nucl. Fusion **54** (2014) 054003 (42pp) doi:10.1088/0029-5515/54/5/054003

Special Topic

Theory of fast electron transport for fast ignition

A.P.L. Robinson[1], D.J. Strozzi[2], J.R. Davies[3], L. Gremillet[4], J.J. Honrubia[5], T. Johzaki[6], R.J. Kingham[7], M. Sherlock[7] and A.A. Solodov[8]

[1] Central Laser Facility, STFC Rutherford-Appleton Laboratory, Harwell Science and Innovation Campus, OX11 0QX, UK
[2] Lawrence Livermore National Laboratory, University of California, PO Box 808, Livermore, CA 94550, USA
[3] Fusion Science Center for Extreme States of Matter, Laboratory for Laser Energetics and Mechanical Engineering, University of Rochester, Rochester, NY 14623, USA
[4] CEA, DAM, DIF, F-91297 Arpajon, France
[5] School of Aerospace Engineering, Technical University of Madrid, Plaza Cardenal Cisneros 3, 28040 Madrid, Spain
[6] Institute of Laser Engineering, Osaka University, 2-6 Yamadaoka, Suita, Osaka 565-0871, Japan
[7] Plasma Physics Group, Blackett Laboratory, Imperial College London, Prince Consort Rd, London, SW7 2BZ, UK
[8] Laboratory for Laser Energetics, University of Rochester, Rochester, NY 14623, USA

Received 4 March 2013, revised 19 August 2013
Accepted for publication 21 August 2013
Published 17 April 2014

Abstract

Fast ignition (FI) inertial confinement fusion is a variant of inertial fusion in which DT fuel is first compressed to high density and then ignited by a relativistic electron beam generated by a fast (<20 ps) ultra-intense laser pulse, which is usually brought in to the dense plasma via the inclusion of a re-entrant cone. The transport of this beam from the cone apex into the dense fuel is a critical part of this scheme, as it can strongly influence the overall energetics. Here we review progress in the theory and numerical simulation of fast electron transport in the context of FI. Important aspects of the basic plasma physics, descriptions of the numerical methods used, a review of ignition-scale simulations, and a survey of schemes for controlling the propagation of fast electrons are included. Considerable progress has taken place in this area, but the development of a robust, high-gain FI 'point design' is still an ongoing challenge.

(Some figures may appear in colour only in the online journal)

1. Introduction

Since its proposal by Tabak and co-workers [198] in 1994 the concept of fast ignition (FI) inertial confinement fusion (ICF) has attracted considerable attention [199]. This advanced ICF concept is appealing because of its ability to achieve high energy gains ($G > 100$) while reducing both the total laser energy and the hydrodynamic demands on the fuel assembly. One of the new challenges in this concept is the need to efficiently couple the ignitor pulse energy via the relativistic (*fast*) electrons to a hot spot in the compressed fuel. Within this, there are two parts—the absorption of laser light into fast electrons, and then the propagation and stopping of the fast electrons. This review is concerned with the latter of these, i.e. fast electron transport (FET).

The FET aspect of FI is challenging for at least three reasons. Firstly there is an issue that would exist even if fast electron propagation were purely ballistic. The size of the hot spot is comparable to the size of the fast electron source (i.e. the laser spot), but the two are separated by a distance which is several times their size. Therefore any appreciable angular spread in the fast electrons must either be mitigated or controlled, as a reduction in the coupling efficiency will otherwise occur. Secondly there is the possibility that various instabilities might disrupt the beam propagation which in turn would impair the coupling efficiency. Thirdly, any solution to the first and second problem must be compatible with achievable fuel assemblies and the fast electron parameters required to achieve stopping in the hot spot. Yet another problem is the source characteristics as a function of the laser

parameters: currently it would appear that the fast electron energy spectrum is too hard to allow for all the fast electrons to be deposited in an ideal hot spot.

Ultimately it is hoped that an overarching solution to these problems can be found which is still attractive and feasible, i.e. a 'point design' for FI. Currently it is not possible to build an ignition-scale facility purely for the purposes of investigating the feasibility of FI or solving the problems associated with FET by purely iterative empirical methods. Therefore detailed numerical simulation and a thorough understanding of the underlying theory are essential parts of realizing FI. Hence the importance of the subject matter of this review.

In this review of the area, we will cover the following aspects of the theory of FET in FI:

(i) *Basic physics*. The fundamental physical processes including scattering and stopping of fast electrons, the role of resistively-generated fields, and key beam–plasma instabilities and phenomena.
(ii) *Simulation methods*. The different simulation methods that have been applied to this problem and their relative strengths and weaknesses.
(iii) *Review of ignition-scale calculations*. A review of simulation studies of the full-scale problem, and how this has informed the overall view of the current challenges that FI is facing.
(iv) *Concepts for controlling transport*. A survey of the various ideas that have been proposed to overcome the limits on the coupling efficiency that are imposed by realistic fast electron divergence angles, namely: fast electron self-collimation by resistively-generated magnetic fields (due to beam profile or resistivity gradients), electrostatic confinement by a vacuum gap (double-cone target), and imposed axial magnetic fields.
(v) *Prospects for a point design*. What future FET studies will have to address in order to move closer to a FI point design.

In addition, we provide a very brief précis of the requirements for fast electron heating to reach ignition in section 2.

Our review will draw attention to the considerable effort that has gone into both understanding the fundamental aspects of the problem and developing numerical tools that are suitable for studying FET. The calculations that have been performed under conditions close to full-scale FI so far clearly show that the scheme must be adapted in some way given realistic fast electron beam (FEB) parameters. Our review also indicates there are potentially feasible ways to 'control' FET and thus achieve a viable point design.

2. Ignition via rapid heating of compressed fuel

So that the FET problem can be put in context, we briefly summarize the objectives that must be achieved in order to obtain ignition and gain from the rapid heating of a particular region of highly compressed DT fuel. FI is an isochoric mode of ignition, where a region of fuel of relatively constant density is heated to much higher temperatures and pressures. It contrasts with isobaric ignition modes, such as central hot-spot ignition. The requirements for FI are determined by hydrodynamics and burn physics. Estimates of the optimal parameters that minimize the ignitor pulse energy have been obtained by Atzeni using both analytic calculation and 2D hydrodynamic simulations [5]. The resulting optimal fast electron energy ($E_{\rm ign}$), fast electron intensity ($I_{\rm ign}$), pulse duration ($t_{\rm ign}$) and hot-spot radius ($r_{\rm hs}$) are

$$E_{\rm ign} = 140\rho_{100}^{-1.85}\,{\rm kJ}, \tag{1}$$

$$I_{\rm ign} = 2.4\times10^{19}\rho_{100}^{0.95}\,{\rm W\,cm^{-2}}, \tag{2}$$

$$t_{\rm ign} = 54\rho_{100}^{-0.85}\,{\rm ps}, \tag{3}$$

$$r_{\rm hs} = 60\rho_{100}^{-0.97}\,\mu{\rm m}, \tag{4}$$

where $\rho_{100} = \rho/100\,{\rm g\,cm^{-3}}$. A typical FI scenario will involve the assembly of a quasispherical DT mass reaching peak densities in the range $300 < \rho < 1000\,{\rm g\,cm^{-3}}$. Assuming that a re-entrant cone-guided FI scheme is being followed, the distance between the tip of the cone and the geometric centre of the DT mass (the 'stand-off' distance) is typically 100 μm. In FI schemes that employ 'hole-boring' to create a path for the ignitor pulse, there will still be a substantial stand-off distance of at least 100 μm. The DT density around the cone tip depends on the detailed hydrodynamics of the fuel assembly scheme, but is usually on the order of at least a few g cm^{-3}. The fuel temperature at stagnation is usually around 200–300 eV. The ignition requirements were generalized in [4] to include effects like $r_{\rm hs}$ exceeding the optimal value and fast electrons not fully stopping in the DT fuel. More recently, ignition requirements based on realistic, PIC-based fast electron sources have been found [12].

The objective of FET theory is to ensure that a hot spot is produced within the constraints of equations (1)–(4) given conditions that do not differ too greatly from those outlined in the preceding paragraph. As direct-drive ICF with central hot-spot ignition may be possible with total laser energies of 1–2 MJ, and advanced indirect-drive ICF may be feasible with similar total laser energy, the FI concepts ideally aim to operate using not much more than 100 kJ of ignitor pulse energy, and around 300 kJ of long pulse energy for fuel assembly. Such a system would give considerably better gain (∼100) for much less capital (3–4 times less). This assumes that 25% of the ignitor pulse energy is coupled to the hot spot. Even if one assumes a 50% conversion into fast electrons, one still needs a 50% coupling efficiency from the generated fast electrons to the hot spot. As this review will proceed to show, this is not a straightforward proposition.

3. Basic physics of FET in FI

We now look at the basic physical phenomena that affect the propagation of the FEB from the source to the compressed core. We will assume that the characteristics of the FEB at the source are given, and concentrate on the theoretical models describing propagation of fast electrons. In this section, phenomena are considered in isolation, concentrating on the fundamental equations and models of each phenomenon. Naturally, the interaction of these phenomena does occur, is rather complex, and requires use of simulation codes for quantitative prediction. However these fundamental elements are the 'building blocks' of FET theory, and are essential for understanding the simulation codes.

3.1. Fast electron parameters

The physics of the absorption of high power, high intensity laser light into the plasma and generation of the FEB is a whole topic in its own right and is covered in detail elsewhere in this special issue. Such details will not be covered, and we limit ourselves to a few general remarks. Broadly speaking, the fast electrons are injected from the laser–plasma interaction (LPI) region (e.g. inner cone surface) towards the compressed fuel core with a broad distribution of energies and a significant degree of anisotropy. A simple model that is sometimes used in transport calculations is

$$f_{\rm inj}(E,\theta) \propto \exp(-E/\bar{E}) \exp\left(-\frac{\theta^2}{2\theta_{\rm inj}^2}\right). \quad (5)$$

$E = m_{\rm e}c^2(\gamma - 1)$ is the fast electron kinetic energy and θ the angle between $\vec{v}$ and the nominal direction of beam propagation.

The mean fast electron energy is often taken to be close to the ponderomotive potential energy, $U_{\rm pond} = [1 + 0.73 I_{18}(\lambda_{\rm L})^2_{\mu{\rm m}}]^{1/2} - 1$ ($I_{18} = I/10^{18}\,{\rm W\,cm^{-2}}$), in such simple models of the fast electron distribution. FET calculations that aspire to have good predictive capability need to include either a self-consistent, laser-generated fast electron source or take a detailed fast electron distribution from a PIC LPI calculation. The ponderomotive scaling does provide a rough indication of the expected fast electron mean energy or temperature with intensity and wavelength, but the detailed scalings are still very much an open topic of research. Detailed PIC simulations often show an energy distribution that is considerably more complex than the exponential in equation (5).

The angular spread of the fast electrons has no simple or clean characterization either, all the more so since it is expected to depend on the electron energy. Even if one neglects the energy dependence, it is virtually impossible to measure $\theta_{\rm inj}$ directly, although experiments have *inferred* a wide range of characteristic angles in addition to a range of simulation results. Current research is tending to operate under the presumption that FI will have to contend with a scenario where the characteristic fast electron divergence half-angle is greater than 30°, and possibly even exceeding 50°–60°.

The conversion efficiency from laser energy to fast electron energy, $\eta_{\rm L}$, is not well characterized either. A wide range of experimental and theoretical results on this were compiled by Davies in [55], who noted that the range of results spanned the range $10 \leqslant \eta_{\rm L} \leqslant 90\%$. Detailed PIC simulations relevant to FI, amongst other results, indicate that achieving a $\eta_{\rm L}$ in the range of 30–50% is likely, thus making an 'attractive' FI scheme still possible provided that efficient coupling to the hot spot can also be achieved.

3.2. Effect of macroscopic EM fields

3.2.1. Return current and current balance. As the FEB propagates through dense plasma, it will draw a *return current* that is both spatially coincident with the fast electron current density $\boldsymbol{j}_{\rm f}$ and which nearly cancels the fast electron current to a good approximation [15], i.e. if the return current density is $\boldsymbol{j}_{\rm b}$ then,

$$\boldsymbol{j}_{\rm f} + \boldsymbol{j}_{\rm b} \approx 0. \quad (6)$$

To see how this arises, one can consider the hypothetical case where there is no return current. For a wide beam, one can estimate the electric field growth from $E \approx -j_{\rm f} t/\varepsilon_0$. Since the current densities in FI can easily reach $10^{16}\,{\rm A\,m^2}$, one can see that the electric field can reach $10^{12}\,{\rm V\,m^{-1}}$ in 1 fs, which is enough to stop MeV fast electrons on a few μm scale. Thus it is clear that a return current will be drawn when the fast electrons propagate through dense plasmas. In a fully 3D situation, one might imagine that the fast electron current is only globally balanced, but not locally balanced (as in equation (6)). However, this will lead to the growth of magnetic fields that would destroy the beam, so the current neutralization must indeed be co-spatial. The return current phenomenon is not particular to FET in the context of ultra-intense laser–plasma physics, and arises in a number of other contexts such as charged particle-beam dynamics [133] and energetic electron transport in solar flares [212].

3.2.2. Resistive inhibition and ohmic heating. Current balance implies that $\boldsymbol{j}_{\rm b} \approx -\boldsymbol{j}_{\rm f}$, and on inserting this into a resistive Ohm's law, one obtains $\boldsymbol{E} = -\eta \boldsymbol{j}_{\rm f}$. The peak resisitivity in many conducting solids will be around $10^{-6}\,\Omega\,{\rm m}$, and even low-Z plasmas at a temperature of a few hundred eV will have resistivities of 10^{-7}–$10^{-8}\,\Omega\,{\rm m}$. This means that the resistively-generated electric field can be 10^8–$10^{10}\,{\rm V\,m^{-1}}$, which is sufficient to inhibit FET significantly.

The drawing of the return current also heats the background plasma via ohmic heating with power density $\boldsymbol{j}_{\rm b} \cdot \boldsymbol{E} \approx \eta j_{\rm f}^2$. From the aforementioned typical values of resistivity and fast electron current density this means that the ohmic heating can heat a solid-density target at a rate of 0.1–1 keV ps^{-1}. Therefore at solid density the ohmic heating must be included in the energy equation of the background plasma, as the heating and thus the effect on resistivity is strong. However at very high density (e.g. DT fuel above $100\,{\rm g\,cm^{-3}}$) this heating is very small, and thus ohmic heating will not make any significant contribution to the generation of the hot spot.

3.2.3. Resistive magnetic field generation. Current balance also has implications for the generation of magnetic field [14]. An improved estimate for the resistive electric field is

$$\boldsymbol{E} = -\eta \boldsymbol{j}_{\rm f} + \frac{\eta}{\mu_0} \nabla \times \boldsymbol{B}. \quad (7)$$

Inserting this into Faraday's law $\partial_t \boldsymbol{B} = -\nabla \times \boldsymbol{E}$ yields

$$\frac{\partial \boldsymbol{B}}{\partial t} = \eta \nabla \times \boldsymbol{j}_{\rm f} + \nabla\eta \times \boldsymbol{j}_{\rm f} + \frac{\eta}{\mu_0}\nabla^2 \boldsymbol{B} - \nabla\eta \times (\nabla \times \boldsymbol{B}). \quad (8)$$

The last two terms correspond to resistive diffusion and resistive advection of magnetic field, and these are the normal terms that are found in the resistive MHD description of a static plasma. The first two terms, on the other hand, correspond to resistive generation of magnetic field, and these are due to the presence of the fast electrons. Davies noted that one can describe the first term as growing magnetic field which pushes fast electrons into regions of higher current density,

whereas the second term grows magnetic field which pushes fast electrons into regions of higher resistivity. These magnetic field growth rates are significant—the magnitude of the growth rate is roughly $\dot{B} \sim \eta j_f / R$ (where R is the FEB radius). Taking some typical figures ($j_f = 10^{16}\,\mathrm{A\,m^{-2}}$, $\eta = 10^{-7}\,\Omega\,\mathrm{m}$, $R = 5\,\mu\mathrm{m}$), yields a growth rate of $2 \times 10^{14}\,\mathrm{T\,s^{-1}}$, i.e. 200 T in 1 ps. Magnetic fields on the order of 100–1000 T will have a significant effect on multi-MeV electrons if the fields extend over several micrometres, insofar as these fields can pinch or filament the beam.

3.2.4. Self-pinching of the FEB. The magnetic field generated by the $\eta \nabla \times j_f$ term in equation (8) grows in the sense which acts to pinch the FEB [52, 202]. The tendency of the beam to self-pinch can, in principle, be highly beneficial to FI. Counteracting against this self-pinching is the angular divergence of the FEB. Bell and Kingham derived a condition for self-pinching or collimation for a plasma with Spitzer resistivity by noting that the self-pinching condition is $R/r_g > \theta_{1/2}^2$ with r_g the electron gyroradius, i.e. the magnetic field can deflect a fast electron through the characteristic fast electron divergence half-angle, $\theta_{1/2}$, in the same distance that it takes the beam radius to double. In the limit of strong heating ($T_b \gg T_{b,\mathrm{init}}$), the Bell–Kingham condition [13] for self-pinching is $\Gamma > 1$ where

$$\Gamma = 0.13 n_{23}^{3/5} Z^{2/5} (\log\Lambda)^{2/5} P_{TW}^{-1/5} T_{511}^{-3/10} (2 + T_{511})^{-1/2} \times R_{\mu m}^{2/5} t_{psec}^{2/5} \theta_{rad}^{-2}, \quad (9)$$

with n_{23} being the background electron density in units of $10^{23}\,\mathrm{cm^{-3}}$, T_{511} being the fast electron energy in units of the electron rest mass, $R_{\mu m}$ being the beam radius in micrometres, t_{psec} is the fast electron pulse duration in ps, and θ_{rad} is $\theta_{1/2}$ in radians. Equation (9) shows that the self-pinching is most strongly dependent on the divergence angle of the fast electrons, with most other parameters exhibiting much weaker dependence. For conditions relevant to FI, self-pinching is marginal and strongly dependent on $\theta_{1/2}$.

3.2.5. Beam hollowing. Even in a uniform density plasma, the $\nabla\eta \times j_f$ term can still have a significant effect. This occurs in the regime of strong heating as this will produce a significant $\nabla\eta$ as the ohmic heating in the centre of the beam is much stronger than at the periphery of the beam ($\propto \eta j_f^2$). This can lead to the sign of $\partial E_x/\partial r$ reversing ($x || j_f$), which leads to the generation of a de-collimating magnetic field in the beam centre. In turn this will lead to the expulsion of fast electrons from the centre of the beam, and this effect is therefore referred to as *beam hollowing*. Davies first identified this effect in [54], where he analysed heating and magnetic field generation in the case of a rigid beam model, and he considered different possible resistivity models via $\eta \propto T_b^\alpha$. When $\alpha < 1$ beam hollowing will eventually occur, as all materials become Spitzer-like ($\alpha = -3/2$) at sufficiently high temperature.

3.3. Drag and scattering of individual fast electrons

Here we will consider the transport of individual fast electrons through plasmas and solids, in other words, we will not consider collective effects arising from the presence of more than one fast electron.

Fast, in this context, refers to an electron traveling at speeds much greater than that of the electrons in the material. In this case, the principal effects on the fast electron are energy loss and angular scattering. We will present expressions for the rate of energy loss, or drag, and the rate of angular scattering and briefly outline their derivations and their implications for FI.

This single particle model will be an adequate description of drag and scattering provided that the fast electron density is much less than the electron density of the material. To determine exactly how much less requires an accurate calculation of collective effects, which we do not have. Work along these lines for the correlated stopping of N fast electrons has been presented in [27, 62]. In the case of a plasma, this effect should be negligible if the separation between fast electrons is greater than the screening length for the fast electron wake. This distance is the dynamical screening length v/ω_p (with ω_p the plasma frequency) for $v \gg (kT_e/m_e)^{1/2}$, and the plasma Debye length $\lambda_D = \sqrt{\varepsilon_0 kT/n_e e^2}$ in the opposite limit. However, there could still be significant electromagnetic fields generated by the collective response of the material to the fast electrons as a whole that can then be considered independently from the drag and scattering. These effects, such as beam–plasma instabilities, are discussed elsewhere in this paper.

We briefly note that drag and scattering have received much attention since the proposal of FI in 1994 [6]. However, calculations of drag date back to the 1930s, with the definitive reformulations of the basic theories being published in the 1950s [69, 195]. These frequently consider the more general problem of drag in matter with bound electrons. Free electrons (namely in conductors) are considered in these calculations, therefore they do apply to plasma. These results are embodied in [100], were recently summarized in [6, 189], and are presented here. The latter two references differ slightly in their angular scattering formulas, and in some details of their logic. For a fully quantum-mechanical (but non-relativistic) treatment of drag due only to free electrons, including both binary collisions and interaction with the plasma medium (e.g. plasmon excitation), see [72].

3.3.1. Drag. The standard expression for the drag on a fast electron in *all* matter (solid, liquid, gas or plasma, conductor or insulator) is [100]

$$\frac{dE}{dt} = -\frac{n_e e^4}{4\pi\varepsilon_0^2 m_e v} L_d, \quad (10)$$

$$L_d = \ln\frac{pv}{\sqrt{\gamma+1}\hbar\omega_p} - \frac{\ln 2}{2} + \frac{9}{16} + \frac{(1/2)\ln 2 + 1/16}{\gamma^2} - \frac{\ln 2 + 1/8}{\gamma}, \quad (11)$$

where E, p and v are the kinetic energy, momentum and velocity of the fast electron, respectively. We have introduced the dimensionless parameter L_d, which we call the drag number. In conventional plasma physics notation it would be called '$\ln\Lambda$'. Bremsstrahlung has been neglected. As would

be expected, fast electron drag does not depend on the velocity or the binding energy of the electrons in the material, since we are considering the limit in which these become negligible. It depends only on their density n_e, which here refers to total, not free, electron density and it is also total density that determines the plasma frequency ω_p in equation (11). The value of $\hbar\omega_p/e$ at the typical solid density of 6×10^{28} atoms m^{-3} is $9.1\sqrt{Z}$ eV, where in this section Z represents nuclear, not ionic, charge. In DT, $\hbar\omega_p/e = 180\sqrt{\rho_{100}}$ eV, where $\rho_{100} = \rho/100\,\mathrm{g\,cm^{-3}}$. This result has been extensively tested in cold matter, but not so extensively in plasma and never at the densities required for FI. However, there is no reason to believe that this lies in a fundamentally different physical regime; drag due to degenerate, free electrons is present in metals.

What changes between materials when applying equation (11) is the implication of *fast*. In plasma, it is sufficient for the fast electron to have a velocity a few times higher than the electron thermal velocity ($\sqrt{kT_e/m_e}$) or the Fermi velocity if the electrons are degenerate. This will be true in the corona and in the core of ignition targets for all cases of interest. In unionized matter, the fast electron must have an energy much greater than any binding energy, so in a cone we will have to consider the effect of electron binding. Before we do this, we will outline the derivation of equation (11) as given in [100].

Fast electron energy loss W above a cut-off W_c is calculated using a binary collision model and energy loss below W_c is calculated using a model for the collective response of the electrons in the material. It is assumed that W_c is much less than the fast electron energy yet much greater than the energy of any individual electron in the material. The cut-off W_c at which the two models are patched together cancels in the final result, giving some confidence that it is accurate, even though neither model is valid for intermediate energy losses, for which no analytical model is available.

For the binary collision model the Møller cross-section is used, an approximate solution to the Dirac equation to order $\alpha v/c$ (the first Born approximation), where α is the fine structure constant, so it includes relativistic effects and quantum spin and exchange effects. Experimentally, deviations from this cross-section have only been detected in close collisions at energies much higher than those of interest here, when radiation becomes important. The target electron is assumed to be stationary, which requires its velocity to be much less than that of the fast electron, and any binding or potential energy is neglected, which requires this to be much less than the energy loss. It is also implicitly assumed that the energy loss occurs largely while the electrons are close together, because the cross-section applies for isolated electrons coming in from infinity and being detected at infinity but is being applied to calculate fast electron energy loss to only one, immediately adjacent electron among many others. Classically, it can be shown that this is an adequate approximation for sufficiently fast electrons by considering interaction over a limited distance [149], and this does not represent a significant additional restriction on the theory. We know of no rigorous demonstration that this carries over to the quantum case. The calculation follows the familiar treatment of binary collisions, with a maximum energy loss of half the fast electron energy, since only the fastest electron is followed, giving

$$L_d|_{W>W_c} = \ln\sqrt{\frac{E}{W_c}} + \frac{9}{16} - \ln 2 + \frac{(\ln 2)/2 + 1/16}{\gamma^2} - \frac{\ln 2 + 1/8}{\gamma}, \tag{12}$$

neglecting terms in W_c/E. The first term would be obtained using the Rutherford cross-section, and the remaining terms represent small quantum corrections due to spin and exchange.

For the model of the collective response of the electrons in the material it is assumed that the fast electron moves at constant velocity and that its electric field causes a small perturbation of the electrons from their equilibrium positions, so a quantum harmonic oscillator model may be used. These are only adequate assumptions far from the fast electron and while its velocity changes on a time scale much slower than the collective response time of the electrons. The final result is

$$L_d|_{W<W_c} = \ln\frac{\sqrt{2m_e v^2 W_c}}{\hbar\omega_p}, \tag{13}$$

which when added to equation (12) yields equation (11). This can be understood in terms of energy exchange to plasma waves (plasmons) in quanta of $\hbar\omega_p$; that this arises from a quantum treatment of electron oscillations in a plasma, which has been considered by a number of authors [21, 72, 153], is not surprising. What is remarkable is that this also arises as the limiting form for fast electrons from a general treatment, including electron binding.

We will now consider the more general case where the binding energies of the electrons in the material cannot be neglected, since this will be the case in a cone. This leads to the drag being reduced. For a combination of historical and mathematical reasons the energy loss due to the collective response of the material is artificially divided into two parts and written

$$L_d|_{W<W_c} = \ln\frac{\sqrt{2p^2W_c/m_e}}{I_{ex}} - \frac{1}{2}\frac{v^2}{c^2} - \frac{\delta}{2}, \tag{14}$$

giving

$$L_d = \ln\left(\sqrt{\gamma+1}\frac{E}{I_{ex}}\right) - \frac{\ln 2}{2} + \frac{1}{16} + \frac{(1/2)\ln 2 + 9/16}{\gamma^2} - \frac{\ln 2 + 1/8}{\gamma} - \frac{\delta}{2}. \tag{15}$$

The first part is given by the first two terms of equation (14), the basis for which was published by Bethe in 1930 (in German). It gives the energy transferred to the excitation of electrons by the electric field of a charged particle moving at constant velocity. The complexities of dealing with coupled, quantized oscillations of multiple bound electrons are hidden in I_{ex}, known as the mean excitation potential, for which there exist a variety of theoretical models. In very general terms it can be written as

$$\ln I_{ex} = \sum_{i,j} f_{ij}\ln(E_j - E_i), \tag{16}$$

a weighted sum over all possible transitions of electrons in the material from initial energy E_i to final energy E_j, f_{ij} being

the transition probability. In the simplest possible case of a single, undamped, harmonic oscillator of frequency ω it is $\hbar\omega$. This is a good approximation for plasma, giving the mean excitation potential to be $\hbar\omega_\mathrm{p}$. The values normally used for unionized materials are determined by measurements of either ion or electron energy loss or of optical absorption, as drag can be treated in terms of the absorption of a virtual photon field. Thus it becomes a free parameter used to fit experimental data. The reference values are those published in [100], available online at [17]. For elements these can be adequately fitted by $9.43Z + 26.1$ eV, except for hydrogen, where I_ex/e is 19.2 eV. For compounds, the stopping due to its constituents can be added since chemical structure has been found to have only a small effect on the mean excitation potential. The second part is the δ, first quantified by Fermi in 1940 [71] using a purely classical calculation representing the electron response with a single, harmonic oscillator. It gives a reduction in the energy loss due to the electric field of the fast electron being shielded by the collective response of the electrons in the material, an effect neglected by previous treatments, hence the convention of a negative sign (the factor of 2 is another, rather confusing, convention). It is called the density effect correction because it increases with electron density. The mathematical reason behind this division is the difficulty of giving a straightforward expression for δ in the general case of multiple bound electrons. It can be obtained analytically in the limit of a strongly relativistic electron [71]

$$\delta \to 2\ln\left(\frac{\gamma\hbar\omega_\mathrm{p}}{I_\mathrm{ex}}\right) - \frac{v^2}{c^2} \qquad v \to c, \tag{17}$$

giving the general result for fast electron drag that we started with. For plasma, where $I_\mathrm{ex} = \hbar\omega_\mathrm{p}$, this expression is valid for all cases of interest. For bound electrons, where typically $I_\mathrm{ex} \gg \hbar\omega_\mathrm{p}$, this expression is only greater than 0 for $\gamma > 1.65 I_\mathrm{ex}/\hbar\omega_\mathrm{p}$. In practice, $\gamma \gg 1.65 I_\mathrm{ex}/\hbar\omega_\mathrm{p}$ is required for equation (17) to be a good approximation for bound electrons. In solid gold, for example, this requires a fast electron energy much greater than 8 MeV.

Sternheimer has given a simple, approximate formulation of the density effect [194] that is used in [100], which we will write as

$$\delta = \sum_n f_n \ln\left[1 + \frac{E_l^2}{f_\mathrm{S}^2 B_n^2 + f_\mathrm{B} f_n (\hbar\omega_\mathrm{p})^2}\right] - \left(\frac{E_l}{\gamma\hbar\omega_\mathrm{p}}\right)^2, \tag{18}$$

where f_n is the fraction of electrons with binding energy B_n (Sternheimer writes this as h times the frequency of the absorption edge), f_B is 1 if $B_n = 0$ (free electrons) and 2/3 otherwise, E_l is given implicitly by

$$\sum_n \frac{f_n(\hbar\omega_\mathrm{p})^2}{f_\mathrm{S}^2 B_n^2 + E_l^2} = \frac{1}{(p/m_\mathrm{e}c)^2} \tag{19}$$

and the Sternheimer factor f_S is given implicitly by

$$\sum_n f_n \ln\left[f_\mathrm{S}^2 B_n^2 + f_\mathrm{B} f_n (\hbar\omega_\mathrm{p})^2\right] = \ln I_\mathrm{ex}^2, \tag{20}$$

which ensures that equation (17) is obeyed with experimental values of the mean excitation potential, a consistent problem with other formulations. The Sternheimer factor is typically between 1.5 and 2.5 [194].

For plasma ($B = 0$, $f_\mathrm{B} = 1$) equations (18) and (19) give the density effect correction to be $2\ln(\gamma) - v^2/c^2$ and equation (20) simply gives the mean excitation potential to be $\hbar\omega_\mathrm{p}$, reproducing results we have seen before.

To illustrate the result for bound electrons let us consider a single binding energy, for which it is straightforward to obtain

$$\delta = \ln\left[(\gamma^2 - 1/3)\left(\frac{\hbar\omega_\mathrm{p}}{I_\mathrm{ex}}\right)^2\right] - \frac{v^2}{c^2} + \left(\frac{f_\mathrm{S} B}{\gamma\hbar\omega_\mathrm{p}}\right)^2 \quad \text{if } \frac{p}{m_\mathrm{e}c} > \frac{f_\mathrm{S} B}{\hbar\omega_\mathrm{p}}, \tag{21}$$

$$= 0 \quad \text{otherwise } \frac{p}{m_\mathrm{e}c} \leqslant \frac{f_\mathrm{S} B}{\hbar\omega_\mathrm{p}}. \tag{22}$$

This shows that there is a threshold fast electron energy for the density effect to occur in insulators (conduction electrons are treated as free electrons) and that $p/m_\mathrm{e}c$ should exceed $f_\mathrm{S} B/\hbar\omega_\mathrm{p}$ for all electrons before equation (11) will be a good approximation, a similar constraint to that indicated by equation (17). For multiple binding energies a numerical solution is required.

Sternheimer [194] gives a five parameter fit to the density effect correction for numerous elements and compounds. We have found that for Cu and Mo the overall drag number from [100] is reproduced to within 1% by just using

$$\frac{\delta}{2} = \ln\left[1 + \frac{E}{m_\mathrm{e}c^2}\frac{\hbar\omega_\mathrm{p}}{I_\mathrm{ex}}\exp(-0.5)\right], \tag{23}$$

which reproduces the limiting forms of the density effect correction, but does not fit at intermediate energies. However, here the density effect correction makes a negligible contribution to the drag number. This approach could be adapted for insulators with a threshold energy E_0 by using

$$\frac{\delta}{2} = \ln\left[1 + \frac{E - E_0}{m_\mathrm{e}c^2}\frac{\hbar\omega_\mathrm{p}}{I_\mathrm{ex}}\exp(-0.5)\right] \qquad E \geqslant E_0, \tag{24}$$

but we have not verified the accuracy of this approach.

What is lacking are results for partially ionized matter when the electron is not fast enough for equation (11) to apply. The only treatment we are aware of is an approximate model for the mean excitation potential of bound electrons in an ion, published in a difficult to obtain report by More [136], the drag number of the free electrons being given by equation (11). For the mean excitation potential he used a simplified theoretical model known as the local plasma approximation

$$\ln I_\mathrm{ex} = \int f_\mathrm{e}(\vec{r}) \ln[\hbar\omega_\mathrm{p}(\vec{r})]\,\mathrm{d}V, \tag{25}$$

where f_e is the electron probability density function and $\omega_\mathrm{p}(\vec{r})$ refers to the plasma frequency at the local mean electron density $N_\mathrm{e} f_\mathrm{e}$, N_e being the number of electrons. In this approximation the mean excitation potential of bound electrons is higher than that of free electrons because they are concentrated around the nucleus. To obtain the electron distribution around an ion More used the Thomas-Fermi model and found that the result could be described by

$$I_\mathrm{ex}(q) = I_\mathrm{ex}(0)\frac{\exp(1.29(q/Z)^{0.72-0.18q/Z})}{\sqrt{1 - q/Z}}, \tag{26}$$

where q is the ionization state. This should be an adequate description for weakly ionized many electron atoms when the interaction between electrons of neighbouring ions is negligible. It does not give the correct result for hydrogen-like ions, which would be expected to have a mean excitation potential of roughly Z^2 times the value for hydrogen; More argues that the contribution of this one electron will, in general, be negligible. Equation (26) could also be used to estimate the density effect for the bound electrons by using equation (20) to calculate a new effective value of f_S from the new value of I_{ex}, representing an average increase in binding energies, or by using our crude model. Binding energies of ions can be measured or calculated, but a limited number of results are available and no one appears to have made the effort to apply these to calculating fast electron drag. The mean excitation potential and density effect correction will also have to be recalculated for compressed material, such as a cone tip in a compressed target. The simplest approach would be to start from equation (20) to reevaluate the mean excitation potential.

3.3.2. Scattering. In solids where scattering is from atoms with a radius a much less than the interatomic separation and the de Broglie wavelength of the fast electron is much less than a, it is clear that angular scattering can be adequately described in terms of binary collisions. An approximate model for the average potential around an atom is the familiar exponentially screened potential with a screening distance a [101, 140]. Measured and calculated values of atomic radii are readily available for all elements; the Thomas–Fermi model gives a simple, general result of $a_0/Z^{1/3}$, where a_0 is the Bohr radius (5.3×10^{-11} m), although this is not accurate for all elements. Using the scattering cross-section for an exponentially screened potential obtained from the Dirac equation in the first Born approximation [6, 140], the familiar treatment of binary collisions, integrating over *all* scattering angles, 0 to π, gives

$$\frac{\mathrm{d}\langle\theta^2\rangle}{\mathrm{d}t} = \frac{Zn_e e^4}{2\pi\varepsilon_0^2 p^2 v} L_s, \tag{27}$$

$$L_{s-a} \approx \ln\frac{2ap}{\hbar} - 0.234 - 0.659\frac{v^2}{c^2} \qquad \frac{2ap}{\hbar} \gg 1, \tag{28}$$

where $\langle\theta^2\rangle$ is the mean square scattering angle with respect to the electron's instantaneous (not original) direction of motion, and we have introduced the scattering number L_s with the $-$a indicating that it applies to atoms. The last term, which is due to the electron spin, had to be evaluated numerically, so all terms have been expressed to the same accuracy of three significant figures. This differs slightly from the expression in [6] because they calculated $\langle\cos\theta\rangle$ not $\langle\theta^2\rangle$. The integral does not diverge at zero scattering angle (infinite impact parameter) because in quantum mechanics any potential that falls faster than $1/r$ has a finite cross-section for zero scattering angle [101]. Here this cross section is approximately $\pi[2Z\alpha a/(v/c)]^2$ for $2ap/\hbar \gg 1$, which surprisingly gives an effective upper impact parameter that is smaller than the screening distance a. Since close collisions are not modified, using a screened potential in place of the Møller formula to calculate the drag number would make no significant difference.

The accuracy of the first Born approximation for the exponentially screened potential has been carefully analysed by Joachain [101]. He found that it is only accurate to order $\ln(ap/\hbar)Z\alpha/(v/c)$ and only converges for $ap/\hbar \gg 1$ (hence our use of this limit), which are quite severe limitations. However, his comparison with more accurate solutions shows that what this approximation misses are oscillations in the cross-section and that it is accurate for small-angle scattering. Since we are only interested in the mean scattering angle and the most important factor is the cross-section for zero scattering, this approximation should not lead to significant errors, with the usual provisos that the fast electron energy is high enough for it not to have bound states and low enough that radiation is not important.

In plasmas, following the treatment used for the drag term, we should only use binary collisions above some scattering angle θ_c and a statistical treatment of the electric field due to random, thermal fluctuations from charge neutrality below θ_c; hopefully θ_c will cancel out. However, there does not exist an adequate model for the effect of distant charge fluctuations; all existing models do not deal adequately with interparticle correlations due to the electrostatic field and do not include quantum effects, which we have seen to be important for distant interactions. The inclusion of fluctuations (Langmuir wave emission) in the stopping power, but not in angular scattering, means that the two do not satisfy an Einstein relation, which would be obtained if both followed from a sequence of small, uncorrelated momentum kicks (e.g. a Langevin model). The best approach appears to be to use equation (28) with the Debye length in place of the atomic radius, giving

$$L_{s-i} \approx \ln\frac{2\lambda_D p}{\hbar} - 0.234 - 0.659\frac{v^2}{c^2} \qquad \frac{2\lambda_D p}{\hbar} \gg 1, \tag{29}$$

where the $-$i indicates that it applies to ions. We will now briefly review the theoretical models that lead us to this conclusion, in historical order.

Landau [23] used a series of coupled kinetic equations for joint probability densities and set the 3-body joint probability density to zero, because it cannot be solved, and obtained an approximate solution for the 2-body joint probability density in equilibrium, neglecting particle motion. This showed that pairs of particles interact via the exponentially screened potential, but does not prove that interactions in a plasma can be reduced to sums over pairs of particles; rather it assumes this. Pines and Bohm [154] used Fourier transforms of individual particle positions, but used the random phase approximation, which is equivalent to assuming that the particles are uncorrelated. Their treatment went beyond that of Landau by considering the effect of particle motion, showing that the exponentially screened potential is only accurate for particles with velocities below the thermal velocity. Faster particles show reduced, asymmetric screening, for which an analytic solution cannot be obtained, but numerical solutions have been published by a number of authors [60, 66, 215]. Several authors have used the Holtsmark distribution for the distant interactions [40, 80], which describes the electric field due to a completely random distribution of stationary point charges. This diverges, so an upper cut-off has to be introduced. It shows that the net effect of a completely random distribution of charges is the same as summing the effect of individual binary collisions with each particle. In practice, not all distributions are possible because some will have an electrostatic potential energy higher than the total energy of the system. The Debye length, or something

close to it, then appears as the natural cut-off because it gives the distance over which deviations from charge neutrality will give an electrostatic potential energy of the order of the thermal energy. Spitzer used two different models [44]. First, he calculated the random fluctuations in the electric field at a point by applying Poisson statistics to the charged particles in a sphere surrounding it. Like the Holtsmark distribution, this assumes a completely random distribution of point charges so diverges as the size of the sphere considered tends to infinity and again the Debye length appears as the natural order of magnitude for a cut-off to prevent this divergence. He then considered the autocorrelation function of the electric field for charged particles moving in straight lines, which yet again neglects interparticle correlations and again diverges, but this time a cut-off in correlation time is needed. He used $1/\omega_p$, giving much the same result as a spatial cut-off at λ_D in his first model. This gives a slightly different physical picture, with distant interactions being curtailed due to the limited lifetime of fluctuations from charge neutrality. A treatment in terms of dipoles has also been tried, but not published, and also diverges, although this would not be the case if a quantum treatment had been used.

In summary, these models indicate two practical approaches:

(i) Sum partial binary collisions over a distance of the order of the Debye length, in effect a $1/r$ potential cut at the Debye length.
(ii) Sum full binary collisions with all particles using the screened potential.

We used approach (ii) principally because it is more elegant. It also seems reasonable to assume that ions move completely at random, which allows us to reduce the many-body problem to a sum of binary interactions when considering the mean effect of many interactions, because electrons will move to cancel any charge build up before the ions are significantly affected by their mutual electrostatic field. The imperfect nature of this neutralization due to the thermal motion of the electrons is accounted for by using the Debye screened potential, which will apply to the vast majority of the ions since they have velocities less than the electron thermal velocity.

These considerations also lead us to exclude ion shielding in the Debye length, which is sometimes included by using $\sqrt{\varepsilon_0 kT/(Z+1)n_e e^2}$ in place of $\sqrt{\varepsilon_0 kT/n_e e^2}$, a conclusion that has been supported by results from numerical modelling [64]. The Debye length will have to be modified for degenerate electrons. A crude approximation is to replace the temperature with $\sqrt{kT^2 + E_F^2}$ where E_F is the Fermi energy [123].

Unfortunately, it appears that approach (i) will give significantly greater scattering than approach (ii) because the quantum-mechanical result for the screened potential effectively cuts off the interaction at a distance significantly less than the Debye length (the finite cross-section of $\pi[2Z\alpha a/(v/c)]^2$ for zero scattering). A proper quantum treatment of approach (i) is really required, but we can resort to the uncertainty principle to iron out this difference; we are considering the interaction of the electron with particles within a region of size λ_D so they can be attributed a minimum momentum spread of order $\hbar/2\lambda_D$. Interpreting this as imposing a minimum scattering angle and using the small-angle approximation gives $\theta_{min} \sim \hbar/2p\lambda_D$. Using this cut-off with the scattering cross-section for a $1/r$ potential obtained from the Dirac equation in the first Born approximation (the Mott formula [139]) actually leads to a scattering number slightly smaller than approach (ii), but the difference is not significant given the crude approximation being used.

We will now consider scattering from electrons, which is normally ignored because it is only significant in hydrogen. It is not the same as scattering from ions because the maximum energy exchange of half the fast electron energy gives a maximum scattering angle of $\sin^{-1}\sqrt{2/(\gamma+3)}$ and the physical considerations that led us to sum binary collisions with all atoms and ions using a screened potential would not appear to apply to electrons. For the case of atoms, it seems clear that the electrons do not share the same screened potential and that scattering from electrons will only occur while the fast electron is inside the atom; the mean effect of the electrons on the total potential has been included in the screened potential and we just need to add the effect of the irregularities in the potential apparent close to electrons. For the case of a plasma, we cannot apply the same argument that electrons are free to move at random and the Debye (static) screened potential will not apply to most electrons. The contribution of the electrons to the effect of distant charge fluctuations would appear to have been included in the screened potential used for the ions, so we just need to include scattering due to the random thermal motion of nearby electrons. This amounts to saying that approach (i) is more adequate for electrons, with the atomic radius replacing the Debye length for atoms. However, we have already argued that both approaches should give comparable results, therefore an adequate approximation for electrons should be to account only for the reduced maximum scattering angle, giving

$$L_{s-e} \sim L_s - \frac{1}{2}\ln\frac{\gamma+3}{2}. \tag{30}$$

The final expression for scattering rate can be written

$$\frac{d\langle\theta^2\rangle}{dt} \approx \frac{n_e e^4}{2\pi\varepsilon_0^2 p^2 v}\left[(Z+1)L_s - \frac{1}{2}\ln\frac{\gamma+3}{2}\right], \tag{31}$$

with L_s given by equation (28) for unionized material and by equation (29) for fully-ionized material. In [6] scattering from electrons was dealt with using an exponentially screened potential and the result does not differ significantly.

As with the drag term, we lack results for partially ionized material. In the absence of a better treatment, we suggest summing scattering by the ion charge q with a screening distance given by the Debye length for the free electrons $\lambda_D(q)$ and scattering by the full nuclear charge Z with a screening distance given by the ion radius $a(q)$. This amounts to replacing the screening distance in either equation (28) or equation (29) with $\lambda_D(q)^{q/Z}a(q)$, so as we are only modifying the argument of a logarithm the approximation does not have to be particularly good. Ion radii for low values of q are available and for hydrogen-like ions it is a_0/Z, but values for intermediate ionization states are not readily available.

3.3.3. Implications of drag and scattering for FI. We are interested in FET in compressed DT plasma and, for cone-in-shell FI, in the cone material, for which gold has been

the preferred candidate. When the ignition laser is fired the cone tip will have been heated and shock compressed, so it is not entirely accurate to treat it as a cold solid, but we will use these values as an estimate.

The quantity of principal interest arising from the drag is the stopping distance. Assuming the drag number is a constant we can obtain this analytically;

$$s = \frac{4\pi\varepsilon_0^2}{n_e e^4 L_d}\frac{E^2}{\gamma}. \tag{32}$$

It is tempting to use the relativistic limit $s \propto E$, but for this to be within 10% of the result from the full expression requires energies greater than 4.6 MeV, so for most cases of interest the full expression should be used.

Numerical calculations of stopping distances in cold matter are tabulated in [100] and are available online [17]. As an example, a 1 MeV electron can penetrate up to 400 μm of gold ($\rho s = 0.77\,\mathrm{g\,cm^{-2}}$), so stopping should not be an issue in the cone. These calculations also include bremsstrahlung, which allows us to determine when this is indeed negligible. In hydrogen energy loss to bremsstrahlung (radiation yield) only exceeds $0.1E$ for $E > 100$ MeV, while in gold this is reached for $E > 2$ MeV. It is undesirable for an ignition design to have a significant number of electrons above 1 MeV stopping in a cone, so bremsstrahlung should never be a significant energy loss mechanism.

Fast electron stopping in compressed DT plasma has been considered using equation (11) in [6]. They give an approximate expression for the stopping distance:

$$\rho s \approx 1.94\frac{E_{\mathrm{MeV}}^2}{1+1.96E_{\mathrm{MeV}}}\rho_{100}^{0.066}\,\mathrm{g\,cm^{-2}}, \tag{33}$$

which was found to be within 10% of a numerical solution of equation (10) for energies from 1 to 10 MeV and DT mass densities from 300 to 1000 $\mathrm{g\,cm^{-3}}$. As an example, at 400 $\mathrm{g\,cm^{-3}}$ a stopping distance less than 1.2 $\mathrm{g\,cm^{-2}}$ requires an energy less than 1.5 MeV.

Scattering leads to an undesirable increase in the angular spread of electrons, which could be quite serious in the tip of a high-Z cone. While energy loss remains negligible, the accumulated root-mean-square scattering angle over a path length s is given by

$$\langle\theta^2\rangle^{1/2} \approx \frac{Ze^2}{\varepsilon_0 pv}\sqrt{\frac{n_a s L_s}{2\pi}}, \tag{34}$$

where n_a is atom number density. If we wish to maintain this below, say, 45° ($\pi/4$) for a 1 MeV electron then for solid gold, tip thickness should be less than 13 μm ($\rho s = 0.025\,\mathrm{g\,cm^{-2}}$). Even if the *spatial* spread of electrons is reduced by a collimating magnetic field or vacuum gaps this will not reduce the angular spread, so as soon as the collimating effect ends the electrons will diverge. This indicates that a lower Z cone tip would be desirable, because even taking into account that thickness should then be increased to avoid shock break out roughly as $Z^{-1/2}$, the net angular scattering will still vary as $Z^{3/4}$.

The effect of scattering on ignition requirements for an initially parallel beam of electrons entering a uniform sphere of compressed DT plasma has been considered in [6] using a Monte Carlo model. They found that it led to a 10–20% increase in the energy requirement.

3.4. Beam-plasma instabilities

3.4.1. Motivation. Electron beam–plasma instabilities are a long-standing field of plasma physics [51]. It was early understood that, for a broad parameter range, the beam-driven excitation of plasma waves can lead to energy and momentum transfer rates between the incident beam and the ambient plasma largely exceeding classical (collisional) values [35, 49, 70, 122, 137, 145, 147, 164, 207]. Such 'anomalous' relaxation or scattering processes underlie many scenarios of intense electron beam transport in laboratory [125, 176] or space [1, 132, 141] plasmas. For instance, they were at the basis of the pioneering concept of electron beam-driven fusion explored in the 1970s and 1980s [98, 117, 133, 138, 197, 206, 207]. Because it relies upon the propagation and dissipation of an intense electron current into a large-scale plasma, the fast ignition scheme (FIS) has spurred renewed interest in this topic.

The influence of microscopic beam–plasma instabilities in the FIS could be twofold. First, the magnetic turbulence generated by a Weibel-like instability [77, 216] in the laser-absorption region tends to isotropize the fast electrons through random deflections [2]. As a result, the electrons are injected into the target with a large angular spread, which severely constrains the beam energy required for ignition: according to Atzeni *et al* [7], the ignition energy increases from ~25 kJ to ~50 kJ when the half-angle divergence of the electron source increases from 20° to 40°. Second, the variety of instabilities arising during the beam transport could entail an enhanced stopping power which could relax the ignition requirements (e.g. [222]). Assuming the beam electrons' mean energy, $\langle E_b\rangle$, obeys the ponderomotive scaling [219], the laser ignition energy, E_L, is predicted to vary as [4]

$$E_L \geqslant 93\left(\frac{\rho}{300\,\mathrm{g\,cm^{-3}}}\right)^{-0.9}\left(\frac{f_{\mathcal{R}}\lambda_0}{0.5\,\mu\mathrm{m}}\frac{0.25}{\eta_L}\right)^2\,\mathrm{kJ}, \tag{35}$$

where ρ is the DT core density, λ_0 the laser wavelength, η_L the laser-to-electron coupling efficiency and $f_{\mathcal{R}}$ a parameter (close to unity in the collisional regime) quantifying the effective beam range:

$$\rho\mathcal{R} = 0.6 f_{\mathcal{R}}\langle E_b\rangle\,\mathrm{g\,cm^{-2}}. \tag{36}$$

The question therefore arises as to whether the excitation of beam–plasma instabilities may entail $f_{\mathcal{R}} \ll 1$ so as to significantly decrease E_L. This could proceed either directly, through the unstable wave-beam interaction [125], or indirectly, through an instability-induced increased plasma resistivity [176].

In contrast to past studies, which mostly focused on electrostatic beam-aligned instabilities, recent FIS-related theoretical works have considered the whole unstable $\boldsymbol{k}$-spectrum [28, 29, 31–34, 37, 45, 83, 107], paying particular attention to the quasi-magnetic filamentation modes developing normal to the beam direction [2, 38, 90, 92, 108, 110, 113, 127, 150, 156, 174, 177, 182, 183, 201, 211]. Being all the stronger when the beam and plasma densities are comparable [32], the collisionless instabilities are most likely to disrupt the early propagation of the beam into the 'low'-density regions of the

target. Note, however, that from the optimal beam intensity found in [5], the beam density is expected to be

$$n_\mathrm{b} \sim 8\times10^{21}\left(\frac{\rho}{100\,\mathrm{g\,cm^{-3}}}\right)\left(\frac{\langle E_\mathrm{b}\rangle}{1\,\mathrm{MeV}}\right)^{-1}\mathrm{cm^{-3}}. \quad (37)$$

Given such extreme values, collisionless instabilities may arise up to solid densities, depending on the background collisionality. This encompasses the laser-absorption region, the cone tip (if any) and part of the DT plasma. Most of these microscopic processes, however, should be quenched in the resistive regime treated in section 3.2, so that macroscopic resistive fields should then rule the beam transport. An exception is the filamentation instability which may survive in strongly-collisional plasmas, albeit confined at longer wavelengths. Close to the core ($\rho \geqslant 100\,\mathrm{g\,cm^{-3}}$), collisional drag and scattering effects dominate the beam transport.

3.4.2. Main instability classes and their related properties. Unless otherwise noted, we shall restrict our review to uniform, infinite and initially field-free 2D beam–plasma systems. The most general (kinetic) description is afforded by the relativistic Vlasov–Maxwell equations, whose linearization yields the following dispersion relation for electromagnetic perturbations $\propto \mathrm{e}^{\mathrm{i}(\boldsymbol{k}\cdot\boldsymbol{x}-\omega t)}$ [99]

$$\left(\omega^2\epsilon_{zz}-k_x^2c^2\right)\left(\omega^2\epsilon_{xx}-k_z^2c^2\right)-\left(\omega^2\epsilon_{xz}+k_xk_zc^2\right)^2=0, \quad (38)$$

where the dielectric tensor elements read

$$\epsilon_{\alpha\beta}(\boldsymbol{k},\omega)=\delta_{\alpha\beta}+\sum_j\frac{\omega_{pj}^2}{\omega^2}\int\int\int \mathrm{d}^3p\,\frac{p_\alpha}{\gamma(\boldsymbol{p})}\frac{\partial f_j^{(0)}}{\partial p_\beta}$$
$$+\sum_j\frac{\omega_{pj}^2}{\omega^2}\int\int\int \mathrm{d}^3p\,\frac{p_\alpha p_\beta}{\gamma(\boldsymbol{p})^2}\frac{\boldsymbol{k}\cdot\left(\partial f_j^{(0)}/\partial\boldsymbol{p}\right)}{m_j\omega-\boldsymbol{k}\cdot\boldsymbol{p}/\gamma(\boldsymbol{p})}. \quad (39)$$

Here, $\boldsymbol{k}=(k_x,k_z)$ is the real wave number, z is the direction of beam propagation, ω is the complex frequency, $\omega_{pj}=(n_je_j^2/m_j\epsilon_0)^{1/2}$ is the plasma frequency of species j and $\gamma(\boldsymbol{p})=[1+(p/m_jc)^2]^{1/2}$ is the Lorentz factor. In the following, the index $j=(b,p)$ stands for the electron beam and plasma components. Collisional effects are neglected at this stage and will be discussed in section 3.4.3. The main ingredient in (39) is the unperturbed distribution function $f_j^{(0)}(\boldsymbol{p})$. In the context of the FIS, there is no obvious physical reason supporting a particular model distribution for the beam electrons. A variety of descriptions can be found in the literature, ranging from monokinetic [20, 150] to Maxwellian-like [203, 204, 226, 227] through waterbag [30, 45, 83, 183, 225] and Kappa [121] distributions. However, in order to address potentially large (relativistic) thermal spreads, it appears convenient to model the beam–plasma system by means of drifting Maxwell–Jüttner distribution functions [105, 221]

$$f_j^{(0)}(\boldsymbol{p})=\frac{\mu_j}{4\pi m_jc^3\gamma_j^2K_2(\mu_j/\gamma_j)}$$
$$\times\exp\left[-\mu_j\left(\gamma-\beta_j\frac{p_z}{m_jc}\right)\right], \quad (40)$$

where $\beta_j=\langle p_z/m_j\gamma c\rangle$ is the z-aligned mean drift velocity, $\gamma_j=(1-\beta_j^2)^{-1/2}$, $\mu_j=m_jc^2/T_j$ is the normalized inverse temperature and K_2 is a modified Bessel function. Two arguments can be made for this model distribution. First, it permits an exact resolution of the 2D fully relativistic spectrum at an affordable numerical cost [32]. Second, it has been shown, under certain conditions, to model with some accuracy the relativistic electron phase space observed in laser–plasma simulations [45]. Care must be taken, though, in the numerical evaluation of equations (39) and (40) in the complex ω-plane as detailed in [33].

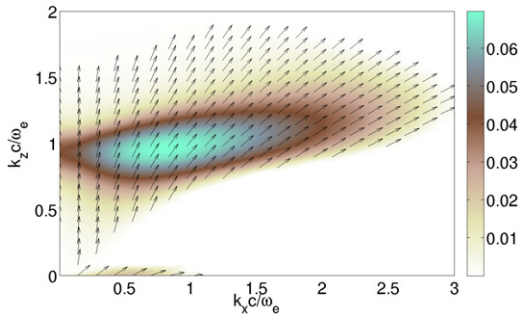

Figure 1. Overlay of the normalized growth rate $\delta=\Im\omega/\omega_\mathrm{e}$ (shaded colours) and of the electric field orientation (arrows) in the (k_x,k_z) space. Maxwell–Jüttner distribution functions are considered with $n_\mathrm{b}/n_\mathrm{p}=0.1$, $\gamma_\mathrm{b}=4$, $T_\mathrm{b}=50\,\mathrm{keV}$, $T_\mathrm{p}=5\,\mathrm{keV}$ and the beam drifting along the z-axis. Reprinted with permission from [33]. © 2010 The American Physical Society.

Three instability classes can be identified according to their wave vector's orientation and electromagnetic properties. This is exemplified in figure 1 which displays the $\boldsymbol{k}$-dependence of the normalized growth rate

$$\delta=\Im\frac{\omega}{\omega_\mathrm{e}}, \quad (41)$$

where $\omega_\mathrm{e}=[n_\mathrm{e}e^2/\epsilon_0m_\mathrm{e}]^{1/2}$ is the nonrelativistic total plasma frequency ($n_\mathrm{e}=n_\mathrm{b}+n_\mathrm{p}$) for a dilute-beam configuration: $n_\mathrm{b}/n_\mathrm{p}=0.1$, $\gamma_\mathrm{b}=4$, $T_\mathrm{b}=50\,\mathrm{keV}$ and $T_\mathrm{p}=5\,\mathrm{keV}$. The plasma drift velocity follows from the current neutrality condition $\beta_\mathrm{p}=-\beta_\mathrm{b}n_\mathrm{b}/n_\mathrm{p}$.

The well-known two-stream modes [22] are located along the beam direction ($k_x=0$), with a peak growth rate $\delta_\mathrm{max}\sim0.04$ at $k_{z,\mathrm{max}}c/\omega_\mathrm{e}\sim1/\beta_\mathrm{b}$. These are purely electrostatic plasma waves propagating at the phase velocity $\Re\omega/k\sim\beta_\mathrm{b}$. Their maximum growth rate is given by the approximate analytical expressions (in the weak $n_\mathrm{b}/n_\mathrm{p}$ limit)

$$\delta_\mathrm{max}^\mathrm{TS}\approx\begin{cases}\dfrac{\sqrt{3}}{2^{4/3}}\dfrac{1}{\gamma_\mathrm{b}}\left(\dfrac{n_\mathrm{b}}{n_\mathrm{p}}\right)^{1/3} & \text{if}\quad \dfrac{T_\mathrm{b}}{m_\mathrm{e}c^2}\leqslant\beta_\mathrm{b}^2\gamma_\mathrm{b}\left(\dfrac{n_\mathrm{b}}{n_\mathrm{p}}\right)^{2/3},\\ \beta_\mathrm{b}^2\dfrac{m_\mathrm{e}c^2}{T_\mathrm{b}}\dfrac{n_\mathrm{b}}{n_\mathrm{p}} & \text{otherwise,}\end{cases} \quad (42)$$

in the hydrodynamic (cold) and kinetic regimes, respectively [197]. The orientation of the associated electric perturbation can be evaluated from the linear relation $E_x(\omega,\boldsymbol{k})/E_z(\omega,\boldsymbol{k})=(k_x^2c^2/\omega_\mathrm{e}^2-\omega^2\epsilon_{zz})/(k_xk_zc^2/\omega_\mathrm{e}^2+\epsilon_{xz})$ [29]. As expected, figure 1 shows that the two-stream modes fulfil $\boldsymbol{k}\times\boldsymbol{E}=0$.

The filamentation instability, which arises in systems composed of counterstreaming species, belongs to the family of anisotropy-driven instabilities typified by the Weibel instability [77, 216]. Hence, the two designations are often

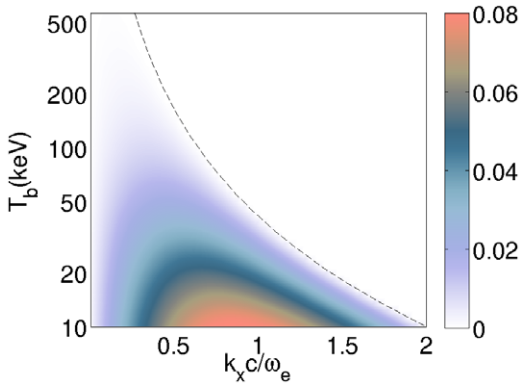

Figure 2. Filamentation growth rate δ as a function of the transverse wave vector k_x and the beam temperature T_b. Maxwell–Jüttner distribution functions are considered with $\gamma_b = 2$, $n_b/n_p = 0.1$ and $T_p = 5$ keV. The cut-off wave vector k_{lim} (equation (44)) is plotted in the dashed line.

used interchangeably in the literature. As the classical Weibel instability, the filamentation modes develop preferentially normal to the 'hot' (beam) direction $k_z \approx 0$. They correspond to aperiodic ($\Re\omega = 0$), mostly magnetic fluctuations amplified by the repulsive force between electron currents of opposite polarity. In figure 1, the filamentation growth rate is seen to maximize at $k_x c/\omega_e \sim 0.5$ with $\delta_{max} \sim 0.02$. An analytical estimate can be derived in the cold limit ($T_b = T_p = 0$), which reads [150].

$$\delta^F_{max} \approx \beta_b \sqrt{\frac{n_b}{\gamma_b n_p}} \tag{43}$$

for $1 \leqslant k_x c/\omega_e < \infty$. In the kinetic (hot) regime associated to figure 1, by contrast, the unstable domain is restricted to $0 \leqslant k_x \leqslant k_{lim}$, with the cut-off wave vector [34]

$$k^2_{lim} = \frac{1}{2}\left[\mathcal{F}_2 - \mathcal{F}_0 + \sqrt{(\mathcal{F}_2 - \mathcal{F}_0)^2 + 4(\mathcal{F}_0\mathcal{F}_2 - \mathcal{F}_1^2)}\right]\frac{\omega_e^2}{c^2}, \tag{44}$$

where $\mathcal{F}_n = \sum_j (n_j/n_e)\mu_j\beta_j^n$. Assuming $n_b/n_p \ll 1$, we have $k_{lim} \sim \beta_b\sqrt{(n_b/n_p)(m_e c^2/T_b)}$. Interestingly, the fastest-growing filamentation wave vector has the same scallings as k_{lim} [33]. The shrinking of the unstable domain for increasing beam temperatures is illustrated in figure 2 for $\gamma_b = 2$, $n_b/n_p = 0.1$ and $T_p = 5$ keV. Along with the decrease in k_{lim}, the peak growth rate is found to drop as $\delta_{max} \propto T_b^{-3/2}$ [33]. Further analysis shows that, similarly to the cold-fluid scaling (43), the instability is also quenched in the high-γ_b limit as $\delta_{max} \propto \gamma_b^{-1/2}$ due to the beam's increasing inertia [33]. Note that any combination of Maxwell–Jüttner functions with non-vanishing β_j's is filamentation unstable (i.e. $k_{lim} > 0$) due to a finite anisotropy. In practice, though, (44) sets an effective stabilization threshold when $k_{lim} \leqslant 1/L_x$, where L_x is the transverse size of the beam–plasma system (typically of the order of the laser spot). This incomplete stabilization contrasts with the total suppression occurring for model distributions allowing for independent longitudinal and transverse thermal spreads [30, 34, 183, 205]. In fact, filamentation proves mostly vulnerable to the transverse temperature $T_{bx} = \langle p_x^2/\gamma\rangle$, causing a pressure force counteracting the magnetic pinching force. In the simplified waterbag case with weak beam density and temperature, stabilization is thus predicted for [183]

$$\frac{\Delta\beta_b^2}{\beta_b^2} \geqslant \frac{n_b}{\gamma_b n_p}, \tag{45}$$

where the beam's transverse velocity spread, $\Delta\beta_b$, is related to the transverse temperature, $T_{b\perp} \equiv T_{bx}$, through [183]

$$T_{bx} = \frac{m_e\gamma_b c^2}{2}\left[1 + \frac{1-\Delta\beta_b^2}{2\Delta\beta_b}\ln\left(\frac{1-\Delta\beta_b}{1+\Delta\beta_b}\right)\right], \tag{46}$$

which simplifies to $T_{bx} \sim m_e\gamma_b c^2\Delta\beta_b^2/3$ in the limit $\Delta\beta_b \ll 1$.

Although the filamentation modes are essentially magnetic, figure 1 demonstrates that their electric-field component is not purely inductive ($\boldsymbol{k}\cdot\boldsymbol{E} \neq 0$). This follows from the fact that, except for perfectly symmetric systems (i.e. with $n_b = n_p$, $\beta_b = -\beta_p$ and $T_b = T_p$), the off-diagonal term ϵ_{xz} in (38) is generally nonzero [31]. The ion response to the resulting space-charge force should therefore be taken into account in the weaky-unstable regime [161, 211].

The spectrum in figure 1 turns out to be governed by off-axis modes, thus propagating obliquely to the beam. The fastest-growing oblique mode with $\delta_{max} = 0.07$ is located at $(k_x, k_z) = (0.8, 0.95)$. As shown in [34], these modes are quasielectrostatic in a broad system-parameter range including the configuration of figure 1. For $n_b/n_p \ll 1$, their maximum growth rate can be estimated to be [34, 171, 197]

$$\delta^0_{max} \approx \frac{\sqrt{3}}{2^{4/3}}\left(\frac{n_b}{\gamma_b n_p}\right)^{1/3}, \tag{47}$$

in the hydrodynamic regime defined by

$$\frac{T_b}{m_e c^2} < \frac{3}{2^{10/3}}\left(\frac{n_b}{n_p}\right)^{2/3}\gamma_b^{1/3}\frac{\left(1+\gamma_b^{-2}\right)^{2/3}}{\left(1+\gamma_b^{-1}\right)^2}. \tag{48}$$

In the opposite kinetic limit, one has approximately

$$\delta^0_{max} \approx \beta_b^2\frac{m_e c^2}{T_b}\frac{n_b}{n_p}. \tag{49}$$

In both regimes, the longitudinal wave vector of the dominant oblique mode is correlated to the dominant two-stream mode ($k_z c/\omega_e \sim 1/\beta_b$), whereas the transverse component $k_x c/\omega_e$ decreases below unity when moving into the kinetic regime [33].

The domain of preponderance of each instability class has been computed in the (n_b/n_p, γ_b, T_b) parameter space for a fixed plasma temperature $T_p = 5$ keV [32, 33]. The surfaces that delimit regions governed by different instability classes are displayed in figure 3 and coloured according to the local maximum (in $\boldsymbol{k}$-space) growth rate. The two-stream instability prevails for non-relativistic beam drift energies ($\gamma_b - 1 \ll 1$), as well as in weakly relativistic systems with hot enough beams. This follows from the quenching of the filamentation and oblique instabilities with decreasing β_b and increasing T_b, respectively. Filamentation modes govern systems where the beam and plasma densities are similar (in the FIS, this mostly concerns the laser-absorption region), whereas oblique modes are dominant for dilute relativistic beams. The

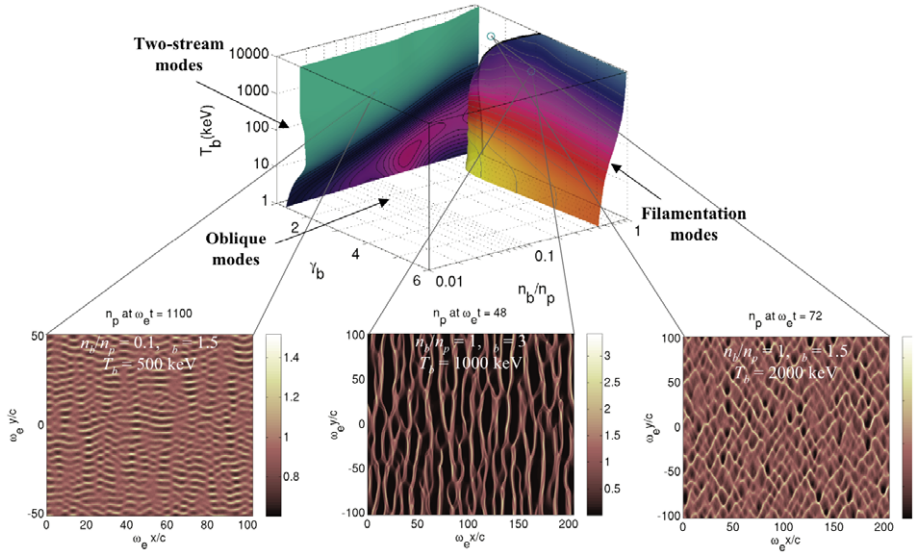

Figure 3. (top) Hierarchy of the two-stream, oblique and filamentation modes in the $(n_b/n_p, \gamma_b, T_b)$ parameter space for Maxwell–Jüttner distribution functions. (bottom) Plasma density profiles at the end of the linear phase as predicted by 2D PIC simulations, each ruled by a specific instability class. The plasma temperature is $T_p = 5$ keV and the beam flows along the y-axis. Reprinted with permission from [34]. © American Institute of Physics.

filamentation-to-oblique transition is mostly determined by γ_b for dense, cold and weakly relativistic beams, and by n_b in the relativistic and ultra-relativistic regimes. Note that oblique modes always dominate for hot enough relativistic beams. These results are illustrated by the lower panels of figure 3 showing the plasma density profiles observed in three 2D PIC simulations, each ruled by a distinct instability class. The spectral characteristics of each modulated pattern have been checked to perfectly agree with linear theory. It is worth noting that the Maxwell–Jüttner fit obtained from the laser–plasma simulations of [45] (i.e. $T_b = 530$ keV and $\gamma_b = 1.4$) corresponds to a dominant two-stream instability in a collisionless background with densities $n_b/n_p < 0.1$.

3.4.3. Collisional effects. Collisions are expected to influence the development of the instabilities in the high-density, low-temperature regions penetrated by the electron beam, that is, at a distance from the laser-absorption region. As a consequence, most of the studies performed in this respect have considered dilute collisionless beams interacting with dense, nonrelativistic collisional plasmas [45, 73, 87, 88, 108]. Collisional effects are frequently described by simplified Krook-like models, which consist in introducing phenomenological relaxation terms in the Vlasov equation [148]. The most accurate approach of this kind is the particle-number-conserving BGK model [18]

$$\frac{\partial f_p}{\partial t} + \boldsymbol{v}.\nabla_x f_p - e\left(\boldsymbol{E} + \boldsymbol{v}\times\boldsymbol{B}\right).\nabla_v f_p = C(f_p) = -\nu\left(\delta f_p - \delta n_p f_p^{(0)}/n_p^{(0)}\right), \quad (50)$$

where $\delta f_p = f_p - f_p^{(0)}$ and $\delta n_p = \int \mathrm{d}^3 v \delta f_p$. The BGK model can be generalized to conserve momentum and energy as well. A more rigorous approach makes use of the Landau collision operators [26, 181]. In the case of a large ion charge ($Z \gg 1$), electron–ion collisions prevail over electron–electron collisions and are described by the operator

$$C_{ei}(f_p) = \frac{Z n_p e^4 \ln\Lambda}{8\pi\epsilon_0^2 m_e^2}\nabla_v.\frac{1}{v}\left(I - \frac{\boldsymbol{vv}}{v^2}\right).\nabla_v f_p(\boldsymbol{v}), \quad (51)$$

where I denotes the identity operator and $\ln\Lambda$ is the Coulomb logarithm. In principle, the BGK collision frequency ν should be adjusted so as to reproduce the plasma susceptibility obtained from the Landau operator in the collisional limit, which yields $\nu = \nu_{ei}$, where ν_{ei} is the usual collision frequency [16].

An exact evaluation of the collisional two-stream instability using a Maxwell–Jüttner-distributed beam and the electron–ion Landau operator has been recently carried out. Figure 4 plots the k_z-dependence of the growth rate for the parameters $n_e = 10^{23}$ cm^{-3}, $n_b/n_p = 0.01$, $T_b = 100$ keV, $\gamma_b = 3$, $T_p = 1$ keV, $Z = 10$ and $\ln\Lambda = 2$. There follows a collision frequency $\nu_{ei}/\omega_e = 0.01$, that is, approximately twice the maximum collisionless growth rate (blue curve). In the presence of collisions, the peak growth rate drops from $\delta_{max} = 5.3\times10^{-3}$ to 1.1×10^{-3}, while the dominant wave number only slightly decreases. Note that the BGK model (red) yields a peak growth rate about 30% lower than the Landau value (black).

If strong enough, collisions are able to completely stabilize the two-stream modes [87, 185]. This is illustrated in figure 5, where the maximum growth rate is plotted as a function of the plasma density, the beam density being fixed at $n_b = 10^{21}$ cm^{-3}. The other parameters are $\gamma_b = 2$, $T_b = 100$ keV, $T_p = 300$ eV, $Z = 10$ and $\ln\Lambda = 2$. The exact collisional curve (black) is fairly approximated by the expression

$$\delta_{max} \approx \delta_{max}^{NC} - \nu_{ei}/2, \quad (52)$$

where δ_{max}^{NC} is the maximum collisionless growth rate (blue curve). The relative error between (52) and the exact values is found to increase as the instability weakens.

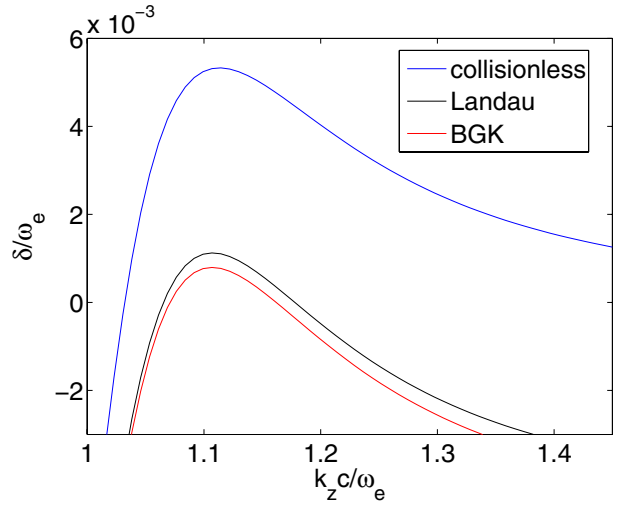

Figure 4. Growth rate $\delta = \Im\omega$ of the two-stream instability with (red, black) and without (blue) e–i collisions for $n_e = 10^{23}\,\mathrm{cm}^{-3}$, $n_b/n_p = 0.01$, $T_b = 100\,\mathrm{keV}$, $\gamma_b = 3$, $T_p = 1\,\mathrm{keV}$, $Z = 10$ and $\ln\Lambda = 2$. The BGK curve (red) is found to understimate the exact Landau curve (black).

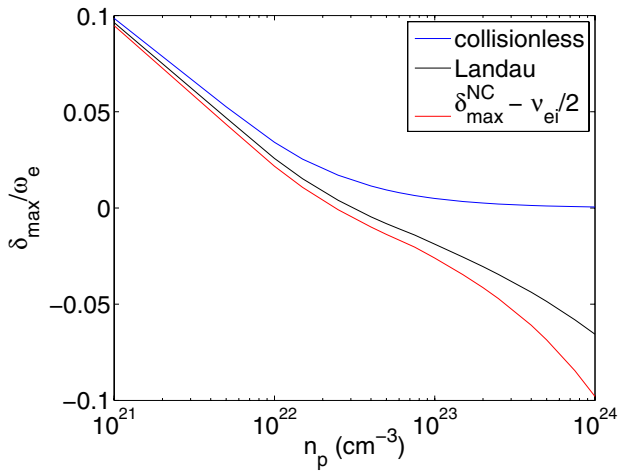

Figure 5. Maximum growth rate of the two-stream instability for $n_b = 10^{21}\,\mathrm{cm}^{-3}$, $T_b = 100\,\mathrm{keV}$, $\gamma_b = 2$, $T_p = 300\,\mathrm{eV}$, $Z = 10$ and $\ln\Lambda = 2$.

Complete stabilization ($\delta_{max} \leqslant 0$) is achieved here for $n_p \geqslant 3.2 \times 10^{22}\,\mathrm{cm}^{-3}$, which corresponds to $\nu_{ei}/\omega_e \geqslant 0.04$. By contrast, (52) yields a somewhat underestimated stabilization threshold ($n_p \geqslant 2.5 \times 10^{22}\,\mathrm{cm}^{-3}$).

Because of the close connection between two-stream modes and oblique modes in a broad parameter range [33], the latter are affected by collisions in a similar fashion, exhibiting, in particular, complete stabilization in the strong collisional limit [87].

As first demonstrated by Molvig [135] and further investigated in [73, 88, 108], a starkly different scenario takes place for the filamentation instability. The main result is that for dilute and energetic enough beams, collisions keep the system unstable regardless of the transverse beam temperature. Moreover, collisions shrink the unstable domain towards small k's. Figure 6, which is extracted from [73], illustrates these effects by comparing the k-variations of the collisionless and collisional filamentation growth rates for

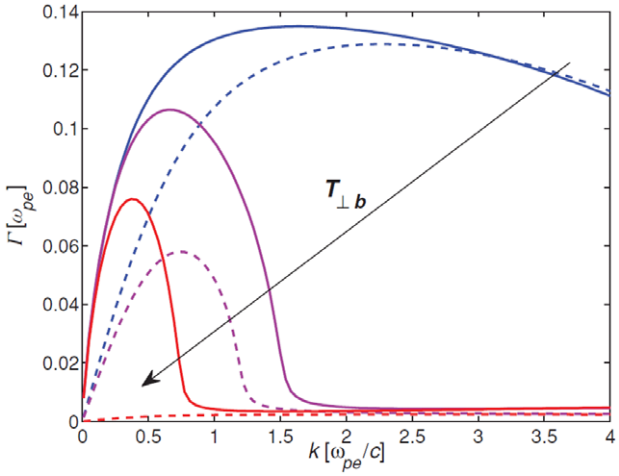

Figure 6. Filamentation growth rate as a function of the wave vector in collisionless (dashed lines) and collisional (solid lines) configurations for $\gamma_b = 5$, $T_p = 10\,\mathrm{keV}$, $n_b/n_p = 0.1$, $\nu/\omega_e = 0.5$ and increasing beam transverse temperatures: $T_{b\perp} = 0.5\,\mathrm{keV}$ (blue), $T_{b\perp} = 9\,\mathrm{keV}$ (magenta) and $T_{b\perp} = 34\,\mathrm{keV}$ (red). Reprinted with permission from [73]. © 2010 Cambridge University Press.

waterbag distribution functions with $\gamma_b = 5$, $T_p = 10\,\mathrm{keV}$, $n_b/n_p = 0.1$. A BGK collision model is employed with $\nu/\omega_e = 0.5$. As expected, the instability is weakened and confined to decreasing wave numbers as the beam transverse temperature is raised. The instability is enhanced in the presence of collisions, especially in the large-temperature limit ($T_{b\perp} = 34\,\mathrm{keV}$) where, according to equation (45), it should be stabilized in the collisionless regime. PIC simulations confirm the predicted robustness of the collisional filamentation and the generation of filamentary structures larger than in the collisionless regime [73, 106]. Note that the highly-collisional filamentation instability corresponds to the so-called resistive filamentation instability seen in hybrid simulations [84, 93, 186, 187], which is derived assuming the return current obeys Ohm's law $\boldsymbol{E} = \eta \boldsymbol{j}_p$, where η is the electrical resistivity [84, 98].

3.4.4. Weibel/filamentation instability in fast electron generation and transport. Multidimensional PIC simulations of the fast electron generation in overcritical plasmas have shown that the filamentation instability plays a major role in the laser-absorption region [2, 59, 146, 157, 161, 176, 177]. This is so because, for a large enough laser spot ($\gg\lambda_0$) and normal incidence, the electron acceleration initially takes place within an essentially 1D geometry. As a result of this plane-wave approximation, the transverse canonical momentum is conserved: $p_\perp(x(t), t) - eA_\perp(x(t), t) = p_{\perp 0}$. As the vector potential $A_\perp$ vanishes over a few plasma skin depths, the fast electrons quickly recover their initial (thermal) transverse momentum $|p_{\perp 0}|$ ($\ll |p_x|$) when penetrating into the target. There follows an input electron distribution strongly elongated along the longitudinal direction, hence prone to the Weibel/filamentation instability. Magnetic fluctuations are then spontaneously generated along the target surface, leading to fragmentation of the fast electron profile into small-scale filaments.

This process is illustrated in figure 7 in the case of a 3D PIC simulation of a $10^{20}\,\mathrm{W\,cm}^{-2}$ laser plane wave impinging

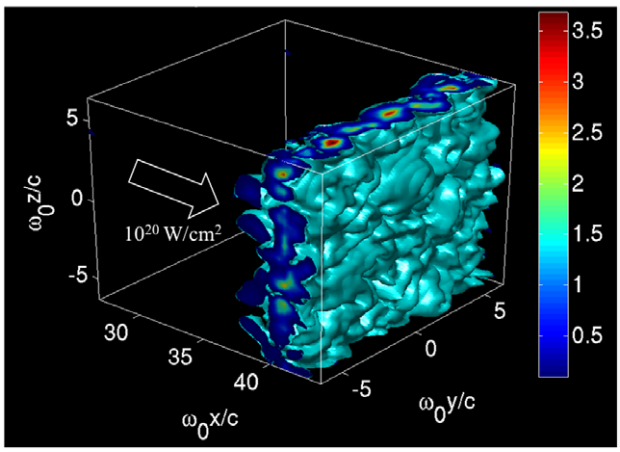

Figure 7. Isosurface of the magnetic field $|\boldsymbol{B}|$ associated to Weibel-generated fluctuations (averaged over a laser cycle) in a 3D PIC simulation of a 10^{20} W cm^{-2} laser plane wave interacting with a $50n_c$ plasma. The arrow points along the incoming laser direction and the magnetic field is normalized to $m_e\omega_0/e$.

onto a $50n_c$ plasma. At $t = 100\omega_0^{-1}$ (where ω_0 is the laser frequency), magnetic fluctuations have grown in the interaction region to an amplitude $|\boldsymbol{B}| \sim m_e\omega_0/e$ with a transverse size $\lambda \sim c/\omega_0$. The underlying physics can be understood as follows. Let us assume for simplicity that the plane-wave approximation initially holds and that the hot electron distribution is cold in the transverse direction, $f_b(\boldsymbol{p}) \propto \exp[-\mu\sqrt{1+p_x^2/(m_ec)^2}]\delta(p_y)$. In the high-energy limit ($\mu < 1$), μ is related to the mean Lorentz factor as $\langle\gamma\rangle = K_2(\mu)/K_1(\mu) \sim 2/\mu$. Substitution of the above distribution into equations (38) and (39) (noting that the 'hot' axis is now the x-axis) readily yields the maximum Weibel growth rate $\delta_{\max} = \omega_{pb}\sqrt{K_0(\mu)/K_1(\mu)} \sim \omega_{pb}\sqrt{-\mu\ln\mu}$, where ω_{pb} is the hot electron plasma frequency. Because of the vanishing dispersion in the transverse momentum, the growth rate saturates to $\delta_{\max}$ for wave vectors $k_y \geqslant \sqrt{\mu}$. Assuming that the hot electron density is equal to the critical density ($\omega_{pb} = \omega_0$) and that the normalized mean electron energy scales as $\langle\gamma\rangle \sim a_0^\alpha$, where $\alpha \sim 2/3 - 1$ [11, 155, 219], one gets $\delta_{\max} \sim \omega_0\sqrt{\ln a_0/a_0^\alpha}$. As a result, the growth rate is comparable to the laser frequency for $a_0 > 1$.

The saturated level of the magnetic fluctuations, B_{sat}, can be estimated from the widely used trapping criterion [1, 49, 146, 183, 223] which expresses the fact that the exponential growth phase comes to an end when the electron bouncing frequency inside a magnetized filament of period $2\pi/k_y$, $\omega_B \sim \omega_0\sqrt{\langle 1/\gamma\rangle(k_yc/\omega_0)(eB_{sat}/m_e\omega_0)}$, becomes of the order of the growth rate $\delta(k_y)$. Using the above estimates with $\langle 1/\gamma\rangle = K_0(\mu)/K_1(\mu)$ and $k_y = \mu^{1/2}$, one finds the saturated magnetic amplitude $eB_{sat}/m_e\omega_0 \sim \mu^{-1/2} = a_0^{\alpha/2}$. The maximum quiver momentum being $p_y = m_e\langle\gamma\rangle\omega_B/k_y$, the approximate divergence is $p_y/p_x \sim \omega_B/k_yc \sim \sqrt{\ln a_0}$. Magnetic deflections within the self-generated magnetized filaments then rapidly cause the hot electrons to acquire a divergence of the order unity. The Weibel/filamentation instability therefore appears as the mechanism mainly responsible for the large angular spread seen in simulations [2, 59] and experiments [82].

The assumption of a zero transverse temperature for the hot electrons actually holds only a few skin depths away from the laser-absorption region. In reality, however, the instability develops within the skin layer, where the electron distribution has a finite anisotropy, thus yielding a weaker growth rate. This process has been addressed in [146] by fitting the simulated hot electron distribution to a semi-relativistic, two-temperature Maxwellian [145]. Defining $A = T_x/T_\perp - 1 > 0$ and applying the same reasoning as above, the saturated magnetic field is expected to scale as

$$B_{sat} \approx 0.16a_0^{2\alpha}\sqrt{\frac{n_b}{n_c}}\frac{A^{5/2}}{(A+1)^3}\frac{m_e\omega_0}{e} \leqslant 0.04a_0^{2\alpha}\sqrt{\frac{n_b}{n_c}}\frac{m_e\omega_0}{e}. \quad (53)$$

3D PIC simulations performed with a laser amplitude $a_0 = 3$ and plasma densities $n_e = (1-2)n_c$ predict a maximum anisotropy $A \sim 2$–10 and a saturated magnetic amplitude in reasonable agreement with the above estimate.

The 2D PIC results displayed in figures 8(*a*)–(*d*) further depict this self-generated magnetic scattering effect in the case of a 10^{19} W cm^{-2} ($a_0 = 3$) laser pulse injected into a $100n_c$ cone-guided target [10]. The pulse has a $500\omega_0^{-1}$ duration and a $16\lambda_0$ width. A 1 μm scale-length exponential pre-plasma is added on the inner target walls (panel (*a*)). A set of typical electron trajectories inside the absorption region are plotted in panel (*b*). Beside being reflected by the laser field in the low-density region ($x \sim 200c/\omega_0$), the fast electrons undergo strong deflections across the skin layer ($x \sim 220c/\omega_0$) due to magnetic modulations of amplitude $B_z \sim 1.5m_e\omega_0/e$. The resulting electron momentum distribution is shown at $t = 300\omega_0^{-1}$ before the laser maximum (panel (*c*)) and at the time of the laser maximum (panel (*d*)). The root-mean-square angle of the fast (>1 MeV) electrons is found to increase during this time interval from $\langle\theta^2\rangle^{1/2} \sim 34^\circ$ to $\langle\theta^2\rangle^{1/2} \sim 48^\circ$.

In the plane-wave case, the rapid magnetic build-up breaks the invariance along the transverse directions, and hence the transverse canonical momentum is no longer conserved. The electron acceleration is modified due to the coupling between the laser field and the quasistatic magnetic fluctuations. This multidimentional effect causes the transverse velocity of the electrons injected into the target to oscillate at the laser frequency. More precisely, it has been found in [2] using a quasilinear analysis that the averaged transverse electron velocity behaves as

$$\langle v_y(x,t)\rangle \approx \gamma^{-2}\sum_k \int_0^x dx' \int_0^{x'} dx'' \int_0^{x''} dx''' kc_k(x',x''') \times \sin\left(k\gamma^{-1}\int_{x'''}^{x'} d\xi\, A_y(\xi,t)\right), \quad (54)$$

where $A_y(t,x)$ is the laser vector potential, $c_k(x_1,x_2) = \langle B_k(x_1)B_{-k}(x_2)\rangle$ is the spectral density of the perturbative Weibel-generated field $B(x,y) = \sum_k B_k(x)e^{iky}$. The above equation shows that $\langle v_y\rangle$ changes sign with the laser field in accordance with PIC simulations [2].

The late-time dynamics of the magnetized filaments has been frequently investigated by means of simulations resolving only the plane orthogonal to the beam's axis [63, 92, 122, 131, 172]. In the case where $n_b \ll n_p$, the beam electrons are strongly pinched by the magnetic field, which expels the plasma electrons from the filament's interior. Further

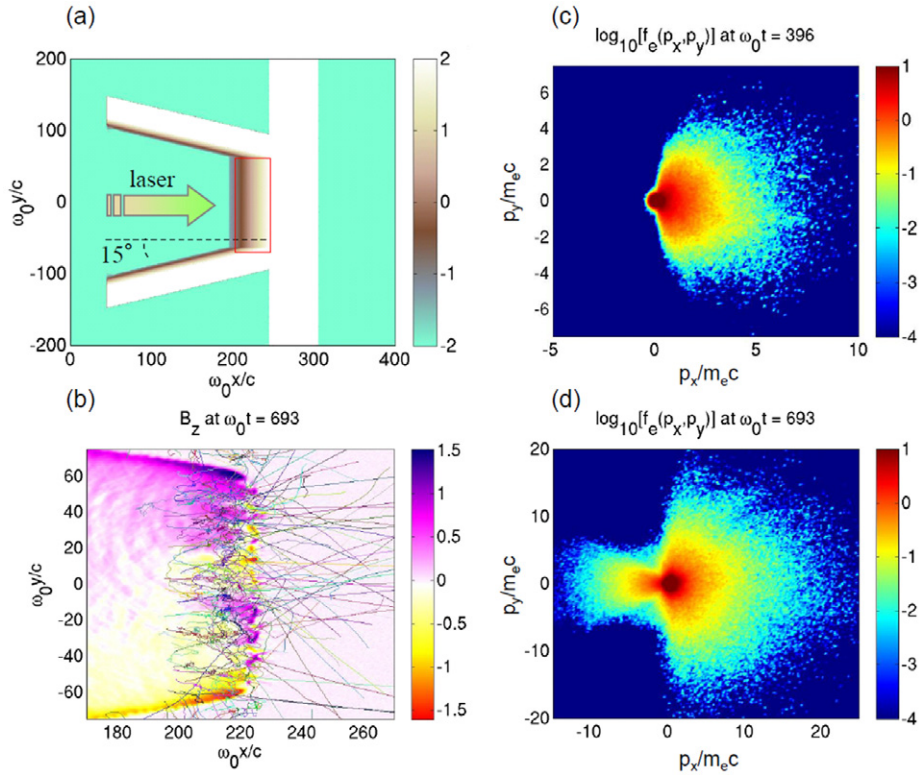

Figure 8. 2D PIC simulation of the interaction of a 10^{19} W cm^{-2} laser pulse with a cone-attached target: initial density profile, log scale (*a*); typical electron trajectories within the box shown in (*a*) and map of the quasistatic magnetic field B_z (normalized to $m_e/\omega_0 e$) at the time of the on-target laser peak (*b*); $p_x - p_y$ electron phase space around the absorption region at $t = 300\omega_0^{-1}$ before (*c*) and at the time (*d*) of the laser peak. See text and [10] for further details.

magnetic pinching of the beam electrons generates a strong space-charge field accelerating the ions in the radial direction [92, 172]. The nonlinear stage is dominated by the merging of magnetically-interacting neighbouring filaments (due to incomplete current shielding by the plasma electrons), leading to increasingly large filaments. While this merging process is accompanied by a steadily-declining total beam current, Polomarov *et al* [156] have demonstrated that during its earliest phase, the fusion of sub-Alfvénic filaments (i.e. carrying current $I < I_A = \gamma_b\beta_b 4\pi m_e c/\mu_0 e \approx 17.05\gamma_b\beta_b$ kA) entails an increase in the magnetic energy and, consequently, a decreasing kinetic energy, whereas the coalescence of super-Alfvénic filaments ($I > I_A$) occurring at later times gives rise to a slowly-decaying magnetic energy. In the case of comparable beam and plasma densities, simulations indicate that the typical filament size increases roughly linearly with time as a result of successive coalescences [63, 131].

Provisos, however, must be made concerning the practical relevance for the FIS of the aforementioned simulations. First, all of them consider beam electrons with weak thermal spreads in contradistinction with the momentum distributions of laser-accelerated electrons seen in PIC simulations (figures 8(*c*) and (*d*)). Second, by describing the electron dynamics in the plane perpendicular to the beam's flow only, they do not capture the parallel or oblique unstable modes described in section 3.4.2. As shown in [184] through comparisons with 3D simulations, the overall influence of these multidimensional processes on the beam transport is best reproduced by 2D calculations performed in the plane of the beam's flow. Finally, the simulations carried out in [63, 92, 113, 122, 131, 156, 172, 182] employ initially uniform beam profiles with periodic boundary conditions, thus neglecting the stabilization provided by the dilution of the diverging beam as it propagates away from the injection region. It is then no surprise that a somewhat different picture emerges from more realistic simulations of the fast electron generation and transport. In particular, for laser intensities 10^{20-21} W cm^{-2} (figure 9), filamentation is found to be confined to the vicinity of the laser-irradiated zone [2, 59, 161, 210]. While this region remains (weakly) Weibel-unstable in the nonlinear stage due to the destabilizing effect of the ion motion, the interior region becomes stable owing to the important dilution of the fast electrons [161]. Importantly, the filamentation-driven rippling of the target surface triggers additional laser heating mechanisms such as the Brunel effect [10, 161]. Furthermore, the surface ions may be accelerated by the laser radiative pressure to velocities high enough to trigger the ion-Weibel instability. The magnetic turbulence thus generated may give rise to a collisionless shock of astrophysical interest [74].

In [176], the magnetized beam filaments have been shown to act as random scattering sources for the return current electrons, yielding an effective electrical resistivity of the order of $\nu_A = \omega_c/\omega_p^2\epsilon_0$, where ω_c is the electron cyclotron frequency in the average magnetic field amplitude $\langle|B|\rangle$. Yet, large-scale laser–plasma simulations indicate that this 'anomalous' effect only arises within a few micrometres of the irradiated surface, where the background temperature is high enough to quench collisional processes [42].

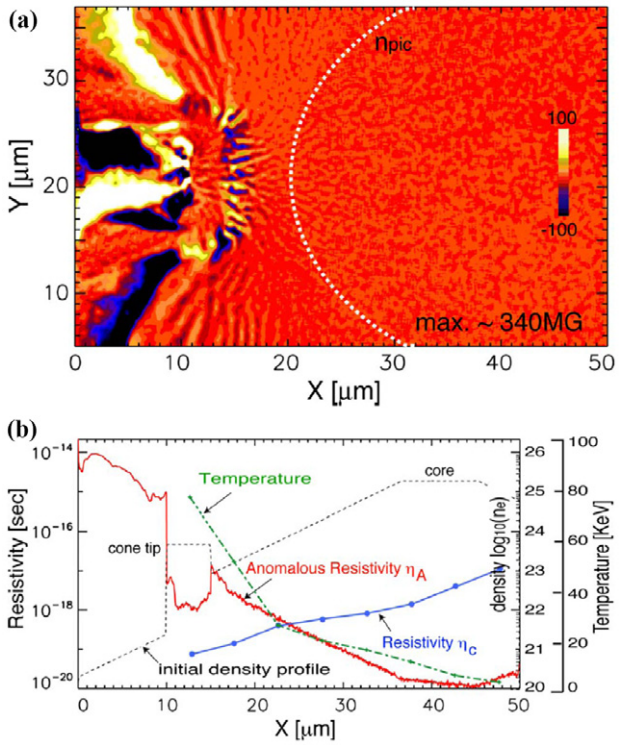

Figure 9. Collisional 2D PIC simulation of the interaction of a 10^{20} W cm^{-2} laser pulse with a cone-guided compressed target: (*a*) quasistatic magnetic field (in MG) at 860 fs; (*b*) x-profiles of the anomalous resistivity, collisional resistivity, density and bulk electron temperature at $y = 21\,\mu$m. Reprinted with permission from [42]. © 2008 American Institute of Physics.

3.4.5. Electrostatic instabilities in FET. Few studies have addressed the influence of the electrostatic (two-stream or oblique) instabilities in the FIS context. One notable exception is the simulation work of Kemp *et al* [112] who showed that, in a 1D geometry and for a laser intensity of 10^{19} W cm^{-2}, two-stream kinetic modes govern the energy transfer from hot to thermal electrons in plasma densities $<10^{23}$ cm^{-3}, whereas they prove strongly inhibited by Coulomb collisions at higher densities.

It is well known that the nonlinear evolution of the two-stream instability depends on the monochromatic or broadband character of the unstable spectrum [197]. The latter case corresponds to the weakly-unstable, kinetic limit and, to first order, is amenable to quasilinear theory [50]. Through resonant wave-particle interaction (i.e. involving waves satisfying $\omega = \boldsymbol{k}\cdot\boldsymbol{v}$), the beam distribution tends to flatten down to the plasma thermal velocity. This weak-turbulence problem has been tackled in [70, 171, 197] where the plateau formation was found to be disturbed by secondary, nonlinear ion-induced scattering and parametric processes. If not collisionally suppressed, this kinetic regime seems to prevail in the FIS context due to the broadly-spread and monotonically-decreasing momentum distribution of the hot electron source.

These mechanisms are illustrated here by 1D PIC simulations of the interaction of a 3×10^{19} W cm^{-2} laser pulse with a $100n_c$ plasma. The mesh size and time step are $\Delta x = 8\times10^{-4}\lambda_0$ and $\Delta t = 2.2\times10^{-3}$ fs, respectively.

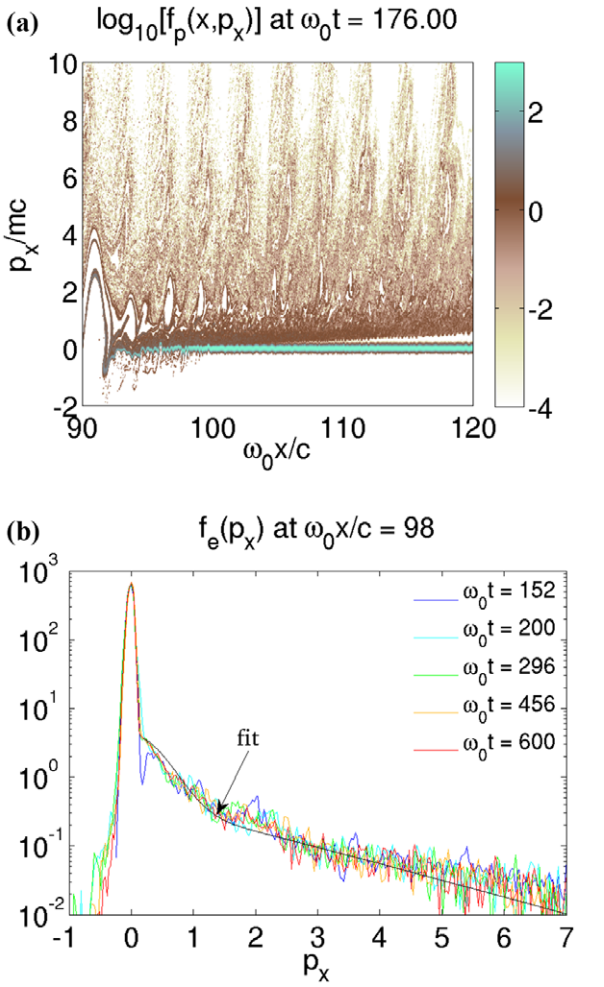

Figure 10. 1D PIC simulation of the interaction of a 3×10^{19} W cm^{-2} laser wave with a $100n_c$, 1 keV plasma: (*a*) $x-p_x$ electron phase space of the interaction region at $t = 176\omega_0^{-1}$; (*b*) momentum distribution at various times at $x = 98c/\omega_0$ and averaged over half a laser wavelength. The solid line plots the high-momentum fit equation (55).

The initial electron temperature is 1 keV and a $1\lambda_0$ scale-length exponential pre-plasma is added on the target surface. The laser profile is constant after a 5-cycle linear ramp. In order to obtain a quasistationary kinetic energy flux into the plasma and, therefore, help identify the unstable beam–plasma processes, the ions are kept fixed in a first stage. As a result, the instantaneous laser-to-plasma absorption rate has an approximately constant value of ~12%. Beyond the laser-irradiated surface ($x \sim 90c/\omega_0$), the $x-p_x$ electron phase space displayed in figure 10(*a*) exhibits $2\omega_0$ high-energy jets ($p_x/m_ec \geqslant 4$) typical of the $J\times B$ acceleration mechanism [116]. The electron vortices centred on $p_x/m_ec \sim 1$ point to the beam-driven excitation of a strongly nonlinear wave close to the absorption region ($x < 100c/\omega_0$). This wave, however, rapidly damps out due to bulk electron trapping, hence yielding a monotonically-decreasing average momentum distribution, as plotted, at various times, in figure 10(*b*). The high-momentum part ($p_x > 0.2m_ec$) of this distribution carries a density $n_b/n_c \sim 0.2$ and, to a good approximation, can be fitted to

$$f_b(p_x) \approx 1.67\times10^3 e^{-5.6\gamma_x} + 0.68e^{-0.57\gamma_x}, \qquad (55)$$

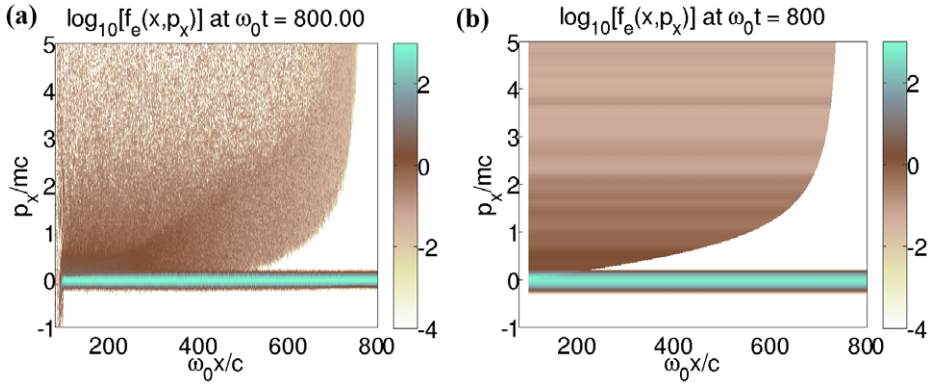

Figure 11. Electron $x - p_x$ phase space at $t = 800\omega_0^{-1}$ as predicted by a self-consistent PIC simulation (a) and the ballistic propagation of the hot electron source (b). Same parameters as in figure 10.

where $\gamma_x = \sqrt{1 + p_x^2/(m_e c)^2}$. Because of its decreasing shape, the source distribution is locally stable with respect to electrostatic fluctuations, as also observed by Tonge *et al* [210]. Deeper into the target ($x > 105c/\omega_0$), though, time-of-flight differences generate a transient positive gradient destabilizing the hot electron distribution.

The quasilinear relaxation induced by the two-stream modes developing in the $\partial f_b/\partial p_x > 0$ region is evidenced in figure 11, where the PIC-simulated electron phase space at $t = 800\omega_0^{-1}$ is compared to that obtained by ballistically evolving the source distribution (55). A plateau clearly forms in the gap region separating the hot and thermal electrons, with a width increasing with the distance from the injection surface. This proves that the advection time $\tau_{adv} = x(v_{min}^{-1} - c^{-1})$ (where v_{min} is the minimum velocity of the hot electrons) is much larger than the characteristic growth time $\tau_{TS} \sim (n_e/n_b)(\Delta p_x^2/p_x^3)\omega_p^{-1}$. This is indeed expected in the present case where $n_b/n_e \sim 10^{-3}$, $p_x/m_e c \sim 2$–4, $\Delta p_x/m_e c \sim 1$, $v_{min} \sim 0.2c$, $x \sim 1000c/\omega_p$, and hence $\tau_{adv} \sim 1000\omega_p^{-1} \gg \tau_{TS} \sim 100\omega_p^{-1}$. Note that the plateau formation is sped up at higher laser intensities due to increased beam density. The quasilinear equations describing the space–time evolution of the averaged beam distribution function and the spectral density of the beam-resonant waves can be analytically solved along the lines of [228], by assuming instantaneous plateau formation and using equation (55) for the source distribution. In agreement with the simulation results, this model predicts that, for a 10^{19} W cm^{-2} laser intensity, a maximum of ~6% of the beam energy is converted to resonant waves. Owing to the stable distribution source, these waves are subsequently reabsorbed by slower electrons arriving at later times. Overall, the wave energy is too weak to affect the beam energy flux. This is demonstrated in figure 12(a), where the spatial profile of the energy flux carried by forward-going ($p_x > 0$) electrons is plotted at various times. Energy is seen to propagate at a velocity $\sim c$ with negligible dissipation over $\sim 800c/\omega_0$. The spatial variations near the right-hand edges of the profiles stem from time-of-flight differences. Figure 12(b) corresponds to a 10^{20} W cm^{-2} laser intensity: albeit more strongly modulated than in panel (a), the energy flux profiles do not reveal significant dissipation either. These findings contrast with the fast relaxation found in the 2D simulation study of Tonge *et al* [210], which was attributed to enhanced

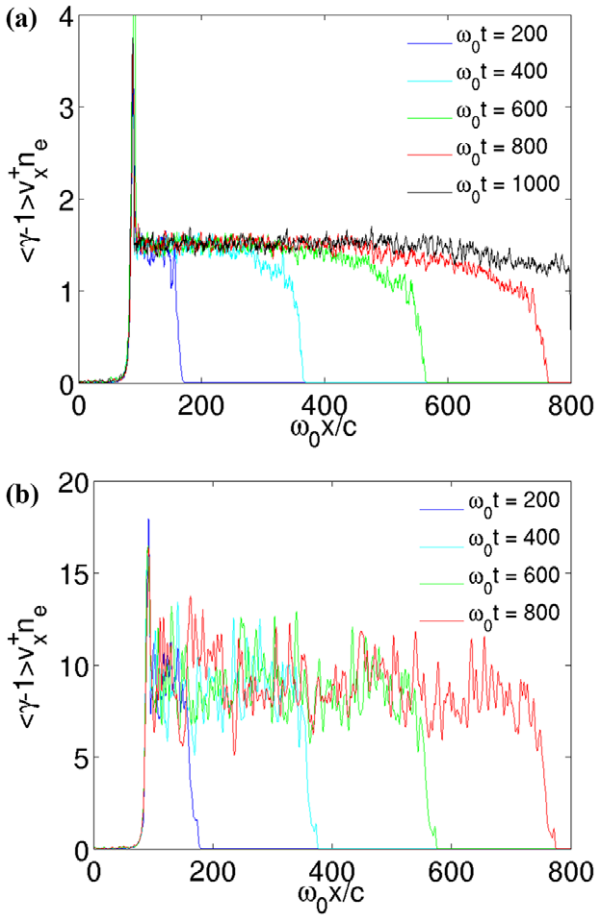

Figure 12. Energy flux density of the forward-going electrons (in units of $m_e c^3 n_c$) as a function of x for a laser intensity of 3×10^{19} W cm^{-2} (a) and 10^{20} W cm^{-2} (b).

electrostatic fluctuations. The origin of this discrepancy is not as yet clearly understood: it may stem from 2D physical effects or from the artificial collisionality caused by insufficient numerical resolution.

The time evolution of the wave spectrum in the space region $375 < \omega_0 x/c < 400$ is displayed in figure 13(a). As slower and slower electrons reach the detection region, waves of decreasing phase velocity are emitted, hence the observed spectral broadening towards high k's. The case of

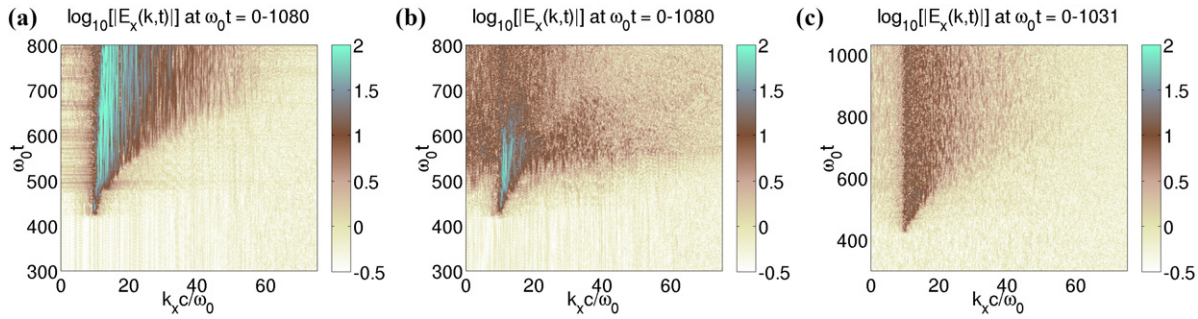

Figure 13. Electric field spectrum $|E_x(k,t)|$ in the space region $375 < \omega_0 x/c < 400$. Panels (a) and (b) correspond to collisionless cases with immobile (a) and mobile (b) ions, while e–i and e–e Coulomb collisions are described in panel (c). The ion charge and temperature are $Z = 13$ and $T_i = 0.2\,\mathrm{keV}$, respectively (other parameters identical to those of figure 10).

mobile aluminum ions with charge $Z = 13$ and temperature $T_i = 0.2\,\mathrm{keV}$ is treated in figure 13(b). The ions close to the interaction region ($\omega_0 x/c < 110$) are kept fixed to maintain an unchanged kinetic energy flux. Weaker and shorter-lived electric fluctuations are then generated, as a result of a modulational instability which efficiently scatters the beam-excited waves outside the beam-resonant region [76, 134, 206]. This parametric process can be modelled assuming the primary waves behave as an monochromatic pump wave (ω_1, k_1) decaying into an ion wave (ω, k) and Langmuir waves $(\omega_1 \pm \omega, k_1 \pm k)$. The corresponding dispersion relation is [134]

$$1 + \frac{\omega_p^2 (k\lambda_D)^2}{4} \frac{W_E}{n_e T_e} \frac{(1+\chi_i)\chi_e}{1+\chi_e+\chi_i} \left(\frac{1}{D_-} + \frac{1}{D_+} \right) = 0, \qquad (56)$$

where $D_\pm = (\omega \pm \omega_1)^2 - \omega_p^2 - 3v_e^2(k \pm k_1)^2$, λ_D is the Debye length, χ_j is the jth component susceptibility and W_E is the wave energy density. In the present case, one has $\omega_1/\omega_p = 0.98$, $k_1\lambda_D = 0.53$ and $W_E/n_e T_e \sim 0.13$. Numerical resolution of (56) then yields a peak modulational growth rate $\delta_{max} = 2.5 \times 10^{-3}\omega_p$ for the wave number $k_{max} = 0.13\lambda_D^{-1}$ and the real frequency $\omega_{max} = 2 \times 10^{-4}\omega_p$. We have checked that these values closely reproduce the simulation results. The high-k secondary waves generated by this instability are strongly Landau-damped by the bulk plasma electrons, which, as observed in [112], gives rise to suprathermal tails but negligible ion heating (not shown). When e–i and e–e Coulomb collisions are switched on [152], figure 13(c) shows that the beam–plasma instability is strongly weakened. This is expected since, for the parameters under consideration ($n_e = 100 n_c$, $T_e = 1\,\mathrm{keV}$ and $T_i = 0.2\,\mathrm{keV}$), the collision frequency ($\nu_{ei} \sim 0.03\omega_p$) is comparable to the collisionless two-stream growth rate. The primary waves are then too weak to trigger the modulational instability and the beam-to-plasma energy transfer essentially proceeds through the resistive electric field.

In summary, 1D kinetic simulations indicate that electrostatic instabilities play only a minor role in the energy relaxation of fast electrons generated by $10^{19-20}\,\mathrm{W\,cm^{-2}}$ laser pulses into $100 n_c$ plasmas due to the decreasing shape of the electron source distribution. Generalization of these results to more realistic 2D geometries, as attempted in [175, 210], requires further investigation. In particular, the influence of the oblique modes remains to be clearly demonstrated in a FIS-relevant laser–plasma setup.

3.5. Background plasma physics

This section discusses the physics of the background medium (i.e. excluding fast electrons), that is relevant to FET and FI. This broadly falls in the realm of radiation-hydrodynamics, which we will not review in detail. Instead, we focus on aspects of special interest to fast electron transport, which are frequently not emphasized in traditional rad-hydro models. These in particular are fluid models that include fast electrons, incorporate electromagnetic fields, and account for Fermi–Dirac (F–D) statistics (namely background electron degeneracy) in transport coefficients like electrical resistivity. We illustrate the physics relevant to transport by describing in detail the Lee-More resistivity model and comparing it with more complete calculations. We conclude by considering the possible importance of strongly-coupled plasma effects.

It is extremely productive to separate transport problems into a background medium and fast electrons. This requires distinguishing between fast and background electrons, which is generally done based on an intermediate electron energy well below that of most fast electrons yet well above that of most background electrons. One way to do this is to express the total electron population as a sum of a drifting thermal population (for speeds up to several times the thermal speed), which obeys a fluid or other reduced description, plus a fast population. This becomes invalid if the background temperature is comparable to typical fast electron energies, either because the background is strongly heated or the fast electrons have slowed down significantly. We shall assume that the distinction can be validly made. This should be tested by comparison with models that do not split the electron population, and is an ongoing research topic.

Fast electrons and the background interact via collisions and macroscopic electromagnetic fields. Fast electron collisions are discussed in detail in section 3.3 of this paper. The e/m fields evolve according to the Maxwell equations, which contain the charge and current densities, ρ and $\boldsymbol{J}$, carried by the fast electrons and background. Since the fast electrons are not atomically bound, it is trivial to find their ρ and $\boldsymbol{J}$. The background can be much more complicated, depending on whether it is neutral matter, a conductor, or a partially or fully-ionized plasma. We assume the background can be described by a fluid model, meaning it is not a collisionless plasma requiring a fully kinetic description. A fluid model applies to neutral matter (with appropriate and perhaps difficult models for material properties like equation of state (EOS)),

and for plasmas that are sufficiently collisional that the background distribution functions are close to equilibrium (e.g. Maxwellian or F–D).

We focus on the background electron momentum and energy equations, which we write in a form following 'notation II' of [67]:

$$m_e \frac{\partial \boldsymbol{v}_e}{\partial t} = -e\left(\boldsymbol{E} - \boldsymbol{E}_C - \boldsymbol{E}_{NC}\right), \tag{57}$$

$$\boldsymbol{E}_C = \underline{\underline{\eta}} \cdot \boldsymbol{J}_e - e^{-1}\underline{\underline{\beta}} \cdot \nabla T_e, \tag{58}$$

$$\boldsymbol{E}_{NC} = -\frac{\nabla p_e}{e n_e} - \boldsymbol{v}_e \times \boldsymbol{B}, \tag{59}$$

$$\left[\frac{\partial}{\partial t} + \boldsymbol{v}_e \cdot \nabla\right](\rho c_V T_e) + p_e \nabla \cdot \boldsymbol{v}_e = \nabla \cdot \left[\underline{\underline{\kappa}} \cdot \nabla T_e + e^{-1} T_e \underline{\underline{\beta}} \cdot \boldsymbol{J}_e\right] + \nu_{ei,T} n_e (T_i - T_e) + \boldsymbol{J}_e \cdot \boldsymbol{E}_C. \tag{60}$$

The Maxwell equations including fast electrons are

$$\frac{\partial \boldsymbol{B}}{\partial t} = -\nabla \times \boldsymbol{E}, \tag{61}$$

$$\epsilon_0 \mu_0 \frac{\partial \boldsymbol{E}}{\partial t} = \nabla \times \boldsymbol{B} - \mu_0(\boldsymbol{J}_e + \boldsymbol{J}_i + \boldsymbol{J}_f), \tag{62}$$

$$\nabla \cdot \boldsymbol{E} = e\epsilon_0^{-1}\left(-n_e - n_f + \sum_i Z_i n_i\right). \tag{63}$$

This section uses SI units and expresses temperature in energy units. Subscripts e,f refer to (background, fast) electron quantities. The electron momentum and energy equations are written in the rest frame of the ions, so that for instance v_e in ηJ_e should be replaced by $v_e - v_i$ in a frame where the ions move. c_V is the specific electron heat capacity, which differs from the Maxwellian ideal-gas result due to e.g. F–D statistics. Fluid equations of this type go back at least to Braginskii [25], and require departures from collisional equilibrium to be small. This breaks down, for example, when $\boldsymbol{E}$ is large enough that a significant portion of the background electrons become runaways, or when v_e exceeds the ion acoustic speed and triggers the ion acoustic drift instability.

We have expressed the forces as equivalent electric fields ($\boldsymbol{E}_C$, $\boldsymbol{E}_{NC}$), which arise from (collisional, collisionless) effects, respectively. The specific $\boldsymbol{E}_C$ and $\boldsymbol{E}_{NC}$ given above are those currently implemented in the Zuma code [120, 196], and neglect certain effects. Namely, $\boldsymbol{E}_{NC}$ lacks the advective term $\boldsymbol{v}_e \cdot \nabla \boldsymbol{v}_e$ and off-diagonal components of the pressure tensor, and $\boldsymbol{E}_C$ neglects collisions of fast with background electrons. $\underline{\underline{\eta}}$ (resistivity), $\underline{\underline{\beta}}$ (thermal force), and $\underline{\underline{\kappa}}$ (thermal conductivity) arise from collisional or other dissipative effects, which in a weakly-coupled plasma are mainly electron–ion (e–i) collisions. They are tensors due to magnetic fields or anisotropic distributions, and reduce to scalars for $\boldsymbol{B} = 0$ and isotropic distributions.

Transport problems frequently consider situations where background electron inertia can be neglected. In plasmas this typically applies for time scales much longer than the period of Langmuir waves. Dropping $\partial \boldsymbol{v}_e/\partial t$ from the momentum equation gives an algebraic equation for $\boldsymbol{E}$ in terms of other quantities: $\boldsymbol{E} = \boldsymbol{E}_C + \boldsymbol{E}_{NC}$. We call this an Ohm's law. Since this approximation gives $\boldsymbol{E}$, we cannot treat Ampère's law (62) as a time evolution equation for $\boldsymbol{E}$. Generally the displacement current $\partial \boldsymbol{E}/\partial t$ is dropped from (62), although it may be fruitful to include it. Ampère's law instead gives $\boldsymbol{J}_e$ and thus $\boldsymbol{v}_e$, which is no longer specified by the inertialess momentum equation. We call dropping both background electron inertia and displacement current the ohmic approximation. Langmuir and light waves are excluded by construction. In addition, quasineutrality is commonly assumed, which entails dropping $\nabla \cdot \boldsymbol{E}$ from Gauss's law and is valid on length scales much longer than the Debye length. One should remember that these approximations are independent, even though they are often generically called 'hybrid models'.

The ohmic and quasineutral approximations currently made in Zuma are

$$\boldsymbol{E} = \boldsymbol{E}_C + \boldsymbol{E}_{NC}, \tag{64}$$

$$\boldsymbol{J}_e = -\boldsymbol{J}_f + \mu_0^{-1} \nabla \times \boldsymbol{B}, \tag{65}$$

$$n_e = \sum_i Z_i n_i. \tag{66}$$

Zuma itself does not handle ion motion, but has been coupled to the rad-hydro code Hydra [126] as detailed in [196].

Regardless of whether an ohmic approximation is made, a key ingredient is specifying the transport coefficients and ionization state. These are aspects where ideal (fully-ionized, weakly-coupled, non-degenerate) plasma physics is insufficient in transport problems. At high density, it is important that the free electrons obey F–D statistics, so that their equilibrium distribution is not the classical Maxwellian. The exclusion principle causes the electrons to have random momentum with respect to the ions even at zero temperature. This becomes significant when $T_e <$ the Fermi energy $E_F \equiv (\hbar^2/2m_e)(3\pi^2 n_e)^{2/3}$. For a sense of scale, fully-ionized solid beryllium ($\rho = 1.84\,\mathrm{g\,cm^{-3}}$) has $E_F = 22.7\,\mathrm{eV}$. Below we sometimes combine T_e with E_F in a qualitatively correct way, although exact expressions involve F–D integrals.

A general-purpose framework for transport coefficients in dense plasmas is Lee and More's model [123], which connects the plasma and non-plasma (solid, liquid, neutral gas) states. Desjarlais [61] provides improvements to their model, as well as to the Thomas–Fermi ionization model based on the Saha equation and particularly relevant near the metal–insulator transition. Zuma currently employs an extended Desjarlais model for ionization and transport coefficients. Whether a material at room temperature is a conductor or insulator can be important for experiments, and difficult for models geared towards plasmas to capture correctly.

The main result of the Lee–More model is the electron relaxation time τ. From this follows the various transport coefficients, including off-diagonal components due to magnetic fields. We present the Lee–More model as embodied in Zuma. It has been extended to include electron–electron (e–e) collisions along the lines of [25, 67]. We cast our results in terms of the resistivity η, which has direct physical meaning via the electron momentum slowing-down rate ν_m. For no magnetic field (or the component of $\underline{\underline{\eta}}$ along $\boldsymbol{B}$), $\eta = (m_e/n_e e^2)\nu_m$. τ and ν_m are related by $1/\nu_m = \tau A^\alpha$.

A^α accounts for electron F–D statistics and involves F–D integrals F_n:

$$A^\alpha = \frac{4}{3}\frac{F_2(\hat{\mu})}{\left[1+\exp(-\hat{\mu})\right]F_{1/2}(\hat{\mu})^2}, \tag{67}$$

$$F_n(x) \equiv \int_0^\infty \mathrm{d}t\; t^n \left[\mathrm{e}^{t-x}+1\right]^{-1}. \tag{68}$$

A^α is given in equation (25a) of [123], except with a typographical error that F_2 incorrectly reads F_3 there. $\hat{\mu} \equiv \mu/T_\mathrm{e}$ where μ is the electron chemical potential, defined implicitly by $F_{1/2}(\hat{\mu}) = (2/3)\theta^{-3/2}$ with $\theta \equiv T_\mathrm{e}/E_\mathrm{F}$. Antia [3] provides rational function approximations to F_n for several half-integer orders and their inverses, which we use to directly find $\hat{\mu}(\theta)$.

A formula for τ that spans the plasma, neutral-gas, and condensed regimes is

$$\tau = \max(\tau_\mathrm{ec}, \tau_\mathrm{melt}, \tau_\mathrm{min}). \tag{69}$$

$\tau_\mathrm{ec}^{-1} = \tau_\mathrm{ei}^{-1} + \tau_\mathrm{en}^{-1}$ defines the electron collision time off both charged ions (τ_ei) and neutral atoms (τ_en), with rates added. τ_melt and τ_min stem from a Bloch-Grüneisen melting model [229], and a minimum time based on inter-atom spacing $R_\mathrm{i} \equiv (3/4\pi n_\mathrm{i})^{1/3}$. $\tau_\mathrm{en}^{-1} = n_\mathrm{n}\sigma_\mathrm{n}\bar{v}$ where n_n is the number density of neutral atoms, σ_n the cross-section, and $\bar{v} \equiv 3\cdot 2^{-1/2}(T_\mathrm{e}/m_\mathrm{e})^{1/2}\theta^{3/2}F_1(\hat{\mu})$ the average electron speed. The limiting values of $\bar{v}^2$ are $(8/\pi)T_\mathrm{e}/m_\mathrm{e}$ for $\theta \gg 1$ and $(9/8)\epsilon_\mathrm{F}/m_\mathrm{e}$ for $\theta \ll 1$. Approximately, $\tau_\mathrm{min} \approx R_\mathrm{i}/\bar{v}$, and Desjarlais has discussed refinements to this [61]. The melt model gives $\tau_\mathrm{melt} \approx 50(T_\mathrm{melt}/T_\mathrm{e})\tau_\mathrm{min}$, with the material-dependent constant 50 decreasing somewhat for $T_\mathrm{e} > T_\mathrm{melt}$ (see Lee and More for details). The melt model applies to conductors with strong ion correlations, such as a periodic lattice, and not to insulators or gases. In the periodic case, the electron wavefunction becomes a Bloch wave in a periodic potential, and essentially does not undergo Coulomb collisions off single ions. Instead, electrons slow down due to interactions with phonons. As temperature increases and the ions become uncorrelated, Coulomb collisions with ions dominate, and τ_ec applies. Taking the maximum of the three τ's is a crude way of capturing the real, more complicated physics.

We now discuss τ_ei, which falls closest to the realm of traditional plasma physics. We consider one electron species colliding with one ion species; for multiple ion species the collision rates and therefore the η's add. Lee and More find

$$\frac{\eta}{\eta_0} = \frac{1}{3\theta^3 F_2(\hat{\mu})}, \quad \eta_0 \equiv \pi\sqrt{2}\frac{e^2 m_\mathrm{e}^{1/2}}{E_\mathrm{F}^{3/2}}\delta_\mathrm{ee}\frac{n_\mathrm{i}}{n_\mathrm{e}}Z_\mathrm{i}^2\ln\Lambda_\mathrm{ei}. \tag{70}$$

η_0 is the fully-degenerate result, and δ_ee accounts for e–e collisions. In the non-degenerate (Spitzer) limit $\eta = \eta_\mathrm{S}$ with $\eta_\mathrm{S}/\eta_0 = (\pi^{1/2}/8)\theta^{-3/2}$, or $\eta_\mathrm{S} \propto T_\mathrm{e}^{-3/2}$ (neglecting temperature dependence of η_0 via Z_i or $\ln\Lambda_\mathrm{ei}$). An approximate form with the correct small and large θ limits is

$$\frac{\eta}{\eta_0} \approx \left[1+(4\pi^{-1/3}\theta)^p\right]^{-3/2p}. \tag{71}$$

For $p = 1.72$ the relative error in η/η_0 is at most 2% for all θ. Some workers approximately include F–D statistics by capping η at the value at some temperature. The Spitzer η_S equals the fully degenerate η_0 for $\theta = (\pi^{1/2}/8)^{2/3} = 0.366$.

We use the Lee–More Coulomb logarithm:

$$\ln\Lambda_\mathrm{ei} = \max\left(2, \tfrac{1}{2}\ln\left[1+\Lambda^2\right]\right), \tag{72}$$

with $\Lambda \equiv b_\mathrm{max}/b_\mathrm{min}$ the coupling parameter; $\Lambda \gg 1$ for a weakly-coupled plasma. $b_\mathrm{max} = [\lambda_\mathrm{DH}^2 + R_\mathrm{i}^2]^{1/2}$ is the overall screening length. The Debye–Hückel screening length is given by

$$\lambda_\mathrm{DH}^{-2} = \frac{e^2}{\epsilon_0}\left(\frac{n_\mathrm{e}}{\bar{T}} + \sum_i \frac{n_\mathrm{i}Z_\mathrm{i}^2}{T_\mathrm{i}}\right) \tag{73}$$

with $\bar{T} \equiv (T_\mathrm{e}^2 + (4/9)E_\mathrm{F}^2)^{1/2}$. The minimum impact parameter is

$$b_\mathrm{min}^2 = b_\mathrm{min,Q}^2 + b_\mathrm{min,C}^2, \tag{74}$$

$$b_\mathrm{min,Q} \equiv \frac{\hbar}{(12 m_\mathrm{e}\bar{T})^{1/2}}, \tag{75}$$

$$b_\mathrm{min,C} \equiv \frac{e^2}{12\epsilon_0\bar{T}}\frac{\sum_i n_\mathrm{i}Z_\mathrm{i}^2}{\sum_i n_\mathrm{i}Z_\mathrm{i}}. \tag{76}$$

$b_\mathrm{min,Q}$ is the de Broglie wavelength, and $b_\mathrm{min,C}$ is the classical distance of closest approach.

The Lee–More model has proven successful at capturing the results of experiments or more detailed models. Most concrete implementations of Lee–More involve several material-dependent adjustable parameters. They can frequently be chosen to replicate more correct results. Like any semi-analytic model, Lee–More can be applied over wide parameter ranges and usually gives smooth results. Tabulated output from more detailed models can include more physics. The typical drawbacks of tables include the limited parameter range over which they were generated, and the difficulty of tabulating a high-dimension domain (for instance, a dopant ion species of variable concentration increases the table dimensionality).

More sophisticated models than Lee-More exist, and are particularly necessary in the non-plasma regime. One is the Purgatorio code developed at LLNL [193, 220]. It solves the Dirac equation for bound and continuum electron states surrounding a single ion. Transport coefficients like resistivity are found using an extended Ziman formulation [68, 163, 229], and require specification of the ion correlation function, or equivalently the ion structure factor. See [86] for details. A similar approach to transport coefficients is presented in [170].

Figure 14 plots η versus T_e for 1.84 g cm^{-3} beryllium from various models. The solid black curve is from Purgatorio[9]. The ion structure factor used was a combination of the results of Baiko *et al* [9], the one component plasma model, and Debye–Hückel theory. Purgatorio calculates the charge state as well, which increases smoothly with T_e, from 1.5 at room temperature, to 3.2 at 100 eV, and asymptotically approaching 4 for higher T_e. We use Purgatorio's Z_i in the other calculations. Since $Z_\mathrm{i} > 1$ for all T_e we neglect electron–neutral collisions ($\tau_\mathrm{en} \to \infty$). The solid red curve comes from Lee–More's τ_ei for e–i collisions, modified to include e–e collisions ($\delta_\mathrm{ee} \neq 1$). The dashed red curve is the Spitzer η_S ($E_\mathrm{F}/T_\mathrm{e} \to 0$). The solid blue curve is the full Lee-More model, with numerical parameters chosen to give a decent agreement with Purgatorio at low T_e, and with

[9] Data kindly provided by P. Sterne, LLNL.

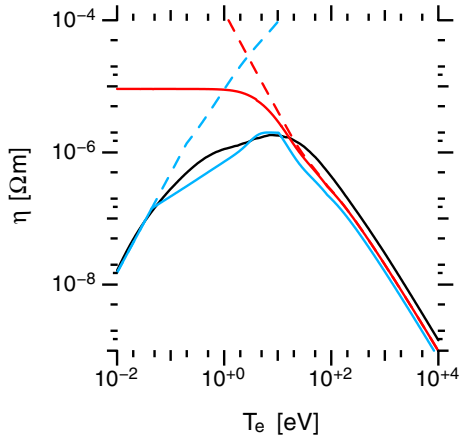

Figure 14. Resistivity for beryllium at density 1.84 g cm^{-3} from various models. See text for details.

e–e collisions neglected ($\delta_{ee} = 1$). This last choice gives a slight difference between the red and blue curves at high T_e. It is easy to include δ_{ee}, but we omit it to demonstrate its magnitude. The dashed blue curve comes from just the melting model $\tau = \tau_{melt}$. Although we have found parameters that bring the Lee–More model into decent agreement with the more complete Purgatorio results for the chosen density, those values are likely not optimal for all densities.

We end this section by briefly discussing when plasma of ICF interest may become strongly coupled, i.e. $\Lambda \sim 1$. Some recent attention has been paid to transport coefficients in this regime [8, 48, 81]. These usually do not consider F–D statistics and connection with the non-plasma state, so that a strongly-coupled generalization of Lee–More is not yet at hand. Following Baalrud [8], strong coupling significantly affects the Coulomb logarithm when $\Lambda < 10$. We assess the potential importance of strong coupling for beryllium, using the Purgatorio Z_i, in figure 15. Panel (*a*) indicates where different terms dominate b_{min} and b_{max}, and panel (*b*) plots Λ including a fit to the $\Lambda = 10$ contour. For instance, we estimate beryllium at 10 g cm^{-3} is strongly coupled for $T_e < 258$ eV. Strong coupling is estimated to be significant below this contour, which includes regimes of interest to FI and high-energy density physics more generally. The correct treatment of this regime, and its impact on the relevant systems, is an open question.

4. Simulation methods

In this section we will review the simulation methods that have been developed for studying FET, and particularly those that are used in the FI context.

4.1. Vlasov–Fokker–Planck codes

The Vlasov–Fokker–Planck (VFP) equation for electrons describes their motion through phase space under the action of the local average Lorentz force and the microscopic field fluctuations that give rise to small-angle collisions with other electrons and ions. It is usually expressed in Cartesian geometry without giving the details of the collisional term [208]:

$$\frac{\partial f}{\partial t} + \boldsymbol{v}\cdot\frac{\partial f}{\partial \boldsymbol{x}} - e(\boldsymbol{E} + \boldsymbol{v}\times\boldsymbol{B})\cdot\frac{\partial f}{\partial \boldsymbol{p}} = \left(\frac{\partial f}{\partial t}\right)_c, \qquad (77)$$

where $\boldsymbol{x}$ and $\boldsymbol{p}$ are the phase space position and momentum coordinates (respectively), $f = f(\boldsymbol{x}, \boldsymbol{p}, t)$ is the electron distribution function, $-e(\boldsymbol{E} + \boldsymbol{v} \times \boldsymbol{B})$ is the Lorentz force and the term on the rhs accounts for the scattering in momentum space due to collisions. When this equation is solved by the use of computational particles it is known as 'collisional particle-in-cell' (collisional-PIC). The collisional-PIC technique has many advantages: robustness; good momentum and energy conservation; no stability or magnitude restrictions in momentum space; very accurate advection in momentum space; and it naturally concentrates computational effort in well-populated regions of phase space. The collisional-PIC technique also has the great benefit of over 40 years of research experience behind it. However, it does suffer one major drawback in that it also introduces noise into the numerical result. The effect of this noise is arguably not yet well-explored in the regime of the dense plasmas that arise in FI research. For this reason a small number of codes based on finite-difference techniques [15, 168, 179] have arisen in recent years. While techniques based on finite-difference in phase space eliminate noise, they do not currently possess most of the aforementioned advantages inherent in the particle approach (and in fact are often deleteriously affected by their converses). Numerical diffusion also occurs (although modern techniques do minimize it) and this may adversely affect the physics. Nevertheless the finite-difference approaches have much merit and also serve as a useful 'reality-check' on the results gained with the particle techniques.

Although the VFP equation is largely valid in FI-relevant plasmas, it should be kept in mind that the collision term requires corrections of order $1/\ln\Lambda$ (the inverse Coulomb logarithm), which should be necessary when the plasma is initially cold and dense. Since the VFP equation is valid over all of momentum space, it is possible to solve it for the distribution function of the energetic particles only, and this is the basis of the VFP-hybrid technique (as used in e.g. [168]), where the background electrons are treated as a simple fluid (see the section on hybrid methods). In fact due to the heavy computational demand of solving the VFP equation, the hybrid technique is by far the most common approach.

Since angular scattering is important for electrons, it is advantageous to use a spherical coordinate system in momentum space, as angular scattering can be easily expressed as diffusion of the distribution function in the angular coordinates. Recasting (77) in two Cartesian space dimensions and spherical-coordinates in momentum space (p, θ, ϕ), and introducing diffusive and drag-like (i.e. in p) collision terms, gives:

$$\begin{aligned}
&\frac{\partial f}{\partial t} + v\cos\theta\sin\phi\frac{\partial f}{\partial x} + v\sin\theta\sin\phi\frac{\partial f}{\partial y} \\
&\quad + F_x\left\{\cos\theta\sin\phi\frac{\partial f}{\partial p} - \frac{\sin\theta}{p\sin\phi}\frac{\partial f}{\partial\theta} + \frac{\cos\theta\cos\phi}{p}\frac{\partial f}{\partial\phi}\right\} \\
&\quad + F_y\left\{\sin\theta\sin\phi\frac{\partial f}{\partial p} + \frac{\cos\theta}{p\sin\phi}\frac{\partial f}{\partial\theta} + \frac{\sin\theta\cos\phi}{p}\frac{\partial f}{\partial\phi}\right\} \\
&= \left(\frac{Y_{ee}n_e}{m_e} + \frac{Y_i n_i}{m_i}\right)\frac{m_e^2}{p^2}\frac{\partial}{\partial p}\left(\gamma^2 f\right)
\end{aligned}$$

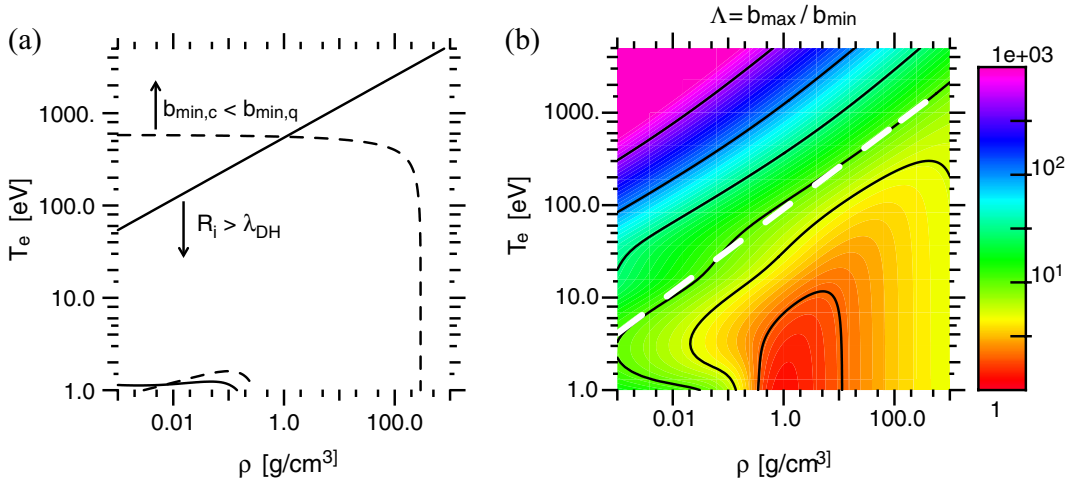

Figure 15. For beryllium: (*a*) where different terms dominate $b_{\min}$ and $b_{\max}$. (*b*) Coupling parameter Λ with black curves for $\Lambda = 2, 5, 10, 30, 100, 500$. White dashed curve is fit to $\Lambda = 10$ contour: $T_e = 1.5\,\mathrm{keV}(\rho/500\,\mathrm{g\,cm^{-3}})^{0.45}$.

$$+\frac{1}{2}\left(Y_{ee}n_e + Y_i n_i\right)\frac{m_e}{p^3} \times\left\{\frac{1}{\sin^2\phi}\frac{\partial^2 f}{\partial\theta^2}+\frac{1}{\sin\phi}\frac{\partial}{\partial\phi}\left(\sin\phi\frac{\partial f}{\partial\phi}\right)\right\}, \tag{78}$$

where

$$F_x = -e\left(E_x - vB_z\sin\theta\sin\phi\right), \tag{79}$$

$$F_y = -e\left(E_y + vB_z\cos\theta\sin\phi\right) \tag{80}$$

are the components of the Lorentz force and $v = p/\gamma m$, $\gamma = \sqrt{1+p^2/m^2c^2}$, $Y_{ee} = 4\pi(e^2/4\pi\epsilon_0)^2\ln\Lambda_{ee}$ and $Y_i = 4\pi(Ze^2/4\pi\epsilon_0)^2\ln\Lambda_{ei}$. The collision terms on the rhs are taken from [102] and are valid for hybrid-VFP simulations only: the first term accounts for the dynamic friction of fast electrons with the cold electrons and ions, while the second term accounts for the angular scattering of fast electrons off cold electrons and ions.

Equation (78) can be readily solved in flux-conservative form, as is done in the FIDO simulation code [179], which uses piecewise-parabolic-interpolation to compute the fluxes combined with the finite-difference time-domain (FDTD) scheme for Maxwell's equations to compute the fields (see e.g. [214]). This treatment is particularly advantageous when the field (acceleration) terms dominate, as is the case when absorption in strong laser fields is modelled.

An alternative form of equation (78) is possible by expanding the distribution function in momentum space in a spherical-harmonic basis:

$$f\left(t,\boldsymbol{x},\boldsymbol{v}\right) = \sum_{n=0}^{N}\sum_{m=-n}^{n} f_n^m\left(t,\boldsymbol{x},v\right)P_n^m\left(\cos\theta\right)\mathrm{e}^{\mathrm{i}m\phi}, \tag{81}$$

where θ is the angle between the velocity vector and the spatial coordinate and the P_n^m are the associated Legendre functions [15]. This gives rise to a large set of coupled partial differential equations for the coefficients:

$$\frac{\partial f_n^m}{\partial t}+\frac{n\left(n+1\right)}{2}\frac{1}{2}\left(Y_{ee}n_e+Y_i n_i\right)\frac{m_e}{p^3}f_n^m - C_{ee} \tag{82}$$

$$= \frac{eB_z}{2m}\left\{\left(n-m\right)\left(n+m+1\right)f_n^{m+1} - f_n^{m-1}\right\} \tag{83}$$

$$-\left(\frac{n-m}{2n-1}\right)v\frac{\partial f_{n-1}^m}{\partial x}-\left(\frac{n+m+1}{2n+3}\right)v\frac{\partial f_{n+1}^m}{\partial x} \tag{84}$$

$$-eE_x\left\{\frac{n-m}{2n-1}G_{n-1}^m+\frac{n+m+1}{2n+3}H_{n+1}^m\right\} \tag{85}$$

$$-\frac{eE_y}{m}\left\{\frac{1}{2n-1}\left[G_{n-1}^{m-1}-\left(n-m\right)\left(n-m-1\right)G_{n-1}^{m+1}\right]\right\} \tag{86}$$

$$-\frac{eE_y}{m}\left\{\frac{1}{2n+3}\Big[-H_{n+1}^{m-1}+\left(n+m+1\right) \times\left(n+m+2\right)H_{n+1}^{m+1}\Big]\right\}, \tag{87}$$

where $G_n^m = \partial f_n^m/\partial p - n f_n^m/p$, $H_n^m = \partial f_n^m/\partial p + (n+1)f_n^m/p$ and C_{ee} accounts for the friction between fast electrons and the background plasma. Equation (87) is for the 1D case only (see [15] for the full 2D equations). This form of the VFP equation has the advantage that it can be solved with relatively fast and simple (for example Runge–Kutta) integration schemes, provided the driving fields are small (in comparison to the laser fields). Numerical schemes that can handle large perturbations to the distribution function are complex and slow. It also allows for a particularly accurate treatment of the magnetic field terms, which are reduced to algebraic form when differenced. This form for the VFP equation was used in, e.g. [13].

4.2. Hybrid Ohmic codes

It is apparent from the disparity between the cold and fast electron characteristics, as described in section 3 that the problem of FET is computationally 'stiff' (disparate length and time scales), and that this also allows a natural separation of the problem into two interlinked models. It is this observation that has motivated the development of the 'hybrid' code. The term 'hybrid code' appears in many places in plasma physics, and the term often denotes very different things. In the case of FET, the term denotes a code in which a kinetic treatment is applied to a distinct fast electron population, and a fluid treatment is applied to a distinct background plasma. It is frequently assumed that the background plasma will respond instantaneously to the fast electrons to ensure quasineutrality,

which is valid on length scales larger than the Debye (or other screening) length. An independent assumption, which we call the ohmic approximation, is that the electric field can be determined from a suitable generalized Ohm's law, with displacement current $\partial_t \boldsymbol{E}$ dropped from Ampère's law. In all cases the magnetic field is evolved from Faraday's law.

This splitting of the populations will only be a good approximation when $n_\mathrm{f} \ll n_\mathrm{b}$, and when the fast electron mean energy is very much greater than the mean thermal energy of the background electrons. In the case of the ultra-intense laser-generated FET problem these conditions will be quite easily satisfied at material densities above 1 g cm^{-3}. Although the fast electron population is very much less dense than the background electrons, the fast electron current density is still sufficiently large to generate electric and magnetic fields with energy densities comparable to the fast electron energy density *unless* there is a compensating return current carried by the background electrons (see section 3.2). This leads to the conclusion that, to a good approximation, $\boldsymbol{j}_\mathrm{f} + \boldsymbol{j}_\mathrm{b} \approx 0$. A more accurate approximation is $\boldsymbol{j}_\mathrm{f} + \boldsymbol{j}_\mathrm{b} \approx \mu_0^{-1} \nabla \times \boldsymbol{B}$. The key equations for $\boldsymbol{E}$ and $\boldsymbol{B}$ in the hybrid approximation then become,

$$\boldsymbol{E} = -\eta \boldsymbol{j}_\mathrm{f} + \frac{\eta}{\mu_0} \nabla \times \boldsymbol{B} \tag{88}$$

and

$$\frac{\partial \boldsymbol{B}}{\partial t} = \eta \nabla \times \boldsymbol{j}_\mathrm{f} + \nabla \eta \times \boldsymbol{j}_\mathrm{f} + \frac{\eta}{\mu_0} \nabla^2 \boldsymbol{B} - \frac{1}{\mu_0} \nabla \eta \times \boldsymbol{B}. \tag{89}$$

The Ohm's law shown in equation (88) can be easily extended to include a number of additional terms (see section 3.5 of this review)—here it is just given in one of the simplest forms. The kinetic treatment of the fast electrons is mathematically described by a suitable kinetic equation, i.e. (77). Usually this is solved by using the standard particle-in-cell (PIC) methods, but with collision operators for the angular scattering from background ions and electrons, and drag from background electrons, included via a Monte Carlo method. The background plasma is described, in general, by a set of hydrodynamic equations, although for some problems it is reasonable to treat the background plasma as essentially static. Even if the background plasma is static, its temperature must evolve due to both ohmic heating of the background electrons, and collisional drag on the fast electrons. These effects must be incorporated into the background electron energy equation.

This must also be accompanied by a prescription for the resistivity. This can be from a theoretical model (Spitzer resistivity or Lee–More), an empirical model, or even a heuristic model. Although the background resistivity is not calculated self-consistently (unlike a purely kinetic model), one advantage of the hybrid approach is that it is relatively easy to use a resistivity model that better treats the 'warm dense matter' regime. This regime is unavoidable both in solid-density interactions and FI, as the resistivity will only be *very* well approximated by the Spitzer resistivity well above the Fermi energy. For DT at 1 g cm^{-3} this would be temperatures above 14 eV.

Although the hybrid approach makes a number of approximations it also has a number of powerful advantages. Firstly the fluid treatment of the background means that the very small length and time scales of the background plasma can be ignored, and thus much larger time-steps can be used which allows large problems to be run quickly. Secondly the model is very computationally robust. Thirdly hybrid codes are easy to write and maintain. Fourthly, hybrid codes allow a lot of physics to be included easily. There are a number of such hybrid codes both in current use and reported in the literature. This includes the unnamed code of Davies [53], PETRA [93], LEDA [168], ZEPHYROS [167], and ZUMA [196, 120]. A limitation to hybrid ohmic approaches is they cannot be applied in regions where Langmuir waves (background electron inertia) or light waves are important, or typically if quasineutrality is violated (recall this is an independent but commonly made approximation). Such situations include LPIs and low-density or vacuum regions surrounding a dense target. This issue is discussed more in the next section.

4.3. Hybrid implicit PIC codes

The implicit PIC algorithm [19] is an alternative method to the ohmic approximation for eliminating fast time scales, namely Langmuir and light waves. The basic idea is to use an implicit time advance, which has the property of numerically damping under-resolved time scales. The equations of motion are not modified, in contrast to the ohmic approximation. Explicit PIC codes generically suffer numerical instability when the plasma period is not resolved, typically when $\omega_\mathrm{pe} \Delta t > 2$. Implicit codes do not have this stability restriction, although of course accuracy is affected by the time step. They require knowledge of the fields at the new time level to advance the particles, in contrast to explicit methods which only use the field at the old time. There are two classes of implicit PIC methods: the direct implicit schemes [43, 75, 119], which relate the fields at the new time to the particle positions and momenta at the new time, and implicit-moment schemes [128], which use only the moments needed in the Maxwell equations (namely ρ and $\boldsymbol{J}$) at the new time. Both implicit methods were originally formulated for electrostatic systems and have been extended to electromagnetic ones: see [89] for direct implicit and [24] for implicit moment.

Several implicit PIC codes are being applied to FI and short-pulse LPI problems. These include the electromagnetic implicit-moment code ePlas [129, 130], and the relativistic, electromagnetic, direct-implicit code ELIXIRS [65]. LSP is a one-, two-, and three-dimensional particle-in-cell (PIC) code developed by Mission Research Corporation [217] and currently maintained by Voss Scientific [209, 218]. LSP has a hybrid mode, as well as several types of electromagnetic field solution available: the standard (explicit) leapfrog algorithm and direct-implicit algorithms using iterative alternate-direction implicit (ADI), a two-step ADI, and matrix inversion. LSP uses a partial implementation of the electromagnetic algorithm of [89], lacking the so-called implicit magnetization term. The implicit algorithms, particularly the two-step ADI, are useful in relaxing the Courant limit on the time step. An iterative electrostatic algorithm is also available for simulations in which fields are slowly varying.

LSP has several options for advancing particles: the standard momentum-conserving and energy-conserving PIC algorithms, cloud-in-cell (CIC) algorithm, and direct-implicit algorithm which can be used in either the PIC or CIC models. The direct-implicit algorithm is used most often. The benefits

of the direct-implicit algorithm are that the usual charged particle limitations on the time step, namely the need to resolve the cyclotron and plasma frequencies, are relaxed although both frequencies cannot be under resolved at the same time and position. The implicit algorithm is useful for very dense plasmas (that occur in FI studies) where the details of electron plasma oscillations can be ignored.

The energy conservation as well as the speed of the direct-implicit calculation is further improved by including a non-relativistic inertial fluid model for the electrons in which the directed and thermal energy of the electrons are treated separately. The equation of motion for the fluid electrons is of standard Braginskii type [25]. It includes a frictional force to model collisions with other particle species. For temperature, the new energy equation for an ideal gas is added including the pdV work, energy exchange between species, thermal conduction, and ohmic heating rate. Inelastic losses with neutrals can also be included. In some circumstances, kinetic effects become important. Examples include runaway, where a hot electron population coexists with a thermal one, or acceleration of less dense electrons or ions from a biased plasma. In the hybrid mode, LSP permits dynamic reallocation of particles between the fluid and kinetic description. Fluid particles with directed energy much greater than thermal energy transition to kinetic particles. Kinetic particles with energy less than the ambient fluid thermal energy transition to fluid particles. These transitions result in energetic electrons treated kinetically and dense thermal plasma electrons as a fluid.

The LSP simulations include an algorithm to model electron–electron, ion–ion and electron–ion collisions. For kinetic particles, this involves first constructing drifting Maxwellian distributions at each grid cell. A particle of a given species is then elastically scattered isotropically in the centre-of-mass frame off a particle obtained by sampling this distribution. Collisions between different species (both kinetic and fluid) are separated into an energy push and a frictional momentum push. The energy and momentum transfers from one species to another are accomplished by summing the changes from each interaction on the grid. The collision frequencies are determined from the Spitzer formulation. Optionally, the more accurate Lee–More [123] model with Desjarlais corrections [61] is available for collisions of fluid electrons and background ions with the ion charge state calculated with a Thomas-Fermi EOS with pressure ionization corrections. Monte Carlo type scattering model with the drag and scattering formulas of [6, 189] is also available for collisions of kinetic electrons and background plasma electrons and ions.

The hybrid implicit approach to dense plasma modelling is alternative to that of hybrid ohmic codes, described in the previous subsection. In those codes, the background plasma is modelled as a collisional fluid and charge neutrality is assumed. The electric field is found from Ohm's law and the background return current is found from Ampère's law without displacement current. This reduced-model approach is inapplicable to LPIs, or low-density regions with, e.g., Debye sheaths. The hybrid implicit model solves full Maxwell equations with displacement current and is applicable in the LPI and low-density regions, provided a kinetic description for plasma electrons is used there (while a fluid description can be used elsewhere in the same run). Time steps and cell sizes can be chosen that resolve the LPI near the critical surface. These time steps, while explicit in the LPI region (electron density, $n_e = 1.1 \times 10^{21}$ cm^{-3} for 1 μm laser light), can be still highly implicit to the plasma frequency in the solid-density target ($n_e > 10^{23}$ cm^{-3}). The entire process of laser propagation into the underdense plasma, fast electron production and transport into the dense plasma, and ion acceleration from the plasma–vacuum interface can be modelled with LSP [218].

Detailed EOS and multi-group diffusion radiation transport modelling capability was recently implemented in the LSP framework with fluid particles [209]. The EOS and opacity data needed for the algorithm are pre-calculated by the Propaceos code [124], which utilizes detailed atomic models for plasmas in local thermodynamic equilibrium (LTE) as well as non-LTE states. The EOS model is used to evolve the ion charge state and introduce non-ideal gas behaviour. The radiation energy density field is calculated, which is coupled to the plasma.

5. Review of ignition scale calculations

This section summarizes the FI calculations carried out so far, showing the dependence of the ignition energies on the electron beam parameters. Electron-driven FI modelling relies on the characterization of the fast electron source, the transport from the generation zone to the compressed core and the energy deposition in the fuel. Thus, the complete description of FI requires the integration of different models/codes that deals with different spatial and temporal scales. Fully integrated calculations are not possible with the present computer resources. Here, we focus our attention on the partially integrated calculations that consist of characterizing the fast electron source via experiments or PIC simulations and using this source to perform FET calculations coupled to radiation-hydrodynamics, including fusion reactions. This 'integrated' model has been used so far to estimate the electron beam requirements in the FI scenario [96, 186, 196]. Relativistic Fokker-Planck models for electron transport in sub-ignition targets have been developed also within the context of the FIREX-I project [224].

5.1. Ignition energies of perfectly collimated electron beams

We assume for the moment that a perfectly collimated beam impinges on a DT assembly at a time close to the peak compression. Here, we do not take into account the fast electron scattering nor the EM fields generated by the electron beam. We first consider the target proposed by Solodov *et al* with a DT mass of 0.5 mg compressed by a 300 kJ nanosecond laser pulse to a peak density of 500 g cm^{-3} [190]. Assuming a mono-energetic electron beam of 20 μm radius and a pulse duration of 10 ps, the lowest ignition energy $E_{ig} = 16.2$ kJ is reached for 2 MeV electrons [190]. This ignition energy is much higher than the 7 kJ obtained from equation (1) for $\rho = 500$ g cm^{-3} due to the target density profile and also because the beam radius and pulse duration do not have the optimal values given by equations (2)–(4). For the more realistic case of electrons with a relativistic-Maxwellian energy spectrum, the lowest ignition energy raises

to 21.5 kJ for an electron mean energy $\langle E\rangle = 1.25$ MeV. This energy is substantially lower than the 2 MeV found for mono-energetic beams because Maxwellian electrons deposit their energy over a larger region. In addition, it is much lower than those obtained in experiments and PIC simulations for laser intensities around 10^{20} W cm^{-2}. More realistic electron energies can be obtained by using the ponderomotive scaling formula $\langle E\rangle/m_ec^2 = [1 + I_L\lambda^2/1.38 \times 10^{18}]^{1/2} - 1$, which relates the laser intensity I_L (in W cm^{-2}) and wavelength λ (in μm) with the electron mean energy $\langle E\rangle$ [219]. For instance, let us consider a Gaussian laser pulse with a duration of 13.8 ps and $\lambda = 1.054$ μm impinging on the fuel assembly mentioned above. Assuming that the electron mean energy is given by the ponderomotive scaling and a laser-to-fast electron conversion efficiency of 50%, one obtains $\langle E\rangle = 6.3$ MeV and an ignition energy $E_{ig} = 53$ kJ [190]. We emphasize that the ignition energies mentioned above have been obtained under the strong assumptions of electron straight path, no beam divergence and without accounting for the self-generated EM fields. Atzeni *et al* estimated that the scattering effects raise the ignition energy by about 20% [6]. Thus, even for the ideal conditions assumed here, electron beam energies of several tens of kJ are needed to ignite a target. Similar results have been obtained for the all-DT target design proposed for the HiPER project [7].

5.2. Ignition energies of divergent electron beams with an assumed initial distribution function

More realistic calculations can be performed by means of the partially integrated model mentioned above. In this model, the beam parameters are estimated from experiments or PIC simulations conducted at laser intensities and/or pulse durations lower than those required for FI. The main features of the relativistic electron source considered so far in FI simulations can be summarized as follows:

(i) *Energy spectrum*. It is normally assumed that the electron spectrum is given by the exponential distribution obtained in PIC simulations for sub-ps pulses. Relativistic-Maxwellian spectra have been used also. Both distributions depend on the fast electron temperature or electron mean energy $\langle E\rangle$, typically fitted to experiments. For laser intensities $<10^{19}$ W cm^{-2}, the so-called Beg's law $\langle E\rangle = 150(I_{17}\lambda^2)^{1/3}$ is used, where $\langle E\rangle$ is in keV, I_{17} is the laser intensity in units of 10^{17} W cm^{-2} and λ the laser wavelength in μm [11]. For intensities around 10^{19} W cm^{-2} or higher, the ponderomotive scaling [219] reproduces well experiments and PIC simulations. However, it gives electron energies well over the desired values around 2 MeV for the laser intensities typical of the FI regime ($>10^{20}$ W cm^{-2}).

Chrisman *et al* [42], Haines *et al* [85] and Kluge *et al* [114] have recently reported scaling laws that provide electron energies lower than those obtained by the ponderomotive scaling and of the same order than those predicted by the Beg's law. In principle, this is very favourable for FI because the optimal electron range is about 1.2 g cm^{-2} [5], which corresponds to an electron energy lower than 2 MeV [189] and a laser intensity about 2.4×10^{20} W cm^{-2} assuming the Beg's scaling. Unfortunately, as it is discussed in section 5.3, recent 3D PIC simulations have revealed that the mean energy of relativistic electrons is similar to that given by the ponderomotive scaling and their spectrum differs substantially from the exponential or relativistic-Maxwellian distributions mentioned above [196].

(ii) *Beam divergence*. In most of the fast electron calculations carried out so far it has been assumed that the electron divergence is given by the beam effective propagation angle measured in the experiments. However, as electrons propagate in metals or plastics, whose resistivity is several orders of magnitude higher than that of the DT fuel, resistive collimation effects can be important [13]. In this case, the initial fast electron divergence turns out to be substantially higher than the effective propagation angle measured [82, 144, 192]. For instance, to reproduce the full propagation angle of 35° found in the experiments conducted by Green *et al* [82], an initial electron divergence half-angle as large as 50° has to be assumed in hybrid calculations [96]. Recent PIC simulations have shown initial divergence half-angles of 50°–55° for FI conditions [196]. Thus, guiding mechanisms should be envisioned for these highly divergent beams in order to have a good coupling efficiency with the dense fuel.

It is also important to account for the dependence of the divergence angle on the electron kinetic energy observed in PIC simulations. It can be taken into account in a simplified fashion by assuming that the initial divergence angle is given by the ponderomotive scaling $\tan\theta = [2/(\gamma-1)]^{1/2}$ [158], where θ is the polar angle and γ the relativistic Lorentz factor. It is conjectured that an electron of energy $(\gamma - 1)m_ec^2$ is emitted with a divergence half-angle randomly selected between 0 and θ. Thus, high-energy electrons are well collimated while low energy electrons have an almost isotropic distribution. This dependence on electron energy is important to get a reasonable high-energy coupling between the beam and the dense fuel. However, recent 3D PIC simulations have shown that the energy spectrum and the angular distribution of the fast electron source are independent of each other, i.e. the divergence angle is the same for all electrons [196]. This implies a strong increase of the ignition energies when compared with those obtained from the ponderomotive scaling.

(iii) *Beam radius*. Experiments and PIC simulations of relativistic LPI with foil targets show that the size of the FEB is greater than that of the laser beam [192]. This effect has to be taken into account in FET calculations [94]. In the case of electron acceleration in re-entrant cones, it is found that the radius of the beam is approximately equal to the cone outer radius. This is also true in the double cones described in section 6.7, where the vacuum layer between the two cone walls force fast electron propagation towards the cone tip [36, 58, 59, 142].

(iv) *Conversion efficiency*. The laser-to-fast electron conversion efficiency obtained in PIC simulations ranges from 30% to 50% for the electron energies relevant for FI, e.g. $E > 250$ keV [57, 196].

As an example of the ignition calculations assuming an initial fast electron distribution carried out so far, let us discuss the ignition energies of the idealized DT fuel configuration shown in figure 16(*a*) [96]. It is assumed that the fast electron energy and divergence are given by the ponderomotive formulas with $\lambda = 0.527$ μm multiplied by a scale factor. Despite it is technologically challenging, the 2nd harmonic of

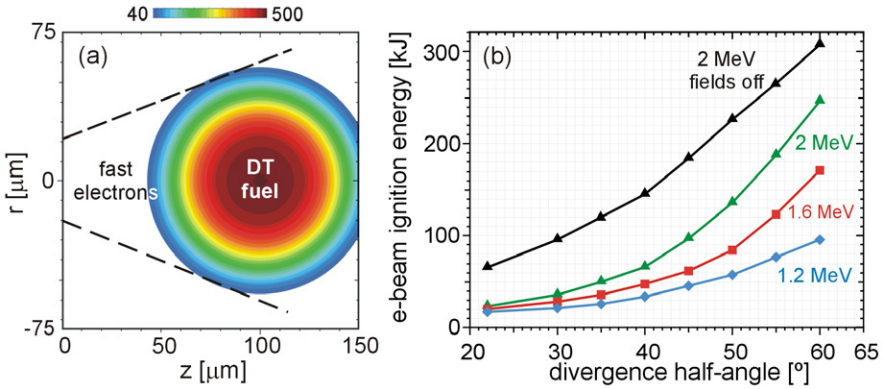

Figure 16. Left: (*a*) initial target density in g cm^{-3}. The halo surrounding the dense core has a density of 2 g cm^{-3}. Right: (*b*) electron beam ignition energies as a function of the divergence half-angle and the electron mean energy $\langle E\rangle$. The beam parameters for the case (35°, 1.6 MeV) are 20 μm radius (HWHM) and 18 ps pulse duration (FWHM). Reprinted with permission from [96]. © 2009 IOP Publishing.

the Nd laser has been considered to reduce the electron energy [96, 186, 196]. The DT fuel has an initial super-Gaussian density distribution, $498\exp\{-(R/45)^4\}$ g cm^{-3} where R is the distance to the centre in μm, sited on a density pedestal of 2 g cm^{-3}. The total DT mass is 0.39 mg and the initial temperature 300 eV. As the cone tip is not included in the simulation box, its effect on FET (beam filamentation, scattering and energy loss) is accounted for indirectly via the initial fast electron distribution function. Calculations have been performed with the hybrid code PETRA for FET [95] coupled to the radiation-hydrodynamics code SARA [97] run in 2D Eulerian mode and cylindrical r–z geometry.

Fast electron energy deposition takes place via ohmic heating due to return currents and classical Coulomb scattering (collisional drag). Ohmic heating is important only in the low-density DT plasma, while collective behaviour is suppressed and energy deposition takes place almost exclusively by collisional drag in the dense core [96, 102, 186, 196]. It is important to emphasize that collective effects may play a major role for core heating, but in an indirect way: self-generated resistive B-fields may collimate the relativistic beam improving the coupling efficiency substantially. However, as the beam collimation decreases strongly with the electron divergence angle, equation (9) [13], its importance in the FI scenario will depend on the full characterization of the fast electron source, which is not possible today neither by experiments nor PIC simulations. Anyway, it is very beneficial for FI: without resistive collimation there is little hope to ignite a precompressed target with reasonable electron beam energies due to their high divergence. For instance, figure 16(*b*) shows the rapid increase of the ignition energy with the electron divergence half-angle, which can be explained by the geometrical effect and the lower beam collimation. In section 5.3, it will be shown that beam collimation has only a marginal importance in the FI scenario when realistic fast electron distributions computed from 3D PIC simulations are assumed.

In addition to the beam collimation, resistive filamentation is the other collective effect that can play a role in electron-driven FI. It has been observed in the simulations of the ideal target shown in figure 16(*a*) [93], the imploded targets of [186] and the experiments with solid and compressed plastic targets analysed in [187]. It was found also in Fokker–Planck simulations of sub-ignition targets [102]. Its effects on fuel ignition have not been studied in detail yet.

The minimum ignition energies of the target of figure 16(*a*) as a function of the initial divergence half-angle with the mean energy as a parameter are shown in figure 16(*b*). For small divergences, the beam is strongly collimated and the ignition energies are even lower than those obtained in section 5.1 for perfectly collimated beams. For higher divergences, the beam collimation is less important and ignition energies increase more than proportionally with the divergence half-angle. It is worth noting that, even for the ideal case shown in figure 16, to get ignition with a 50 kJ electron beam requires a substantial reduction of the divergence half-angle, from the 50°–55° obtained from experiments and PIC simulations to the 35° shown in figure 16(*b*) for 2 MeV electrons. The ignition energies obtained with self-generated resistive fields artificially supressed are also shown for comparison. Note that those fields are not negligible even for relatively large divergencies, resulting in a beam effective propagation angle substantially lower than the electron divergence angle. However, this effect is lower for large divergencies, as shown in figure 16(*b*).

Similar calculations have been reported by Solodov *et al* for the direct-drive capsule mentioned in section 5.1 [190]. Simulations have been performed with the hybrid-PIC code LSP [217] coupled to the radiation-hydrodynamics code DRACO [159]. A relativistic electron beam is injected 125 μm from the target centre at a time when the maximum DT density is slightly above 500 g cm^{-3}. Assuming that beam electrons have a relativistic-Maxwellian distribution with a mean energy of 2 MeV and a divergence half-angle of 20° (HWHM), Solodov *et al* found a minimum ignition energy about 43 kJ [186]. They also found an important resistive collimation of the FEB. The ignition energy increases strongly with the divergence half-angle θ, being 63 kJ and 105 kJ for $\theta = 30°$ and 40°, respectively. These energies are higher than those shown in figure 16(*b*) due to the higher stand off distance between the electron injection surface and the target centre (125 versus 100 μm) and the higher areal density of the coronal plasma surrounding the core of the imploded target [186]. For instance, figure 16(*b*) shows that the ignition energy for a beam with $\langle E\rangle = 2$ MeV and $\theta = 35°$ is 50 kJ while it is around 80 kJ

for the target of [186]. Assuming in this last case a laser-to-fast electron conversion efficiency of 40%, even with the strong assumptions of no cone tip and a divergence half-angle of 35° only, a multi-PW laser with more than 200 kJ would be needed to ignite such a target.

The calculations presented in [96, 186] are quite ideal because fast electrons are injected just on the coronal plasma surrounding the fuel assembly. Indeed, fast electrons have to pass through the overcritical plasma sited inside the cone, if any, and always through the cone tip before reaching the dense fuel. Johzaki *et al* [102, 103] have studied the role played by the cone tip in the FET towards the dense core. They conclude that high-Z materials deteriorate substantially the quality of the electron beam even for cone tips as thin as 10 μm. This is due to the collisional drag with plasma electrons and scattering with ions, resulting in an important reduction of the energy coupling of the FEB to the dense core. The use of lighter materials in the cone tip, such as CH or diamond-like carbon (DLC), mitigates drag and scattering effects. These light materials produce a manageable degradation of the beam and, at the same time, can support the shock and the jet coming towards the cone at the shell collapse time. DLC is preferred to the CH for its higher density.

The effect of the cone tip material in sub-ignition targets has been quantified by Johzaki *et al* within the context of the FIREX-I project [102]. The simplified target configuration considered in this project is a CD plasma with a Gaussian density profile in radius (peak density = 200 g cm^{-3}, FWHM diameter = 20 μm) placed on a density pedestal of 0.2 g cm^{-3}. The target areal density is 0.2 g cm^{-2} and the initial temperature is set to 400 eV. This imploded target configuration is heated during 5 ps by a 5 kJ, 1 MeV FEB with a Gaussian radial profile of 30 μm diameter (FWHM). The beam divergence full angle is 20° and the electrons are injected 50 μm away from the core centre. As the electron beam size is comparable to the imploded core size and the electron range is higher than the target areal density, a hot spot is not generated and, instead, the whole core is heated. Johzaki *et al* have shown a reduction of about 50% in the core heating energy and 60% in the peak ion temperature when a 10 μm thickness gold tip is present. This reduction is much lower, 10% and 11%, respectively, for lighter materials such as CH [102].

Another issue that can affect dramatically the FEB coupling with the dense core is the existence of plasma inside the cone. As has been reported by Johzaki *et al* [104], the ASE (amplified spontaneous emission) laser pre-pulse generates a long scale, low-density plasma inside the cone. As a result, fast electrons are generated by the interaction of the main pulse with the pre-plasma relatively far from the cone tip and with much higher energy than without pre-plasma. This has been confirmed by PIC simulations [104], which have shown harder electron spectra and a substantial reduction of the number of electrons with energies lower than 5 MeV when a pre-plasma is present. Too hot electrons reduce substantially the electron energy deposition in the core and thus the coupling efficiency. Integrated FI experiments carried out at the ILE have evidenced this effect, observing a coupling efficiency substantially higher when the laser pre-pulse energy is reduced [180].

An improvement of the standard field calculation model used in FET calculations has been proposed recently by Johzaki *et al* [102] and Nicolai *et al* [143]. They have pointed out that the generalized Ohm's law and, in particular, the pressure gradient term, which yields an azimuthal B-field proportional to $\nabla T_e \times \nabla n_e$, can play a role in transport calculations. This term is important when the directions of the gradients of electron temperature, ∇T_e, and electron density, ∇n_e, are not parallel, as occurs at the outer regions of the core (see figure 16(a)), where the electron temperature gradient is directed towards the beam axis and the density gradient is directed towards the core centre. The B-field due to $\nabla T_e \times \nabla n_e$ has a direction opposite to the resistive collimating B-field mentioned above and its main effect is to scatter electrons away from the core. However, the growth of this B-field is relatively slow becoming important after several ps. For instance, the energy deposition in the target depicted in figure 16(a) heated by the beam defined by the parameters $\theta = 35°$ and $\langle E \rangle = 1.6$ MeV is reduced by 23% when the generalized Ohm's law is taken into account [143]. A similar reduction (21%) has been found in the calculations for the simplified FIREX-I target discussed above when the term $\nabla T_e \times \nabla n_e$ is included [102].

5.3. Ignition calculations with a PIC-based electron source

A first characterization of the fast electron source in the FI scenario via 3D PIC simulations has been reported recently [111, 196]. One of the main conclusions of this study is that the initial distribution of fast electrons can be factorized as the product of two independent functions of angle and energy. The angular distribution is super-Gaussian, $\exp\{-(\theta/\Delta\theta)^4\}$, with $\Delta\theta = 90°$ and a mean divergence half-angle $\langle\theta\rangle = 52°$. This high divergence can be explained by the curved geometry of the electron acceleration region [175] and by the electron scattering by the oscillating magnetic field generated by the Weibel instability close to the cut-off surface [2, 59]. The energy spectrum can be fitted by a quasi two-temperature profile. The first component is due to electron acceleration near the cut-off surface and has a temperature substantially lower than that given by the ponderomotive scaling T_p, while the second component is due to electron acceleration in the subcritical plasma and has a temperature higher than T_p. The overall electron mean energy is slightly higher than the ponderomotive temperature T_p, but only 24% of the injected energy is carried by electrons with energies lower than T_p. The main differences with the electron source assumed in section 5.2 are the much higher electron energies and divergences, and the energy independent angular spectrum. It is worth pointing out how the PIC source is fed into transport codes. In [196], hot electrons are injected in a 3D 'source box' chosen such that, after propagating some distance, electron distribution function matches that found in PIC simulations. This procedure can be simplified by injecting hot electrons on a plane with a radially outward drift [59] or following the sophisticated technique described in [12].

Strozzi *et al* [196] have performed integrated simulations assuming the PIC-based electron source presented above. The target used is shown in figures 17(a) and (b), where the DT fuel has initially a super-Gaussian density distribution, $440\exp\{-(R/70)^{12}\}$ g cm^{-3} where R is the distance to the centre in μm, sited on a background DT plasma of 10 g cm^{-3}. A DLC cone is included in the simulation box. The DT mass is

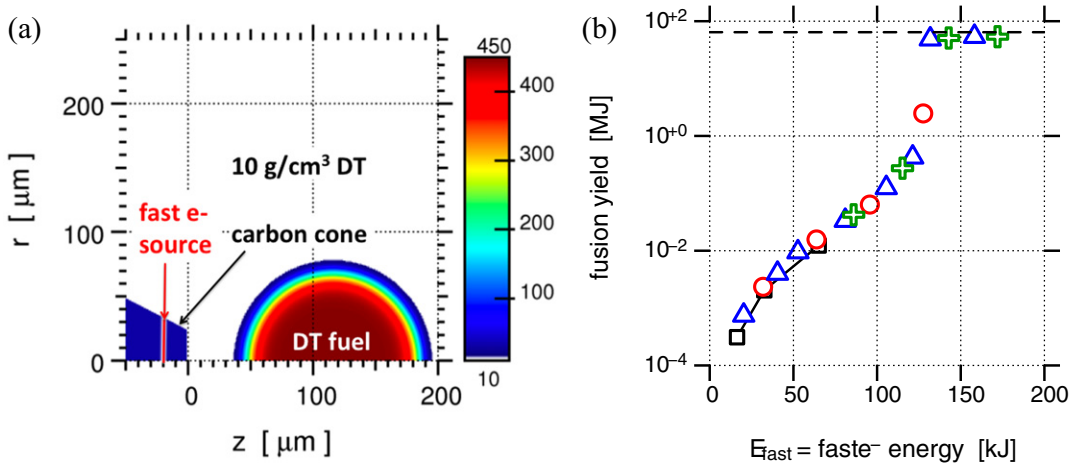

Figure 17. (*a*) Initial target density in g cm^{-3}. The red line indicates the source cylinder where fast electrons are injected. The 8 g cm^{-3} (=2.3 × solid diamond) carbon cone is coloured in blue for clarity. (*b*) Fusion yield versus total injected electron energy, for Zuma–Hydra runs with an artificially collimated source $\Delta\theta = 10^{\circ}$. $r_{\rm beam} = 10\,\mu$m for black squares with solid line, 14 μm for red circles, 18 μm for blue triangles and 23 μm for green crosses. The blue triangle with $E_{\rm fast} = 132$ kJ is the lowest value that can be deemed to be ignited. Reprinted with permission from [196]. © 2012 American Institute of Physics.

0.57 mg and the initial temperature is set to 100 eV. An electron beam with quasiuniform radial profile, $\exp\{-\ln 2(r/r_{\rm beam})^8\}$ with $r_{\rm beam} = 18\,\mu$m, and constant intensity in time (from 0.5 to 18.5 ps, starting from a linear ramp from 0 to 0.5 ps) impinges on the target. The transport and energy deposition of fast electrons from the cone to the core has been simulated with the hybrid-PIC code Zuma [120] coupled to the radiation-hydrodynamic code Hydra [126]. The Zuma code includes the generalized Ohm's law. The details are given in [196].

The fusion yield as a function of the fast electron energy for an artificially collimated electron source ($\Delta\theta = 10^{\circ}$) and for several values of $r_{\rm beam}$ is shown in figure 17(*b*). It is worth noting that, despite the artificial source collimation, the minimum ignition energy is quite high, 132 kJ and roughly independent of the beam radius. This can be explained by taking into account that for large radii, the increase in the volume to be heated is balanced by the lower energy and penetration of fast electrons due to the lower laser intensity. Assuming the laser-to-fast electron conversion efficiency of 0.52 obtained in the PIC simulations, the 132 kJ electron beam corresponds to a laser mean intensity of about 1.4×10^{21} W cm^{-2}, which gives an electron mean energy of 8.2 MeV and a range (6.8 g cm^{-2}) greater than the fuel ρL (6 g cm^{-2}) and much higher than the optimal deposition range for FI (1.2 g cm^{-2}). This is one of the reasons why the ignition energy is so high. We can conclude that, even if a collimated electron beam could be generated, the ignition energy would be unacceptably high because fast electrons are too hot. When the fast electron divergence is included, simulations show ignition energies higher than 1 MJ [196], making FI unfeasible, at least for the 'conventional' scheme discussed in this Section. The major limitations of the calculations presented here arise from the short time of the 3D PIC simulations (~0.36 ps), much lower than the 10–20 ps pulse durations typical of FI, and from the lack of comparison with experimental data close to the true FI conditions.

As a continuation of the work of Strozzi *et al* and using the same simulations codes Zuma and Hydra, Bellei *et al* [12] have performed recently a parametric study of the ignition energy as a function of the source-fuel distance, source size and density of the precompressed fuel. Fast electron source has been characterized again from 3D PIC simulations with an improved method for hot electron data extraction from the PIC code and injection into the transport code Zuma. Bellei *et al* show the benefit of increasing the source spot size in order to lower the hot electron mean energy. However, the electron beam ignition energies found in their study, above 250 kJ (≈500 kJ of laser energy) for a distance source-fuel of 25 μm, are still too high to make attractive the *classical* FI scheme discussed here. Bellei *et al* conclude the necessity of modifying the phase space of the fast electrons *before* propagation in the DT fuel. Some techniques for so doing are summarized in the next section.

6. Concepts for controlling transport

6.1. Motivation

From the preceding sections it is clear that large fast electron divergence angles can severely reduce the fast electron to hot-spot coupling efficiency, thus raising the required ignitor pulse energy to levels at which FI is no longer a viable ICF scheme. In the first instance this is just a consequence of ballistic transport. Suppose that all other processes can be neglected, and that coupling is therefore dominated by ballistic transport with ideal stopping in the hot spot. When the stand-off distance, D, is much larger than the source spot radius, $r_{\rm L}$, one would therefore expect the coupling efficiency, χ, to be roughly equal to the hot-spot area divided by the FEB cross-section at the stand-off distance, which is,

$$\chi = \frac{r_{\rm hs}^2}{2D^2(1-\cos\theta_{1/2})}. \qquad (90)$$

If $\theta_{1/2}$ is large then χ is limited to $\chi \approx r_{\rm hs}^2/D^2$. For $r_{\rm hs}/D = 0.2$ this is 5%. Conversely, equation (90) indicates that for $r_{\rm hs}/D = 0.2$, one needs $\theta_{1/2} = 16.3^{\circ}$ to obtain $\chi = 0.5$. Assuming that the laser-absorption physics cannot be easily engineered to produce such a low divergence angle,

there is a clear need to seek additional means of controlling the transport of the fast electrons.

In the first instance this might be 'self-collimation' of the FEB through the resistively-generated magnetic field that should be produced around the FEB (see section 3.2). The ability of this field to produce significant focussing or pinching of the FEB is at least doubtful in light of experimental and simulation results that have been obtained in the last few years.

If self-collimation cannot be relied upon, then the FI scheme has to be adapted in some way so as to ensure effective transport of the fast electrons by some other means (if at all possible). This might be possible through optical engineering of the laser pulse and a thorough understanding of the laser-absorption process. Alternatively it might be possible to exploit FET physics, and it is this that this section is concerned with.

6.2. Self-collimation of the FEB

In section 3 of this review, the criteria are presented for a FEB to 'self-collimate' as derived and studied in the work of Bell and Kingham. By this, we mean the collimation of a FEB even in a homogeneous background plasma due to the resistive magnetic field that is generated due to the curl of the fast electron current density, and thus the curl of the electric field. A simplified version of the Bell-Kingham criteria can be derived as follows. One starts with an estimate of the magnetic field that is resistively generated,

$$\frac{\partial B}{\partial t} \approx \frac{\eta j_{\mathrm{f}}}{R}, \tag{91}$$

where R is the beam radius, j_{f} the fast electron current density, η the resistivity and t is the time. If we use the Spitzer resistivity ($\eta = \alpha T^{-3/2}$), then this can be integrated to obtain,

$$B \approx \frac{3n_{\mathrm{e}}}{2j_{\mathrm{f}}R}\left[at + T_0^{5/2}\right]^{2/5}, \tag{92}$$

where $a = 2\alpha j_{\mathrm{f}}^2/3en_{\mathrm{e}}$, and T_0 is the initial temperature. Next one estimates the angle (θ) that a fast electron will be deflected through over the distance that the unperturbed beam takes to double its radius,

$$\theta = \frac{eBR}{\gamma m_{\mathrm{e}} c \tan\theta_{1/2}}, \tag{93}$$

where $\theta_{1/2}$ is the divergence half-angle of the beam. If we use the fundamental Bell–Kingham criterion for collimation—that collimation occurs when $\theta = \theta_{1/2}$—then we can combine equations (91) and (93) (and substitute power balance for j_{f}) to obtain

$$\theta_{1/2}\tan\theta_{1/2} = \frac{3en_{\mathrm{e}}\bar{\varepsilon}}{\gamma m_{\mathrm{e}} c\beta I_{\mathrm{L}}}\left[at + T_0^{5/2}\right]^{2/5}, \tag{94}$$

where β is the laser to fast electron conversion efficiency, I_{L} is the laser intensity, and $\bar{\varepsilon}$ is the average fast electron energy. Inserting typical numbers into equation (94) leads to the conclusion that self-collimation is only likely to happen for $\theta_{1/2}$ <20–30°, e.g. DT ($Z = 1$) at $1\,\mathrm{g\,cm^{-3}}$, $I_{\mathrm{L}} = 2\times10^{20}\,\mathrm{W\,cm^{-2}}$, $\beta = 0.3$, $\bar{\varepsilon} = 1.7\,\mathrm{MeV}$ implies $\theta_{1/2} = 27°$ for collimation.

Calculations of FET relevant to ignition scale FI indicate that this is a reasonable estimate for the regime in which self-collimation is sufficient (e.g. [96]; see section 5). There is good evidence, however, that the actual fast electron divergence half-angle under ignition-scale conditions will be significantly greater than 30°. Some of this evidence is experimental [82, 118] coupled with theoretical and numerical interpretation [96]. Other evidence comes from large-scale numerical simulations of laser absorption, e.g. [59, 111]. With divergence half-angles that are slightly in excess of 30°, magnetic field generation is still highly beneficial in terms of improving the coupling. However the evidence suggests that the divergence half-angle could be in excess of 50°, and under these conditions self-collimation does little to prevent very poor coupling to the hot spot (for typical stand-off distances).

6.3. Resistive guiding of fast electrons

From the induction equation in the hybrid approximation,

$$\frac{\partial \boldsymbol{B}}{\partial t} = \eta\nabla\times\boldsymbol{j}_{\mathrm{f}} + \nabla\eta\times\boldsymbol{j}_{\mathrm{f}}, \tag{95}$$

one can see that just as there is a term which indicates that magnetic field grows to drive fast electrons into regions of higher fast electron current density (first term), there is also a term that indicates that magnetic field grows to drive fast electrons into regions of higher resistivity (second term)[10]. The $\eta\nabla\times\boldsymbol{j}_{\mathrm{f}}$ term is the effect responsible for the 'self-collimation' described in the preceding section.

Resistive guiding exploits the second term, the $\nabla\eta\times\boldsymbol{j}_{\mathrm{f}}$ term [168]. At sufficiently high temperatures, all materials will follow a Spitzer-like resistivity in which $\eta \propto Z$. Therefore if one structures a target by using two materials with different Z, in principle the higher Z material should confine and guide the fast electrons as magnetic fields are generated at the interface between the two materials where the $\nabla\eta\times\boldsymbol{j}_{\mathrm{f}}$ term will be large.

It is relatively straightforward to see that the collimating fields generated by resistivity gradients must be at least as strong as those generated by the $\eta\nabla\times\boldsymbol{j}_{\mathrm{f}}$ term. If we denote the $\eta\nabla\times\boldsymbol{j}_{\mathrm{f}}$ term by $\dot{B}_1$, and $\nabla\eta\times\boldsymbol{j}_{\mathrm{f}}$ by $\dot{B}_2$, then we can see that the magnitudes are approximately,

$$\dot{B}_1 \approx \frac{\eta j_{\mathrm{f}}}{R_{\mathrm{b}}}, \tag{96}$$

$$\dot{B}_2 \approx \frac{\eta j_{\mathrm{f}}}{L_{\mathrm{int}}}, \tag{97}$$

where R_{b} is the radius of the FEB, and L_{int} is the scale-length associated with the transition in resistivity. As it is possible to envisage transitions in resisitivity with scale-lengths, $L_{\mathrm{int}} \ll R_{\mathrm{b}}$, due to the sharp interfaces produced by target engineering, there will be range of circumstances in which resistivity gradients are capable of producing powerful confining magnetic fields.

[10] This is Davies' qualitative interpretation of this equation [53].

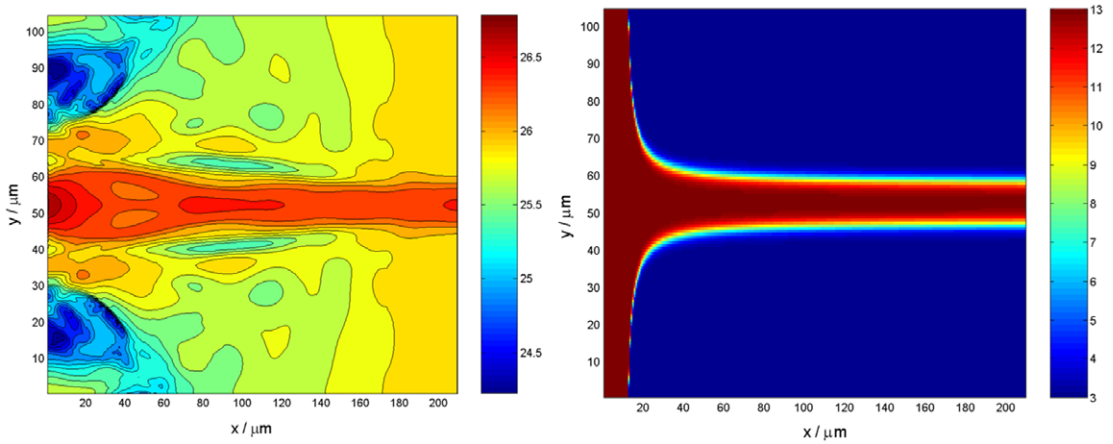

Figure 18. (Left) Plot of fast electron density (m^{-3}, $\log_{10}$) after 750 fs, and (right) plot of target Z in an early simulation carried out using the 2D hybrid-VFP code, LEDA. The injected FEB models laser irradiation at 1 μm, with a laser intensity of 5×10^{19} W cm^{-2}, 30% absorbed into fast electrons, and a $\cos^4\theta$ angular distribution for the injected fast electrons. The target is at solid density.

6.4. Preliminary studies of resistive guiding

In the work of Robinson and Sherlock [168] this concept was explored using a 'hybrid-VFP' code and very good guiding was demonstrated. This investigation concentrated on the conditions close to those of laboratory experiments involving solid-density foils and PW class lasers that deliver a few hundred Joules in about a picosecond. The possibility that 'cold target' effects might cause a problem for the concept was also investigated and it was shown that a small temperature range over which the resisitivities are inverted can be tolerated. One might expect that once collimation has occurred, that the $\eta\nabla\times\boldsymbol{j}_{\rm f}$ will then act to reinforce this collimation and sustain it, even if the $\nabla\eta\times\boldsymbol{j}_{\rm f}$ greatly diminishes. Robinson and Sherlock showed some evidence for this sort of positive feedback in this concept. These initial simulations were done in 2D Cartesian coordinates, and only considered a guiding structure that was perfectly aligned with the axis along which the fast electrons were injected. In figure 18 results from one of these early simulations are shown, including the material composition of the target and the fast electron density after several hundred fs.

Some promising results were obtained in early experiments carried out using PW class lasers and 'cold' solid-density targets [109, 160], and more simulation work was carried out using a 3D particle hybrid code to help interpret these experiments. This combination of numerical studies and experiments gives one good reason to believe that resistive guiding is a genuinely realizable effect that *might* be exploited in FI. Subsequent work in this area has therefore focussed on two major concerns: (i) Can resistive guiding work under the conditions that FI imposes on it? and (ii) How precisely can we exploit resistive guiding in a realistic FI scenario?

6.5. Resistive guiding at high-energy scales

Applicability of the fast-electron collimation scheme exploiting resistivity gradients to FI depends on two factors: (i) the collimating magnetic fields need to persist during the entire ignition pulse; (ii) the high-resistivity path must survive the compression resulting from the implosion. In an ignition pulse, the material along the path of electron propagation is heated to keV temperatures. At such high temperatures, the resistivity of such a material can become less than the resistivity of the surrounding plasma and the resistivity gradients can be inverted. The question is whether or not the inverted resistivity gradients can cause a magnetic field reversal from collimating to de-collimating. It can also be difficult to maintain the guiding structure extending to the dense fuel up to the time of significant compression of the FI target. This problem should be addressed either by developing target designs for which the damaging effect of the implosion is minimized or placing the guiding structure inside a protective cone as was suggested in [167].

Collimation of high-energy electron beams in the wire-like structures has been studied [188]. Simulations using the hybrid-PIC code LSP were performed for a 40 μm diameter copper wire embedded in aluminum. A 10 ps (constant in time), 2 MeV mean-energy, relativistic-Maxwellian electron beam with divergence half-angle of 67°, and total energy of 20 kJ was injected into the wire. The beam was found to be effectively collimated for the whole duration of the electron pulse. About 65% of the injected electrons were collimated on the length of the collimating structure of 150 μm. The resistivity gradient at the wire boundary was found to be inverted because of the wire heating by fast electrons in less than 0.5 ps after the beginning of the electron pulse. The collimating magnetic field, however, persisted because the magnetic field had two components: one generated by the resistivity gradients and the other by the return current gradients. Initially, the collimating magnetic field was generated by the resistivity gradients. The resulting collimation caused large current density gradients that enhanced the collimating field. The current density gradient offset the effect of the reversal of the resistivity gradient thus supporting a large saturated collimating magnetic field. Similar conclusions were obtained for lower-energy electron beams in [160].

LSP simulations [188, 191] showed that high-energy electron beams can be guided by a mid-Z wire through the cone tip and coronal plasma of a FI target, subject to survivability of the wire during the implosion. The simulations utilized idealized cone-fuel configurations with

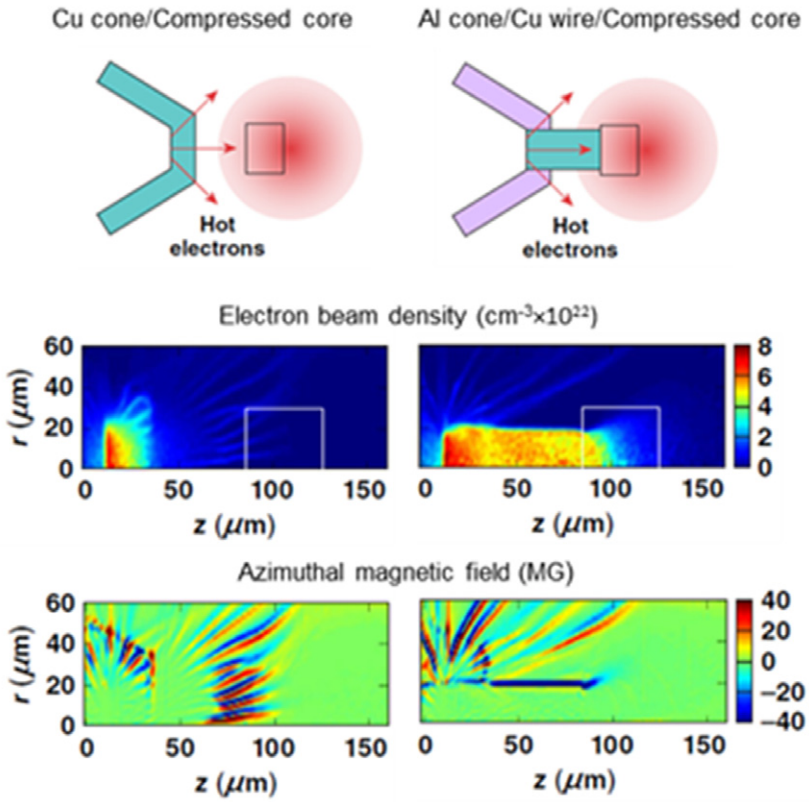

Figure 19. LSP simulations [188] predicting significant increase in energy coupling to the compressed core by the self-generated magnetic field at the copper wire interface.

and without a wire (figure 19). A 75 μm long, 40 μm diameter copper wire goes through the 25 μm thick tip of aluminum cone towards the precompressed deuterium fuel core. The core has a super-Gaussian density distribution $400\exp(-(r/50)^4)$ g cm^{-3} where r is the distance from the centre in μm, sited on a background deuterium plasma of 10 g cm^{-3}. The initial temperature of 100 eV was assumed, ionization and radiative cooling were modelled for copper and aluminum. The simulations used a 40 kJ, 10 ps, 1.6 MeV-mean-energy relativistic-Maxwellian electron beam with initial divergence half-angle of $67^\circ(\propto\exp(-(\theta/\theta_0)^2)$, with $\theta_0 = 67^\circ$), constant temporal profile, and a super-Gaussian radial profile $\exp(-(r_\perp/20)^4)$, where $r_\perp$ is the distance from the beam axis in μm, injected at the inner side of the cone tip. Comparison simulations were performed in which the cone and the wire were replaced by a single copper cone. Fast-electron energy deposition in the cylindrical region (see figure 19) with a diameter of 60 μm and a length of 40 μm (so-called 'ignition region') was calculated. The simulations confirm that the fast-electron coupling to the core is significantly improved with the wire: 45% coupling efficiency to the 'ignition region' in the cone-wire case versus 7% without a wire. It can be seen in figure 19 that fast electrons are effectively collimated and guided by the self-generated resistive magnetic fields at the interface of the copper wire and surrounding lower-Z plasma. Collimation of electrons to the dense fuel in a wire-like structure has been also confirmed by hybrid simulations of J. Honrubia and D. Larson using codes PETRA and ZUMA [191]. Notice for completeness that the divergent electron flow outside the wire in figure 19 is subject to resistive filamentation instability. Resistive filamentation generally requires three-dimensional simulations, while in these cylindrically symmetric simulations only radial modulation of the electron beam develops.

The question of wire survivability was not addressed but it was noted that it may be difficult to maintain a clean high-resistivity path to the dense core at the time of peak compression in an imploded capsule. Detailed target design studies using radiation-hydrodynamics codes are required to show if such a divergence-mitigating structure can be assembled in an actual implosion.

6.6. Advanced uses of resistive guiding

The use of resistive guiding in FI may not necessarily be restricted to the cone-wire scheme discussed above. Other schemes have been suggested that do not require placing an element outside of the cone. Instead, such schemes suggest putting guiding structures in an insert in the cone tip. This may have the advantage of being more robust with respect to the hydrodynamics of fuel assembly, although detailed radiation-hydrodynamics studies are required to confirm this.

One, suggested by Schmitz [175], is to use a curved axisymmetric interface (ellipsoidal or paraboloidal) to produce an azimuthal magnetic field structure that acts as a curved mirror. A divergent fast electron spray will then have its angular spread reduced by the approximately specular deflection in the strong magnetic field which is localized at this interface, in a way that is analogous to a parabolic or elliptical mirror in ray optics. This comes at the expense (as in the case

of an optical parabolic mirror) of increasing the radial extent of the beam. As the hot-spot radius and laser spot radius are likely to be comparable in size, there will be limits on how much the radial extent of the beam can be increased to reduce angular spread (the diameter of the cone apex may also have to be limited for fuel assembly). This was not assessed in Schmitz's original proposal due to limitations on the size of the simulation domain. Some preliminary simulation results presented by Robinson suggest that some substantial benefits might still be obtained from the elliptical mirror approach [169] where a simple elliptical configuration yielded about an improvement in coupling into a target hot-spot region of about 2–3× (over an unguided case).

Another suggestion was made by Robinson *et al* [167] who suggested a 'magnetic switchyard' configuration: a series of concentric quasi-cylindrical guide shells immersed in a less resistive substrate. Strong azimuthal fields grow at the interfaces, confining fast electrons into the guide shells. Each guide shell will receive a portion of the fast electron population with limited angular spread about some mean angle. The guide shells then curve around in an arc which re-directs this mean angle to some distant region. As with the aforementioned mirror concept, this means that the switchyard must increase its radial extent beyond that of the source radius. The numerical simulations presented by Robinson showed that, at least for some configurations, an improvement in coupling of about 2–3× (also compared to an unguided case).

To the same goal, Debayle *et al* [56] recently proposed a structured target made of narrow high- and low-Z elements of density decreasing in the axial direction. The magnetic modulations developing at the filament interfaces then decay away from the surface, leading to non-specular reflections of the fast electrons trapped inside the high-Z filaments. As a result, their local angular dispersion steadily decreases along their path. The capability of these targets to both guide the fast electrons and reduce their angular dispersion is, however, obtained at the cost of heavy constraints on target manufacturing.

Finally, note that transverse resistivity gradients associated to density or temperature non-uniformities in the corona also have the potential to beneficially affect the FET. This was demonstrated both experimentally and numerically in [151] in the case of cylindrically-compressed foam targets. Insofar as they are injected shortly before the shock convergence, the fast electrons can be efficiently guided by the magnetic field growing at the shock front. On the other hand, non-uniformities can help drive resistive filamentation [165], as well as the decollimating effects noted in section 5, so the exploitation of hydrodynamically induced non-uniformities requires careful examination.

6.7. Double pulse approach

The double pulse approach [166] to fast electron divergence control employs, as the name implies, two laser pulses. The role of the first laser pulse is to pre-generate an azimuthal magnetic field using a small fraction of the total laser energy, whereas the role of the second laser pulse is to deliver the majority of the fast electron energy. This concept was motivated by the empirical observation that FEBs appeared to be more collimated at lower intensities [82], from which it was inferred that the intrinsic divergence of the FEB (at injection) was lower at lower intensities ($<10^{20}$ W cm^{-2}).

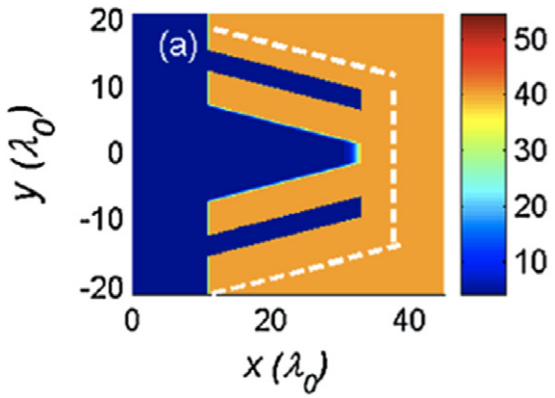

Figure 20. The double-cone target employed in simulations by Cai *et al* [36] (reprinted with permission © 2009 The American Physical Society).

Once the assumption that the divergence angle of the FEB generated at a lower intensity is substantially lower is made, the collimation of this 'generator' FEB occurs fairly easily: in equation (9) there is strong dependence on the divergence angle, but also weak dependence on power and fast electron temperature which increase the likelihood of collimation at lower intensity. The magnetic field can easily reach flux densities at which it will strongly guide a FEB with ignition-scale parameters in moderate Z materials.

Preliminary experimental results obtained by Scott [162] indicate that this approach may be possible. However this experiment was based on illuminating Al foils with sub-kJ 1-ps laser pulses, so the extent to which this shows viability at igntion scale is rather limited. Further experimental and theoretical studies are needed to see if the double pulse approach is truly a viable option for full-scale FI.

6.8. Double cone approach

In this concept, a vacuum gap is introduced in order to prevent those fast electrons travelling at large angles from escaping. The vacuum gap is introduced by employing a target using two concentric cones rather than one, hence 'Double Cone'. Due to the vacuum gap, the cone wall is isolated from the coronal plasma and the fast electrons are confined and guided to the tip by electrostatic and quasistatic magnetic fields formed in the vacuum gap region.

The fast electron guiding using vacuum gap has been first proposed by Campbell *et al* [39], where a collimation of high-energy electrons using planar plug/gap/foil structure was numerically shown and an idea to control fast electron using a conical plug/gap/foil structure (see [39]) was proposed for FI application. This scheme can be applied for the beam guiding from cone tip to the core. Nakamura *et al* [142] have suggested a double-cone target (figure 20), where the vacuum gap is introduced into the side wall of cone target. On the basis of two-dimensional (2D) PIC simulation, they showed that the double-cone confines the electrons for hundred of femtoseconds (fs) by the sheath electric field generated inside the vacuum-gap. However, the simulation time was limited to

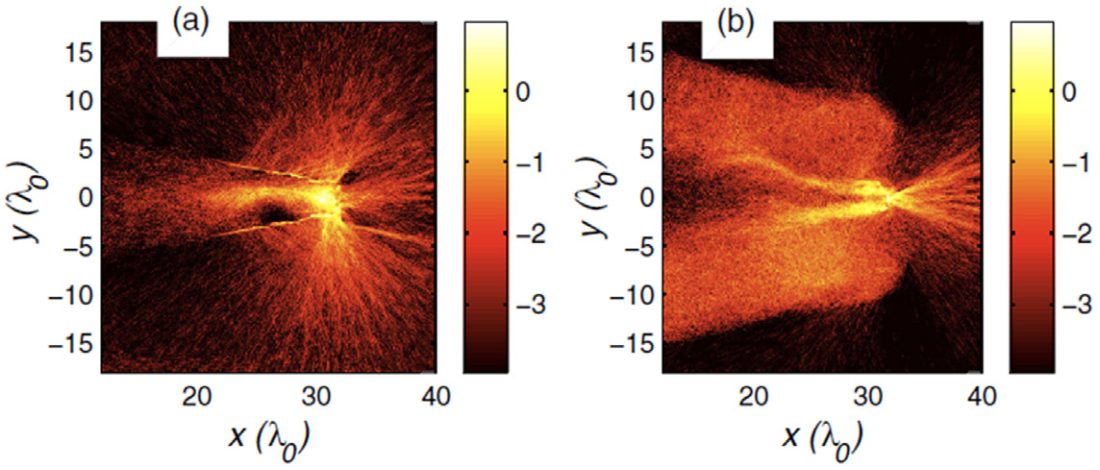

Figure 21. Natural logarithm of electron energy density for (*a*) single cone and (*b*) double cone at 1 ps in simulations performed in [36] (reprinted with permission © 2009 The American Physical Society).

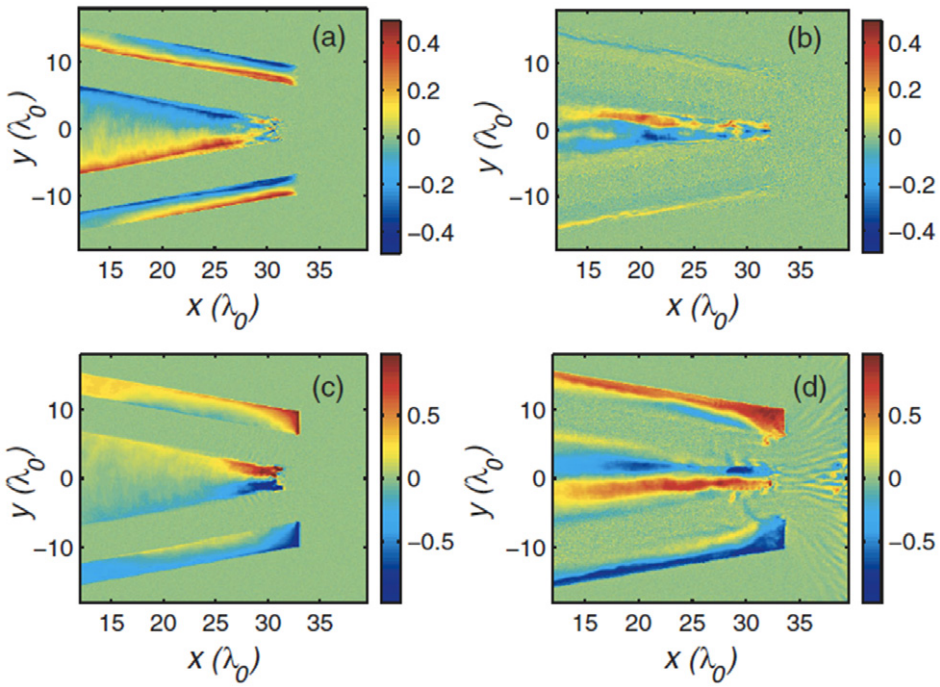

Figure 22. PIC Simulations results from [36] (reprinted with permission © 2009 The American Physical Society) showing: (*a*), (*b*) time-averaged sheath electric fields at 330 and 1500 fs and (*c*), (*d*) time-averaged magnetic fields at 330 and 1500 fs. Fields are in normalized units, i.e. $m_e\omega_0 c/e$.

a few hundred fs. Contrary to this, the core heating duration in practice is 10 ps order. So the reduction of sheath electric field inside the gap due to the plasma expansion from the cone wall in the early phase of core heating and then the failure of confinement was feared. Later, Cai *et al* [36], carried out ps order 2D PIC simulations and demonstrated that the double cone is still effective in confining the high-energy electrons even for the gap width of a few micrometres (figure 21).

After reduction of sheath electric field due to plasma expansion, the quasi-static magnetic field works to confine the fast electrons (figure 22). The quasistatic magnetic field has been generated due to a localized supply of high-energy electrons, originally produced at the inner-cone and the cone tip. This electron current coming from the cone tip produces a positive current inside the gap, while an opposite-directional surface-current is generated along the inner-surface of the outer-cone. The collaboration of these two currents generate a large quasistatic magnetic field inside the gap. These quasistatic fields continue to confine the high-energy electrons for longer than a few picoseconds. They showed that the double cone can reduce the beam energy loss from the side wall down to 1/3 of that for the single cone case.

Even if the double cone is used, the FEB after penetrating the cone tip spatially diverges during propagation to the core due to its large divergence angle and then the enhancement of core heating rate may not be expected so much. In order to guide the FEB close to the core, Johzaki, *et al* [104] have proposed to extend the cone tip and vacuum gap

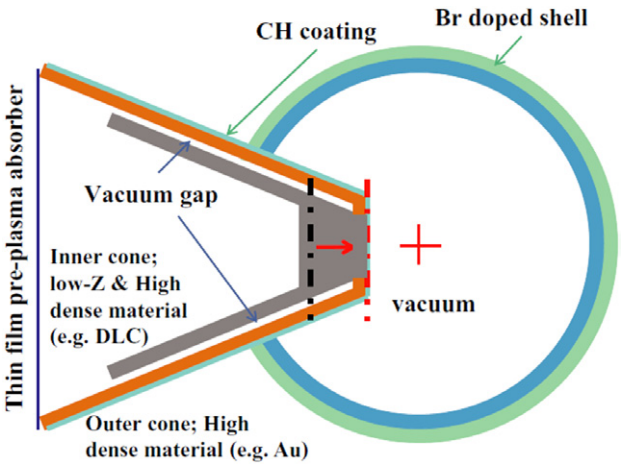

Figure 23. Schematic view of the extended double cone proposed in [104] (reprinted with permission © 2009 IOP Publishing).

(figure 23). They called it the 'extended double cone', which is a combination of the conical plug/gap/foil structure [39] and the double cone [36, 142]. In this case, the fast electrons travel a long distance in the extended tip region, so that low-Z, but relatively dense material (e.g. DLC) was proposed as the tip material to reduce the collisional effects [102, 103]. It was shown from the 2D PIC and FP simulations for core heating that the extended double cone with a short inner wall enhances the core heating rate more than four times when compared with the single wall cone case (see figure 23 and table 1).

The preliminary experiments have been conducted by Sakawa *et al* [173] to prove the vacuum-shielding effect using an Al–Cu double-foil targets with and without a vacuum gap. The enhancement of the number of electrons detected in the target surface direction has been observed for the case with the vacuum gap compared to the case without vacuum gap, which demonstrates the fast electron confinement by the vacuum gap.

For more realistic evaluations of the possibilities for the extended double cone, hydrodynamic modelling of the cone's ignition-time structural distortion must be included in the simulations. Also, the integrated experiments are indispensable to prove the guiding performance.

6.9. Axial magnetic field approach

There is another approach to divergence mitigation which employs an imposed magnetic field, rather than a field self-generated by the fast electron current. There are two main methods which have been suggested for imposing the needed multi-MG fields: flux compression in the fuel assembly implosion [178, 200], and laser-driven coils [47, 78, 79]. A body of simulation work has been carried out at LLNL on the assembly of such fields, and the characterization of their advantages for electron transport, which we shall review here.

The purpose of an imposed field is to spatially confine the fast electrons to small radius (perpendicular to the axial direction), and enhance their flux on the fuel. We distinguish confinement, or limiting the fast electrons from spreading in space, from collimation, or reducing their velocity-space divergence. A confining magnetic field generally will not collimate, so fast electrons emerge from a confining magnetic field with their original divergence. An estimate of the product of field strength times path length needed to confine a fast electron of velocity v is given by [168]

$$BL > K\gamma\beta(1-\cos\theta) \qquad K \equiv \frac{m_e c}{e} = 17.0\ \mathrm{MG}\,\mu\mathrm{m}. \tag{98}$$

$\beta = |v|/c$, $\gamma = (1-\beta^2)^{-1/2}$, and θ is the angle between v and the z-axis. For instance, a 3 MeV electron with $\theta = 45^\circ$ requires $BL > 33.9\,\mathrm{MG}\,\mu\mathrm{m}$ to be confined. Keeping the field thickness smaller than the source spot size imposes $L \leqslant 10\,\mu$m, or $B \geqslant 3$ MG.

Flux compression [213] exploits the frozen-in law of MHD, which states that the magnetic flux $\propto \boldsymbol{B}\cdot\mathrm{d}\boldsymbol{a}$ enclosed by a good conductor of area a remains constant. As a decreases the field strength rises. A 'good' conductor is one for which the resistive diffusion time $\sim\mu_0\sigma L^2$ of the magnetic field is much longer than the implosion time (σ is the conductivity and L a field length scale). Implosions at the Omega laser have compressed axial seed fields of $\leqslant$0.1 MG to 20–40 MG in cylindrical [115] and spherical [41, 91] geometry.

Preliminary FI implosion simulations with an initial seed magnetic field have been performed, using the MHD capabilities of Hydra [178] and Lasnex [200]. These have considered radiation-driven implosions around a re-entrant cone. Figure 24 shows the magnetic field in a Hydra simulation done by Shay, starting with a uniform, axial field of 0.1 MG. It is similar to the implosions presented in [178], and entails a radiation-driven beryllium ablator, a DT ice layer, and a carbon-tipped gold cone. The plot is taken at the time of peak fuel compression, and shows a field of 500 MG in the compressed fuel. However, the field does not diffuse far into the cone or its interior, where the field in the critical-density plasma is $\leqslant$20 MG. The fast electrons will therefore be generated by short-pulse LPI in a region of relatively low field. This poses two challenges. First, electrons which encounter a field that increases along field lines (e.g., an axial field that increases in the axial direction) are subject to magnetic mirroring and reflection. In addition, there is a stand-off distance before the fast electrons reach a field strong enough to confine them.

Imposed multi-MG axial fields have been studied using the coupled hybrid-PIC code Zuma and the rad-hydro code Hydra in [196] (see section 5, for previous description). This work considered an idealized, spherical DT fuel assembly with a carbon cone, and simple initial field profiles. Fusion yields are presented in figure 25. The electron source had a substantial divergence based on full-PIC LPI simulations: $\mathrm{d}N/\mathrm{d}\Omega \propto \exp[-(\theta/\Delta\theta)^4]$ with $\Delta\theta = 90^\circ$, giving $\langle\theta\rangle = 52^\circ$; Ω is the velocity-space solid angle element. A 50 MG uniform, initial axial field performed slightly better than an artificially collimated source with $\Delta\theta = 10^\circ$ (or $\langle\theta\rangle = 7^\circ$) with no imposed field. Both cases required $\sim$130 kJ of fast electrons to ignite. A field of 30 MG needed almost twice as much energy to ignite, while a 10 MG field performed significantly worse (although still much better than with no initial field). This work explored the degradation due to mirroring in non-uniform field profiles, and presented the hollow magnetic pipe as one way to avoid mirroring. The effects on yield are presented in figure 25. The non-uniform field cases labelled BZ30-75, BZ50-75 and BZ0-50 demonstrate the reduced coupling due to mirroring.

Table 1. Summary of heating results from extended double cone (EDC) calculations [104].

Cone type	Pre-plasma	$\eta_{L\to fe}(\%)$	$\eta_{L\to fe<10\,MeV}(\%)$	$\eta_{fe\to core}(\%)$	$\eta_{L\to core}(\%)$	$\langle T_i\rangle_{DD}$ (keV)
Single cone	None	18 (48)	15 (39)	16	7.5	0.75
Single cone	$\lambda_p = 10\,\mu m$	14 (36)	4 (11)	4.7	1.7	0.35
Ex. Dbl. cone	None	31	27	62	19	1.27
Ex. Dbl. cone	$\lambda_p = 10\,\mu m$	20	11	28	5.5	0.7
EDC with short inner wall	None	41	35	79	32	1.58
EDC with short inner wall	$\lambda_p = 10\,\mu m$	23	14	36	8.1	1.01

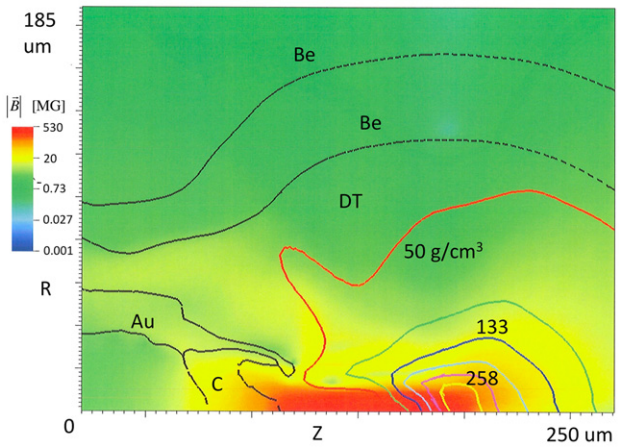

Figure 24. Magnetic field from a Hydra simulation with an initial axial field of 0.1 MG, performed by Shay and detailed in the text. The solid or dashed black contours are material interfaces, the coloured contours are density (the red, bark blue and yellow values are indicated), and the solid background colour is $|\boldsymbol{B}|$ on a log scale. Text labels indicate material.

The magnetic pipe, case BZ50-pipe, couples almost as well as the uniform field case BZ50. Figure 26 shows the pipe field envelope; the thick pipe (solid black outline) is used in figure 25. More work on assembling pipe field structures in FI implosions is needed to make this scheme viable.

The role of different terms in Ohm's law has been studied in several recent works, such as [102, 143, 196] (models based on Ohm's law are detailed in section 4.2 of the present review). All of them have shown that the fast electron coupling to a spherical fuel region is degraded with an extensive Ohm's law that includes terms beyond the resistive $\eta \boldsymbol{J}_e$, especially ∇p_e. This produces an azimuthal $\nabla n_e \times \nabla T_e$ magnetic field at the fuel interface that pushes fast electrons to large radius and away from the hot spot.

Imposed magnetic pipes of differing orientation illustrate the potential benefits of axial (B_z) and azimuthal (B_ϕ) fields. Both the field direction (z versus ϕ) and sign significantly affect its confinement properties, as do non-resistive terms in Ohm's law. Electrons are confined in radius by the radial component of the $\boldsymbol{v} \times \boldsymbol{B}$ Lorentz force, which is independent of v_r and B_r. For a simplified discussion we neglect the change in v_r and v_ϕ due to free motion. This is valid for sufficiently small Larmor radius. The expected confinement based on electron orbits is as follows. Each sign of B_z should confine electrons with one sign of v_ϕ to a small radial excursion, and the other sign of v_ϕ to a larger one. Since the electron source is expected to be uniform in v_ϕ, we expect comparable confinement from either sign of B_z. For $B_\phi < 0$, however, both signs of v_ϕ are well confined, while both are poorly confined for $B_\phi > 0$. We therefore expect $B_\phi < 0$ to confine the best, $B_\phi > 0$ to confine the worst, and both signs of B_z to be intermediate and comparable to each other.

Zuma–Hydra simulations with the same profile of initial $|\boldsymbol{B}|$ have been performed for four cases all with peak magnitudes of 50 MG: $B_z > 0$, $B_z < 0$, $B_\phi > 0$, and $B_\phi < 0$. For the B_z cases the magnetic field is found from a vector potential A_ϕ, so that B_r is included to satisfy $\nabla \cdot \boldsymbol{B} = 0$; no such B_z or B_r is needed for $B_\phi(r, z)$. These calculations show a different ordering of confinement quality than the simple orbit discussion. Figure 26 plots the fusion yield for various initial fields. As expected from orbits, $B_\phi < 0$ performs the best, and $B_\phi > 0$ the worst. Although both B_z have intermediate performance, $B_z < 0$ confines better than $B_z > 0$. The results presented in [196] unfortunately used $B_z > 0$, and would be better with the opposite choice. Moreover, the better confinement with an imposed B_ϕ is promising for self-generated field approaches, which usually give rise to a B_ϕ.

Simplified Zuma-only runs (no coupling to Hydra) were performed to study magnetic pipes of different field orientation. They indicate that the different coupling for the two signs of B_z results from different magnetic field evolution, which occurs only when non-resistive terms are included in Ohm's law. These runs used a uniform DT plasma of $\rho = 10\,g\,cm^{-3}$ and 100 eV, and a divergent electron source with $\Delta\theta = 90°$. Figure 27 depicts the power of fast electrons reaching the right edge, inside the pipe radius, and counting only 1.3 MeV of kinetic energy per electron (the maximum deposited in a DT hot spot of optimal depth $\rho\Delta z = 1.2\,g\,cm^{-3}$). For both the left panel ($\boldsymbol{E} = 0$, $\boldsymbol{B}$ = constant) and centre panel ($\boldsymbol{E} = \eta \boldsymbol{J}_e$, $\boldsymbol{B}$ evolves), the ordering is as expected from orbits. However, when a more extensive Ohm's law is used, the two signs of B_z perform differently, with $B_z < 0$ coupling better than $B_z > 0$. Work is ongoing to elucidate the difference in field dynamics.

Magnetic field generation by laser-driven coils [47] was demonstrated experimentally in the 1980s, and has recently been suggested as a divergence mitigation approach for FI [79]. In this scheme, a coil connects two plates, one of which is struck by a kJ-class, long pulse (~ns) laser. This generates hot (~10 keV) electrons by resonance absorption, which reach the other plate and set up a potential difference between the two plates. A large, transient current flows through the coil and induces a large magnetic field. Experiments at GEKKO-XII [79] have recently made fields of 10 MG. Reference [46] reports smaller-scale experiments at the VULCAN laser which generated fields of 0.1 MG, as well as a simple model of the system. This approach eliminates the need to create large fields in an implosion, and allows one to consider novel field

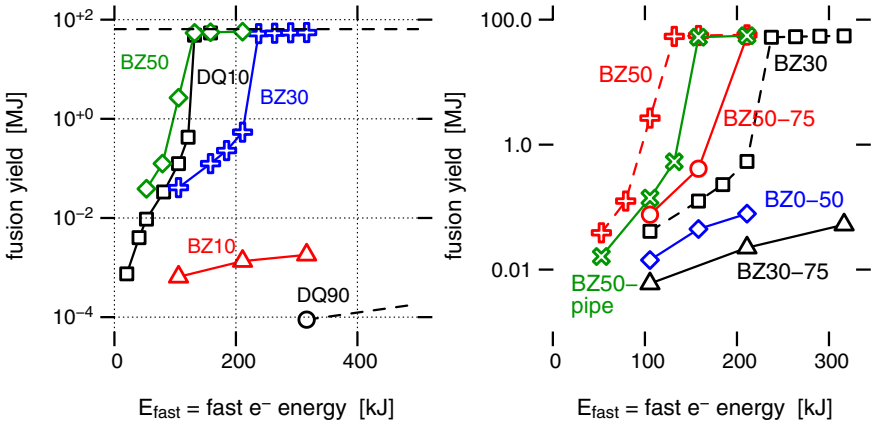

Figure 25. Reprinted with permission from [196] © 2012 American Institute of Physics: fusion yield versus added fast electron energy for Zuma–Hydra runs with PIC-based divergence $\Delta\theta = 90^\circ$, except for one with an artificially collimated source $\Delta\theta = 10^\circ$ and no initial B field (labelled DQ10). Other cases had no initial B_z (DQ90), initial uniform $B_z = 10$, 30, 50 MG (BZ10, BZ30, BZ50), non-uniform initial B_z rising gradually from 30 to 75 MG (BZ30-75), gradually from 50 to 75 MG (BZ50-75), rapidly from 0.1 to 50 MG (BZ0-50), and the magnetic pipe with 50 MG peak field (BZ50-pipe).

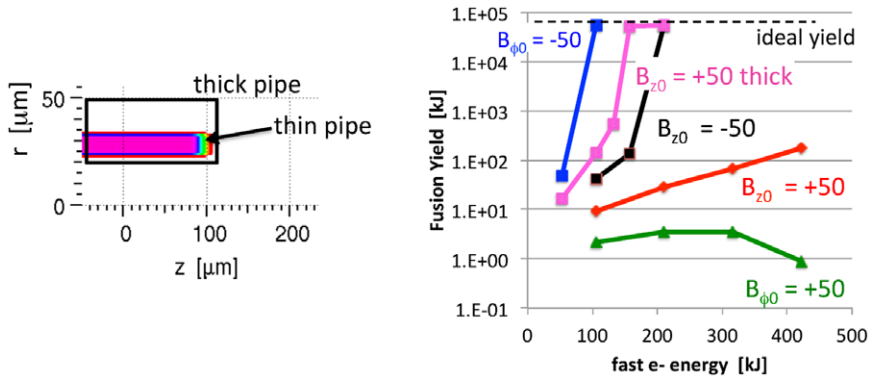

Figure 26. Left: initial magnetic field envelope $|B_z|$ or $|B_\phi|$ for integrated Zuma–Hydra runs with thick and thin 'pipe'. Right: fusion yield versus injected fast electron energy for thick pipe with $B_{z0} > 0$ (taken from [196]) and thin pipes with different B_0 signs and directions.

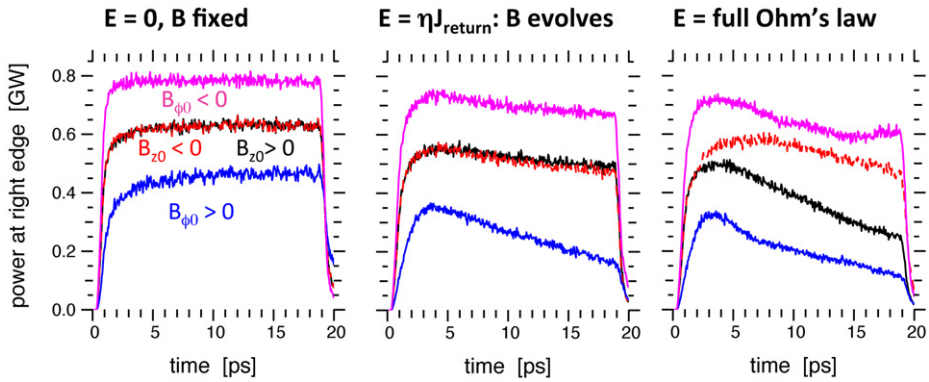

Figure 27. Fast electron power reaching right edge in simplified Zuma-only simulations with initial, 'thin' magnetic pipes as in figure 26.

configurations. For instance, the field could peak on the short-pulse laser side of the re-entrant cone, so that the mirroring effect pushes fast electrons *towards* the fuel. The field is generated over a few ns, which is only a fraction of the duration of a typical FI implosion. It can therefore be timed such that the implosion modifies the field in a limited way. Realistic rad-hydro-MHD modelling is needed to validate the laser-driven coil approach in specific geometries, and when coupled to specific implosions.

7. Conclusions

Although fast ignition ICF was proposed nearly 19 years ago, in-depth simulation studies of the fast electron transport aspect of the problem have only really been done over the past 7 years or so (section 5). In this review we have looked at the following aspects:

(i) *Basic physics*. The fundamental physics of fast electron transport is thought to be well understood. Where doubts

do exist is in the ability to calculate the properties of dense matter, and collisional processes to very high accuracy. Another aspect which has not been fully explored is the extent to which kinetic micro-instabilities affect transport, and whether significant corrections could be included in hybrid models. These aspects need to be addressed, but it is thought that these are unlikely to radically alter the outlook for fast ignition.

(ii) *Simulation methods*. In section 4 it was shown that there are now a number of different simulation models and a large number of codes. These are nearly all extendable models that can include a wide variety of physics, and most have some 'hybrid' character. There are a number of codes that include hydrodynamic motion, radiation transport, and thermonuclear burn—representing a true merging of the hybrid model with standard ICF rad-hydro models. Thus there are codes that can tackle most of the full problem. This is subject to the inclusion of a realistic fast electron source and the approximations inherent in 'hybridization'. Nonetheless, as this review shows, this is sufficient to use computer simulation to make a first assessment of the viability of the fast ignition concept.

(iii) *Ignition-scale calculations*. In recent years there have been a number of studies (see section 5) which have attempted to use the aforementioned numerical models to assess the viability of fast ignition at (or close to) ignition scale. This has ranged from rather idealized calculations through to calculations which have attempted a good degree of realism. These calculations have shown that achieving modest or 'attractive' ignition energies ($<$100 kJ of laser energy) is difficult. The good laser-to-fast electron conversion efficiencies that are seen in certain PIC calculations (40–50%) are certainly beneficial, but the degradation of the coupling into the hot spot due to high fast electron divergence is considerable.

(iv) *Controlling transport*. As the divergence problem is a serious one, a number of studies have looked at modifications to the FI scheme that will allow the flow of fast electrons to be sufficiently controlled as to improve the coupling into the hot spot. In section 6 a number of interesting possibilities were discussed including the exploitation of resistivity gradients, axial magnetic fields, and double cones. This is a highly active area, which may eventually produce an attractive solution to the divergence problem.

The problem of simulating fast electron transport in fast igntion is not a trivial problem. Nonetheless, as this review shows, there has been considerable progress over the last seven years or so. The main challenge that is now being faced is how one can modify transport so that relatively modest ignition energies can be achieved given a divergent fast electron source. A number of concepts have been proposed, and thus it is still entirely possible that an attractive fast ignition point design will emerge in the coming years.

Acknowledgments

APLR and DJS (Lead Coordinators of this paper) would like to thank all the contributors for their effort, dedication, and patience. APLR and DJS also acknowledge their particular contributions: J.R. Davies—Drag and Scattering, section 3.3; L. Gremillet—beam-plasma instabilities, section 3.4; M. Sherlock—VFP codes, section 4.1; A.A. Solodov—Hybrid PIC codes, section 4.3 and Resistive guiding at high-energy scales, section 6.5; J. Honrubia—Review of ignition-scale calculations, section 5; T. Johzaki—double cone approach, section 6.8; DJS—background plasma physics, section 3.5 and axial magnetic field approach, section 6.9. Remaining text prepared by APLR with help from RJK. We acknowledge the many contributions to this field by our late colleague, M.G. Haines.

References

[1] Achterberg A., Wiersma J. and Norman C.A. 2007 The Weibel instability in relativistic plasmas: II. Nonlinear theory and stabilization mechanism *Astronom. Astrophys.* **475** 19–36

[2] Adam J.C., Héron A. and Laval G. 2006 Dispersion and transport of energetic particles created during the interaction of intense laser pulses with overdense plasmas *Phys. Rev. Lett.* **97** 205006

[3] Antia H.M. 1993 Rational function approximations for Fermi–Dirac integrals *Astrophys. J.* **84** 101

[4] Atzeni S, Schiavi A and Bellei C 2007 Targets for direct-drive fast ignition at total laser energy of 200–400 kJ *Phys. Plasmas* **14** 052702

[5] Atzeni S 1999 Inertial fusion fast ignitor: igniting pulse parameter window vs the penetration depth of the heating particles and the density of the precompressed fuel *Phys. Plasmas* **6** 3316–26

[6] Atzeni S., Schiavi A. and Davies J.R. 2009 Stopping and scattering of relativistic electron beams in dense plasmas and requirements for fast ignition *Plasma Phys. Control. Fusion* **51** 015016

[7] Atzeni S., Schiavi A., Honrubia J.J., Ribeyre X., Schurtz G., Nicolaï P., Olazabal-Loumé M., Bellei C., Evans R.G. and Davies J.R. 2008 Fast ignitor target studies for the HiPER project *Phys. Plasmas* **15** 056311

[8] Baalrud S.D. 2012 Transport coefficients in strongly coupled plasmas *Phys. Plasmas* **19** 030701

[9] Baiko D.A., Kaminker A.D., Potekhin A.Y. and Yakovlev D.G. 1998 Ion structure factors and electron transport in dense coulomb plasmas *Phys. Rev. Lett.* **81** 5556–9

[10] Baton S.D. *et al* 2008 Inhibition of fast electron energy deposition due to preplasma filling of cone-attached targets *Phys. Plasmas* **15** 042706

[11] Beg F.N., Bell A.R., Dangor A.E., Danson C.N., Fews A.P., Glinsky M.E., Hammel B.A., Lee P., Norreys P.A. and Tatarakis M. 1997 A study of picosecond laser–solid interactions up to 10^{19} W cm^{-2} *Phys. Plasmas* **4** 447–57

[12] Bellei C., Divol L., Kemp A.J., Key M.H., Larson D.J., Strozzi D.J., Marinak M.M., Tabak M. and Patel P.K. 2013 Fast ignition: dependence of the ignition energy on source and target parameters for particle-in-cell-modelled energy and angular distributions of the fast electrons *Phys. Plasmas* **20** 052704

[13] Bell A.R. and Kingham R.J. 2003 Resistive collimation of electron beams in laser-produced plasmas *Phys. Rev. Lett.* **91** 035003

[14] Bell A.R. *et al* 1997 Fast electron transport in high intensity short-pulse laser-solid experiments *Plasma Phys. Control. Fusion* **39** 653–9

[15] Bell A.R., Robinson A.P.L., Sherlock M., Kingham R.J. and Rozmus W. 2006 Fast electron transport in laser produced plasmas and the KALOS code for solution of the Vlasov

Fokker Planck equation *Plasma Phys. Control. Fusion* **48** R37
[16] Bendib A. 1993 Dielectric functions for the Vlasov–Landau equation *Phys. Rev.* E **47** 3598–606
[17] Berger M.J., Coursey J.S., Zucker M.A. and Chang J. 2005 *Estar, Pstar, and astar: Computer Programs for Calculating Stopping-Power and Range Tables for Electrons, Protons, and Helium Ions* (Gaithersburg, MD: National Institute of Standards and Technology) http://physics.nist.gov/Star
[18] Bhatnagar P.L., Gross E.P. and Krook M. 1954 A model for collision processes in gases: I. Small amplitude processes in charged and neutral one-component systems *Phys. Rev.* **94** 511–25
[19] Birdsall C.K. and Langdon A.B. 2005 *Plasma Physics via Computer Simulation* (New York: Taylor and Francis)
[20] Bludman S.A., Watson K.M. and Rosenbluth M.N. 1960 *Phys. Fluids* **3** 747
[21] Bohm D and Pines D 1953 A collective description of electron interactions: III. Coulomb interactions in a degenerate electron gas *Phys. Rev.* **92** 609–25
[22] Bohm D. and Gross E.P. 1949 Theory of plasma oscillations. A. Origin of medium-like behavior *Phys. Rev.* **75** 1851–64
[23] Boyd T.J.M. and Sanderson J.J. 1967 *Plasma Dynamics* (London: Nelson and Sons)
[24] Brackbill J.U. and Forslund D.W. 1982 An implicit method for electromagnetic plasma simulation in two dimensions *J. Comput. Phys.* **46** 271–308
[25] Braginskii S.I. 1965 Transport properties in a plasma *Reviews of Plasma Physics* vol 1 ed M.A. Leontovish (New York: Consultants Bureau) pp 205–311
[26] Brantov A.V., Bychenkov V.Yu., Rozmus W. and Capjack C.E. 2006 Dielectric function and electron transport in collisional plasma *IEEE Trans. Plasma Sci.* **34** 738–54
[27] Bret A. and Deutsch C. 2008 Correlated stopping power of a chain of N charges *J. Plasma Phys.* **74** 595–9
[28] Bret A., Dieckmann M. and Deutsch C. 2006 *Phys. Plasmas* **13** 082109
[29] Bret A., Firpo M.C. and Deutsch C. 2004 Collective electromagnetic modes for beam–plasma interaction in whole *k*-space *Phys. Rev.* E **70** 046401
[30] Bret A., Firpo M.C. and Deutsch C. 2005 Electromagnetic instabilities for relativistic beam–plasma interaction in whole *k* space: nonrelativistic beam and plasma temperature effects *Phys. Rev.* E **72** 016403
[31] Bret A., Gremillet L. and Bellido J.C. 2007 How really transverse is the filamentation instability? *Phys. Plasmas* **14** 032103
[32] Bret A., Gremillet L., Bénisti D. and Lefebvre E. 2008 Exact relativistic kinetic theory of an electron–beam–plasma system: hierarchy of the competing modes in the system parameter space *Phys. Rev. Lett.* **100** 205008
[33] Bret A., Gremillet L. and Bénisti D. 2010 Exact relativistic kinetic theory of the full unstable spectrum of an electron–beam–plasma system with Maxwell–Jüttner distribution functions *Phys. Rev.* E **81** 036402
[34] Bret A., Gremillet L. and Dieckmann M. 2010 Multidimensional electron beam-plasma instabilities in the relativistic regime *Phys. Plasmas* **17** 120501
[35] Buneman O. 1959 Dissipation of currents in ionized media *Phys. Rev.* **115** 503
[36] Cai H.-B. *et al* 2010 Enhancing the number of high-energy electrons deposited to a compressed pellet via double cones in fast ignition *Phys. Rev. Lett.* **102** 245001
[37] Califano F., Del Sarto D. and Pegoraro F. 2006 Three-dimensional magnetic structures generated by the development of the filamentation (Weibel) instability in the relativistic regime *Phys. Rev. Lett.* **96** 105008
[38] Califano F., Pegoraro F., Bulanov S.V. and Mangeney A. 1998 Kinetic saturation of the Weibel instability in a collisionless plasma *Phys. Rev.* E **57** 7048–59
[39] Campbell R.B. *et al* 2003 *Phys. Plasmas* **10** 4169
[40] Chandrasekhar S. *et al* 1943 *Rev. Mod. Phys.* **15** 1
[41] Chang P.Y., Fiksel G., Hohenberger M., Knauer J.P., Betti R., Marshall F.J., Meyerhofer D.D., Séguin F.H. and Petrasso R.D. 2011 Fusion yield enhancement in magnetized laser-driven implosions *Phys. Rev. Lett.* **107** 035006
[42] Chrisman B., Sentoku Y. and Kemp A.J. 2008 Intensity scaling of hot electron energy coupling in cone-guided fast ignition *Phys. Plasmas* **15** 056309
[43] Cohen B.I., Langdon A.B. and Friedman A. 1982 Implicit time integration of plasma simulation *J. Comput. Phys.* **46** 15
[44] Cohen R.S., Spitzer L. Jr and Routly P.M. 1950 *Phys. Rev.* **80** 230
[45] Cottrill L.A., Langdon A.B., Lasinski B.F., Lund S.M., Molvig K., Tabak M., Town R.P.J. and Williams E.A. 2008 Kinetic and collisional effects on the linear evolution of fast ignition relevant beam instabilities *Phys. Plasmas* **15** 082108
[46] Courtois C., Ash A.D., Chambers D.M., Grundy R.A.D. and Woolsey N.C. 2005 Creation of a uniform high magnetic-field strength environment for laser-driven experiments *J. Appl. Phys.* **98** 054913
[47] Daido H., Miki F., Mima K., Fujita M., Sawai K., Fujita H., Kitagawa Y., Nakai S. and Yamanaka C. 1986 Generation of a strong magnetic field by an intense CO_2 laser pulse *Phys. Rev. Lett.* **56** 846–9
[48] Daligault J. and Dimonte G. 2009 Correlation effects on the temperature-relaxation rates in dense plasmas *Phys. Rev.* E **79** 056403
[49] Davidson R.C., Hammer D.A., Haber I. and Wagner C.E. 1972 Nonlinear development of electromagnetic instabilities in anisotropic plasmas *Phys. Fluids* **15** 317
[50] Davidson R.C. 1972 *Methods in Nonlinear Plasma Theory* (New York: Academic)
[51] Davidson R.C. 1984 Relativistic electron beam-plasma interaction with intense self-fields *Handbook of Plasma Physics* vol 2 ed M.N. Rosenbluth and R.Z. Galeev (Amsterdam: North-Holland)
[52] Davies J.R. 1999 *Phys. Rev.* E **59** 6032
[53] Davies J.R. 2002 *Phys. Rev.* E **65** 026407
[54] Davies J.R. 2003 *Phys. Rev.* E **68** 056404
[55] Davies J.R. 2009 *Plasma Phys. Control. Fusion* **51** 014006
[56] Debayle A., Gremillet L., Honrubia J.J. and d'Humieres E. 2013 Reduction of the fast electron angular dispersion by means of varying-resistivity structured targets *Phys. Plasmas* **20** 013109
[57] Debayle A., Honrubia J.J., d'Humieres E., Tikhonchuk V.T., Micheau S. and Geissler M. 2010 Integrated simulations of ignition scale fusion targets for the HiPER project *J. Phys: Conf. Ser.* **244** 022032
[58] Debayle A., Honrubia J.J., d'Humieres E. and Tikhonchuk V.T. 2010 Characterization of laser-produced fast electron sources for fast ignition *Plasma Phys. Control. Fusion* **52** 124024
[59] Debayle A., Honrubia J.J., d'Humieres E. and Tikhonchuk V.T. 2010 Divergence of laser-driven relativistic electron beams *Phys. Rev.* E **82** 036405
[60] Decyk V.K. 1987 *Int. Conf. on Plasma Physics. Proc. Invited Papers (Kiev, Ukraine)* vol 2 (Singapore: World Scientific) pp 1075–97
[61] Desjarlais M.P. 2001 Practical improvements to the Lee–More conductivity near the metal–insulator transition *Contrib. Plasma Phys.* **41** 267–70
[62] Deutsch C. and Fromy P. 1999 Correlated stopping of relativistic electrons in superdense plasmas *Phys. Plasmas* **6** 3597
[63] Dieckmann M.E. 2009 The filamentation instability driven by warm electron beams: statistics and electric field generation *Plasma Phys. Control. Fusion* **51** 124042

[64] Dimonte G. and Daligault J. 2008 *Phys. Rev. Lett.* **101** 135001
[65] Drouin M., Gremillet L., Adam J.-C. and Héron A. 2010 Particle-in-cell modeling of relativistic laser–plasma interaction with the adjustable-damping, direct implicit method *J. Comput. Phys.* **229** 4781–812
[66] Ellis I.N., Graziani F.R., Glosli J.N., Strozzi D.J., Surh M.P., Richards D.F., Decyk V.K. and Mori W.B. 2011 Studies of particle wake potentials in plasmas *High Energy Density Phys.* **7** 191–6
[67] Epperlein E.M. and Haines M.G. 1986 Plasma transport coefficients in a magnetic field by direct numerical solution of the Fokker–Planck equation *Phys. Fluids* **29** 1029–41
[68] Evans R., Gyorffy B.L., Szabo N. and Ziman J.M. 1973 *The Properties of Liquid Metals* (New York: Wiley)
[69] Fano U. 1956 Atomic theory of electromagnetic interactions in dense materials *Phys. Rev.* **103** 1202–18
[70] Faĭnberg Ya.B., Shapiro V.D. and Shevchenko V.I. 1970 Nonlinear theory of interaction between a 'monochromatic' beam of relativistic electrons and a plasma *Sov. Phys.—JETP* **30** 528–33
[71] Fermi E. 1940 *Phys. Rev.* **57** 485
[72] Ferrell R.A. 1956 Angular dependence of the characteristic energy loss of electrons passing through metal foils *Phys. Rev.* **101** 554–63
[73] Fiore M., Fiúza F., Marti M., Fonseca R.A. and Silva L.O. 2010 Relativistic effects on the collisionless–collisional transition of the filamentation instability in fast ignition *J. Plasma Phys.* **76** 813–32
[74] Fiuza F., Fonseca R.A., Tonge J., Mori W.B. and Silva L.O. 2012 Weibel-instability-mediated collisionless shocks in the laboratory with ultraintense lasers *Phys. Rev. Lett.* **108** 235004
[75] Friedman A., Langdon A.B. and Cohen B.I. 1981 A direct method for implicit particle-in-cell simulation *Comments Plasma Phys. Control. Fusion* **6** 225–36
[76] Fried B.D., Ikemura T., Nishikawa K. and Schmidt G. 1976 Parametric instabilities with finite wavelength pump *Phys. Fluids* **19** 1975
[77] Fried B.D. 1959 Mechanism for instability of transverse plasma waves *Phys. Fluids* **2** 337
[78] Fujioka S. *et al* 2013 Kilotesla magnetic field due to a capacitor-coil target driven by high power laser *Sci. Rep.* **3** 1170
[79] Fujioka S. *et al* 2012 High-energy-density plasmas generation on GEKKO-LFEX laser facility for fast-ignition laser fusion studies and laboratory astrophysics *Plasma Phys. Control. Fusion* **54** 124042
[80] Gasiorowicz S. *et al* 1956 *Phys. Rev.* **101** 922
[81] Glosli J.N., Graziani F.R., More R.M., Murillo M.S., Streitz F.H., Surh M.P., Benedict L.X., Hau-Riege S., Langdon A.B. and London R.A. 2008 Molecular dynamics simulations of temperature equilibration in dense hydrogen *Phys. Rev.* E **78** 025401
[82] Green J.S. *et al* 2008 Effect of laser intensity on fast-electron-beam divergence in solid-density plasmas *Phys. Rev. Lett.* **100** 015003
[83] Gremillet L., Bénisti D., Bret A. and Lefebvre E. 2007 Linear and nonlinear development of oblique beam-plasma instabilities in the relativistic kinetic regime *Phys. Plasmas* **14** 040704
[84] Gremillet L., Bonnaud G. and Amiranoff F. 2002 Filamented transport of laser-generated relativistic electrons penetrating a solid target *Phys. Plasmas* **9** 941–8
[85] Haines M.G., Wei M.S., Beg F.N. and Stephens R.B. 2009 Hot-electron temperature and laser-light absorption in fast ignition *Phys. Rev. Lett.* **102** 045008
[86] Hansen S.B., Isaacs W.A., Sterne P.A., Wilson B.G., Sonnad V. and Young D.A. 2005 Electrical conductivity calculations from the Purgatorio code *Proc. NEDPC (Livermore, CA, USA)* UCRL-PROC-218150
[87] Hao B., Ding W.J., Sheng Z.-M., Ren C., Kong X., Mu J. and Zhang J. 2012 Collisional effects on the oblique instability in relativistic beam-plasma interactions *Phys. Plasmas* **19** 072709
[88] Hao B., Sheng Z.-M. and Zhang J. 2008 Kinetic theory on the current-filamentation instability in collisional plasmas *Phys. Plasmas* **15** 082112
[89] Hewett D.W. and Langdon A.B. 1987 Electromagnetic direct implicit plasma simulation *J. Comput. Phys.* **72** 121–55
[90] Hill J.M., Key M.H., Hatchett S.P. and Freeman R.R. 2005 Beam-Weibel filamentation instability in near-term and fast-ignition experiments *Phys. Plasmas* **12** 082304
[91] Hohenberger M., Chang P.-Y., Fiksel G., Knauer J.P., Betti R., Marshall F.J., Meyerhofer D.D., Séguin F.H. and Petrasso R.D. 2012 Inertial confinement fusion implosions with imposed magnetic field compression using the Omega laser *Phys. Plasmas* **19** 056306
[92] Honda M. and Meyer-ter-Vehn J. 2000 Two-dimensional, particle-in-cell simulations for magnetized transport of ultra-high relativistic currents in plasma *Phys. Plasmas* **7** 1302–8
[93] Honrubia J.J. and Meyer-ter-Vehn J. 2006 Three-dimensional fast electron transport for ignition-scale inertial fusion capsules *Nucl. Fusion* **46** L25–8
[94] Honrubia J.J., Alfonsin C., Alonso L., Perez B. and Cerrada J.A. 2006 Simulations of heating of solid targets by fast electrons *Laser Part. Beams* **24** 217
[95] Honrubia J.J., Kaluza M., Schreiber J., Tsakiris G.D. and Meyer-ter-Vehn J. 2005 Laser-driven fast electron transport in preheated foil targets *Phys. Plasmas* **12** 052708
[96] Honrubia J.J. and Meyer-ter-Vehn J. 2009 Fast ignition of fusion targets by laser-driven electrons *Plasma Phys. Control. Fusion* **51** 014008
[97] Honrubia J.J. 1993 A synthetically accelerated scheme for radiative transfer calculations *J. Quant. Spectrosc. Radiat. Transfer* **49** 491
[98] Humphries S. 1990 *Charged Particle Beams* (New York: Wiley Interscience)
[99] Ichimaru S. 1973 *Basic Principles of Plasma Physics* (Reading, MA: Benjamin)
[100] International Commission on Radiation Units and Measurements 1984 Stopping powers for electrons and positrons *Technical Report* 37, Bethesda, MD, USA
[101] Joachain C.J. 1987 *Quantum Collision Theory* 3rd edn (Amsterdam: North-Holland)
[102] Johzaki T., Nakao Y. and Mima K. 2009 Fokker–Planck simulations for core heating in subignition cone-guiding fast ignition targets *Phys. Plasmas* **16** 062706
[103] Johzaki T. *et al* 2009 Core heating properties in FIREX-I—influence of cone tip *Plasma Phys. Control. Fusion* **51** 014002
[104] Johzaki T. *et al* 2011 Pre-plasma effects on core heating and enhancing heating efficiency by extended double cone for FIREX *Nucl. Fusion* **51** 073022
[105] Jüttner F. 1911 Das Maxwellsche Gesetz der Geschwindigkeitsverteilung in der Relativtheorie *Ann. Phys.* **339** 856–82
[106] Karmakar A., Kumar N., Pukhov G., Shvets A. and Polomarov O. 2008 Three-dimensional filamentary structures of a relativistic electron beam in fast ignition plasmas *Phys. Plasmas* **15** 120702
[107] Karmakar A., Kumar N., Pukhov A., Polomarov O. and Shvets G. 2009 Detailed particle-in-cell simulations on the transport of a relativistic electron beam in plasmas *Phys. Rev.* E **80** 016401
[108] Karmakar A., Kumar N., Shvets G., Polomarov O. and Pukhov A. 2008 Collision-driven negative-energy waves and the Weibel instability of a relativistic electron beam in a quasineutral plasma *Phys. Rev. Lett.* **101** 255001
[109] Kar S. *et al* 2009 *Phys. Rev. Lett.* **102** 055001
[110] Kato T.N. 2005 Saturation mechanism of the Weibel instability in weakly magnetized plasmas *Phys. Plasmas* **12** 080705

[111] Kemp A.J. and Divol L. 2012 Interaction physics of multipicosecond petawatt laser pulses with overdense plasma *Phys. Rev. Lett.* **109** 195005

[112] Kemp A.J., Sentoku Y., Sotnikov V. and Wilks S.C. 2006 Collisional relaxation of superthermal electrons generated by relativistic laser pulses in dense plasma *Phys. Rev. Lett.* **97** 235001

[113] Khudik V., Kaganovich I. and Shvets G. 2012 Halo formation and self-pinching of an electron beam undergoing the Weibel instability *Phys. Plasmas* **19** 103106

[114] Kluge T., Cowan T., Debus A., Schramm U., Zeil K. and Bussmann M. 2011 Electron temperature scaling in laser interaction with solids *Phys. Rev. Lett.* **107** 205003

[115] Knauer J.P. *et al* 2010 Compressing magnetic fields with high-energy lasers *Phys. Plasmas* **17** 056318

[116] Kruer W.L. and Estabrook K. 1985 $\boldsymbol{J} \times \boldsymbol{B}$ heating by very intense laser light *Phys. Fluids* **28** 430–2

[117] Lampe M. and Sprangle P. 1975 Saturation of the relativistic two-stream instability by electron trapping *Phys. Fluids* **18** 475–81

[118] Lancaster K.L. *et al* 2007 *Phys. Rev. Lett.* **98** 125002

[119] Langdon A.B. and Barnes D.C. 1985 Direct implicit plasma simulation *Multiple Time Scales* ed J.U. Brackbill and B.I. Cohen (Orlando, FL: Academic) pp 335–75

[120] Larson D., Tabak M. and Ma T. 2010 Hybrid simulations for magnetized fast ignition targets and analyzing cone-wire experiments *Bull. Am. Phys. Soc.* **55**

[121] Lazar M., Schlickeiser R., Poedts S. and Tautz R.C. 2008 Counterstreaming magnetized plasmas with kappa distributions: I. Parallel wave propagation *Mon. Not. R. Astron. Soc.* **390** 168

[122] Lee R. and Lampe M. 1973 Electromagnetic instabilities, filamentation, and focusing of relativistic electron beams *Phys. Rev. Lett.* **31** 1390–3

[123] Lee Y.T. and More R.M. 1984 An electron conductivity model for dense plasmas *Phys. Fluids* **27** 1273–86

[124] Macfarlane J.J. *et al* 2006 *J. Quant. Spectrosc. Radiat. Transfer* **99** 381

[125] Malkin V.M. and Fisch N.J. 2002 Collective deceleration of relativistic electrons precisely in the core of an inertial-fusion target *Phys. Rev. Lett.* **89** 125004

[126] Marinak M.M., Kerbel G.D., Gentile N.A., Jones O., Munro D., Pollaine S., Dittrich T.R. and Haan S.W. 2001 Three-dimensional Hydra simulations of National Ignition Facility targets *Phys. Plasmas* **8** 2275–80

[127] Mart'yanov V.Yu., Kocharovsky V.V. and Kocharovsky Vl.V. 2008 Saturation of relativistic Weibel instability and the formation of stationary current sheets in collisionless plasmas *JETP* **107** 1225

[128] Mason R.J. 1981 Implicit moment particle simulation of plasmas *J. Comput. Phys.* **41** 233–44

[129] Mason R.J. 1987 An electromagnetic field algorithm for 2D implicit plasma simulation *J. Comput. Phys.* **71** 429–73

[130] Mason R.J. 2006 Heating mechanisms in short-pulse laser-driven cone targets *Phys. Rev. Lett.* **96** 035001

[131] Medvedev M.V., Fiore M., Fonseca R.A., Silva L.O. and Mori W.B. 2005 *Astrophys. J.* **618** L75

[132] Medvedev M.V. and Loeb A. 1999 Generation of magnetic fields in the relativistic shock of gamma ray burst sources *Astrophys. J.* **526** 697–706

[133] Miller R.B. 1982 *An Introduction to the Physics of Intense Charged Particle Beams* (New York: Plenum)

[134] Mima K. and Nishikawa K. 1984 Parametric instabilities and wave dissipation in plasmas *Handbook of Plasma Physics* vol 2 ed M.N. Rosenbluth and R.Z. Galeev (Amsterdam: North-Holland)

[135] Molvig K. 1975 Filamentation instability of a relativistic electron beam *Phys. Rev. Lett.* **35** 1504–7

[136] More R.M. 1985 *Proc. 29th St. Andrews Scottish Universities Summer School in Physics (Fife, Scotland)* (Edinburgh: SUSSP Publications) pp 157–214

[137] Morse R.L. and Nielson C.W. 1969 Numerical simulation of warm two-beam plasma *Phys. Fluids* **12** 2418–25

[138] Mosher D 1975 Interactions of relativistic electron beams with high atomic-number plasmas *Phys. Fluids* **18** 846–57

[139] Mott N.F. 1929 *Proc. R. Soc.* A **124** 425

[140] Motz J.W. *et al* 1964 *Rev. Mod. Phys.* **36** 881

[141] Muschietti L. 1990 Electron beam formation and stability *Sol. Phys.* **130** 201–28

[142] Nakamura T. *et al* 2007 Optimization of cone target geometry for fast ignition *Phys. Plasmas* **14** 103105

[143] Nicolaï Ph., Feugeas J.-L., Regan C., Olazabal-Loumé M., Breil J., Dubroca B., Morreeuw J.-P. and Tikhonchuk V. 2011 Effect of the plasma-generated magnetic field on relativistic electron transport *Phys. Rev.* E **84** 016402

[144] Norreys P.A. *et al* 2009 Recent fast electron energy transport experiments relevant to fast ignition inertial fusion *Nucl. Fusion* **49** 104023

[145] Okada T. and Niu K. 1980 Electromagnetic instability and stopping power of plasma for relativistic electron beams *J. Plasma Phys.* **23** 423–32

[146] Okada T. and Ogawa K. 2007 Saturated magnetic fields of Weibel instabilities in laser–plasma interactions *Phys. Plasmas* **14** 072702

[147] O'Neil T.M., Winfrey J.H. and Malmberg J.H. 1971 Nonlinear interaction of a small cold beam and a plasma *Phys. Fluids* **14** 1204–12

[148] Opher M., Morales G.J. and Leboeuf J.N. 2002 Krook collisional models of the kinetic susceptibility of plasmas *Phys. Rev.* E **66** 016407

[149] Ordonez C.A. *et al* 1994 *Phys. Plasmas* **1** 2515

[150] Pegoraro F., Bulanov S.V., Califano F. and Lontano M. 1996 Nonlinear development of the Weibel instability and magnetic field generation in collisionless plasmas *Phys. Scr.* T **63** 262–5

[151] Perez F. *et al* 2011 *Phys. Rev. Lett.* **107** 065004

[152] Pérez F., Gremillet L., Decoster A., Drouin M. and Lefebvre E. 2012 Improved modeling of relativistic collisions and collisional ionization in particle-in-cell codes *Phys. Plasmas* **19** 083104

[153] Pines D. 1953 A collective description of electron interactions: IV. Electron interaction in metals *Phys. Rev.* **92** 626–36

[154] Pines D. and Bohm D. 1952 *Phys. Rev.* **85** 338

[155] Ping Y. *et al* 2008 Absorption of short laser pulses on solid targets in the ultrarelativistic regime *Phys. Rev. Lett.* **100** 085004

[156] Polomarov O., Kaganovich I. and Shvets G. 2008 Merging of super-Alfvénic current filaments during collisionless Weibel instability of relativistic electron beams *Phys. Rev. Lett.* **101** 175001

[157] Pukhov A. and Meyer-ter-Vehn J. 1996 Relativistic magnetic self-channeling of light in near-critical plasmas. Three-dimensional PIC simulation *Phys. Rev. Lett.* **76** 3975–8

[158] Quesnel B. and Mora P. 1998 Theory and simulation of the interaction of ultraintense laser pulses with electrons in vacuum *Phys. Rev.* E **58** 3719–32

[159] Radha P.B. *et al* 2005 Multidimensional analysis of direct-drive, plastic-shell implosions on OMEGA *Phys. Plasmas* **12** 056307

[160] Ramakrishna B. *et al* 2010 *Phys. Rev. Lett.* **105** 135001

[161] Ren C., Tzoufras M., Tonge J., Mori W.B., Tsung F.S., Fiore M., Fonseca R.A., Silva L.O., Adam J.C. and Héron A. 2006 A global simulation for laser-driven MeV electrons in 50 μm Fast Ignition targets *Phys. Plasmas* **13** 056308

[162] Scott R.H.H. *et al* 2012 *Phys. Rev. Lett.* **109** 015001

[163] Rinker G.A. 1988 Systematic calculations of plasma transport coefficients for the periodic table *Phys. Rev.* A **37** 1284–97

[164] Roberts K.V. and Berk H.L. 1967 Nonlinear evolution of a two-stream instability *Phys. Rev. Lett.* **19** 297–300

[165] Robinson A.P.L. *et al* 2008 *Plasma Phys. Control. Fusion* **50** 065019
[166] Robinson A.P.L. *et al* 2008 *Phys. Rev. Lett.* **100** 025002
[167] Robinson A.P.L., Key M.H. and Tabak M. 2012 *Phys. Rev. Lett.* **108** 125004
[168] Robinson A.P.L. and Sherlock M. 2007 Magnetic collimation of fast electrons produced by ultraintense laser irradiation by structuring the target composition *Phys. Plasmas* **14** 083105
[169] Robinson A.P.L. and Schmitz H. 2013 *Phys. Plasmas* **20** 062704
[170] Rozsnyai B.F. 2008 Electron scattering in hot/warm plasmas *High Energy Density Phys.* **4** 64–72
[171] Rudakov L.I. 1971 Collective slowing down of an intense beam of relativistic electrons in a dense plasma target *Sov. Phys.—JETP* **32** 1134–40
[172] Sakai J., Saito S., Mae H., Farina D., Lontano M., Califano F., Pegoraro F. and Bulanov S.V. 2002 Ion acceleration, magnetic field line reconnection and multiple filament coalescence of a relativistic electron beam in a plasma *Phys. Plasmas* **9** 2959
[173] Sakawa Y. *et al* 2010 *J. Phys.: Conf. Ser.* **244** 042012
[174] Schaefer-Rolffs U., Lerche I. and Schlickeiser R. 2006 The relativistic kinetic Weibel instability: general arguments and specific illustrations *Phys. Plasmas* **13** 012107
[175] Schmitz H., Lloyd R. and Evans R.G. 2012 Collisional particle-in-cell modelling of the generation and control of relativistic electron beams produced by ultra-intense laser pulses *Plasma Phys. Control. Fusion* **54** 085016
[176] Sentoku Y., Mima K., Kaw P. and Nishikawa K. 2003 Anomalous resistivity resulting from MeV-electron transport in overdense plasma *Phys. Rev. Lett.* **90** 155001
[177] Sentoku Y., Mima K., Kojima S. and Ruhl H. 2000 Magnetic instability by the relativistic laser pulses in overdense plasmas *Phys. Plasmas* **7** 689–95
[178] Shay H.D., Amendt P., Clark D., Ho D., Key M., Koning J., Marinak M., Strozzi D. and Tabak M. 2012 Implosion and burn of fast ignition capsules—calculations with HYDRA *Phys. Plasmas* **19** 092706
[179] Sherlock M. 2009 Universal scaling of the electron distribution function in one-dimensional simulations of relativistic laser–plasma interactions *Phys. Plasmas* **16** 103101
[180] Shiraga H. *et al* 2011 Fast ignition integrated experiments with GEKKO and LFEX lasers *Plasma Phys. Control. Fusion* **53** 124029
[181] Shkarofsky I.P., Johnston T.W. and Bachynski M.P. 1966 *The Particle Kinetics of Plasmas* (Reading, MA: Addison-Wesley)
[182] Shvets G., Polomarov O., Khudik V., Siemon C. and Kaganovich I. 2009 Nonlinear evolution of the Weibel instability of relativistic electron beams *Phys. Plasmas* **16** 056303
[183] Silva L.O., Fonseca R.A., Tonge J.W., Mori W.B. and Dawson J.M. 2002 On the role of the purely transverse Weibel instability in fast ignitor scenarios *Phys. Plasmas* **9** 2458
[184] Silva L.O. 2006 Physical problems (Microphysics) in relativistic plasma flows *Relativistic Jets: The Common Physics of AGN, Microquasars, and Gamma-Ray Bursts* (*American Institute of Physics Conference Series* vol 856) ed P.A. Hughes and J.N. Bregman pp 109–28
[185] Singhaus H.E. 1964 Temperature effects on the electrostatic instability for an electron beam penetrating a plasma *Phys. Fluids* **7** 1534
[186] Solodov A.A., Anderson K.S., Betti R., Gotcheva V., Myatt J., Delettrez J.A., Skupsky S., Theobald W. and Stoeckl C. 2008 Simulations of electron transport and ignition for direct-drive fast-ignition targets *Phys. Plasmas* **15** 112702
[187] Solodov A.A., Anderson K.S., Betti R., Gotcheva V., Myatt J., Delettrez J.A., Skupsky S., Theobald W. and Stoeckl C. 2009 Integrated simulations of implosion, electron transport, and heating for direct-drive fast-ignition targets *Phys. Plasmas* **16** 056309
[188] Solodov A.A., Betti R., Anderson K.S., Myatt J.F., Theobald W. and Stoeckl C. 2010 *Bull. Am. Phys. Soc.* **55** 69
[189] Solodov A.A. and Betti R. 2008 Stopping power and range of energetic electrons in dense plasmas of fast-ignition fusion targets *Phys. Plasmas* **15** 042707
[190] Solodov A.A. *et al* 2007 Gain curves and hydrodynamic simulations of ignition and burn for direct-drive fast-ignition fusion targets *Phys. Plasmas* **14** 062701
[191] Solodov A.A. *et al* 2010 *Code comparison session at Fusion Science Center for Extreme States of Matter meeting on Electron Divergence in Fast Ignition (Livermore, CA)*
[192] Stephens R. *et al* 2004 K_α fluorescence measurement of relativistic electron transport in the context of fast ignition *Phys. Rev.* E **69** 066414
[193] Sterne P.A., Hansen S.B., Wilson B.G. and Isaacs W.A. 2007 Equation of state, occupation probabilities and conductivities in the average atom Purgatorio code *High Energy Density Phys.* **3** 278–82
[194] Sternheimer R.M. *et al* 1984 *At. Data Nucl. Data Tables* **30** 261
[195] Sternheimer R.M. 1952 The density effect for the ionization loss in various materials *Phys. Rev.* **88** 851–9
[196] Strozzi D.J., Tabak M., Larson D.J., Divol L., Kemp A.J., Bellei C., Marinak M.M. and Key M.H. 2012 Fast-ignition transport studies: realistic electron source, integrated particle-in-cell and hydrodynamic modeling, imposed magnetic fields *Phys. Plasmas* **19** 072711
[197] Sudan R.N. 1984 Collective beam-plasma interaction (*Handbook of Plasma Physics* vol 2) ed M.N. Rosenbluth and R.Z. Galeev (Amsterdam: North-Holland)
[198] Tabak M., Hammer J., Glinsky M.E., Kruer W.L., Wilks S.C., Woodworth J., Michael Campbell E., Perry M.D. and Mason R.J. 1994 Ignition and high gain with ultrapowerful lasers *Phys. Plasmas* **1** 1626–34
[199] Tabak M. *et al* 2005 Review of progress in fast ignition *Phys. Plasmas* **12** 057305
[200] Tabak M., Shay H., Strozzi D., Divol L., Grote D., Larson D., Nuckolls J. and Zimmerman G. 2010 Assembling fuel for fast ignition in cone-shell targets for good transport coupling *Bull. Am. Phys. Soc.* **55**
[201] Taguchi T., Antonsen T.M. Jr., Liu C.S. and Mima K. 2001 Structure formation and tearing of an MeV cylindrical electron beam in a laser-produced plasma *Phys. Rev. Lett.* **86** 5055–8
[202] Tatarakis M. *et al* 1998 Plasma formation on front and rear of plastic targets due to high intensity laser-generated fast electrons *Phys. Rev. Lett.* **81** 999–1002
[203] Tautz R.C. and Schlickeiser R. 2005 *Phys. Plasmas* **12** 122901
[204] Tautz R.C. and Schlickeiser R. 2006 *Phys. Plasmas* **13** 062901
[205] Tautz R.C. and Shalchi A. 2008 On particle transport in Weibel generated fields *Phys. Plasmas* **15** 052304
[206] Thode L.E. and Sudan R.N. 1975 Plasma heating by relativistic electron beams: I. Two-stream instability *Phys. Fluids* **18** 1552–63
[207] Thode L.E. 1976 Energy lost by a relativistic electron beam due to two-stream instability *Phys. Fluids* **19** 305–15
[208] Thomas A.G.R., Tzoufras M., Robinson A.P.L., Kingham R.J., Ridgers C.P., Sherlock M. and Bell A.R. 2012 A review of Vlasov–Fokker–Planck numerical modeling of inertial confinement fusion plasma *J. Comput. Phys.* **231** 1051–79
[209] Thoma C. *et al* 2011 *Phys. Plasmas* **18** 103507

[210] Tonge J., May J., Mori W.B., Fiuza F., Martins S.F., Fonseca R.A., Silva L.O. and Ren C. 2009 A simulation study of fast ignition with ultrahigh intensity lasers *Phys. Plasmas* **16** 056311
[211] Tzoufras M., Ren C., Tsung F.S., Tonge J.W., Mori W.B., Fiore M., Fonseca R.A. and Silva L.O. 2006 Space charge effects in the current filamentation or Weibel instability *Phys. Rev. Lett.* **96** 105002
[212] van den Oord G.H. 1990 *Astronom. Astrophys.* **234** 496–518
[213] Velikovich A.L. 2012 Tutorial: magnetic flux compression in plasmas followed by Z-pinch, HED magnetic fields *Bull. Am. Phys. Soc.* **57**
[214] Villasenor J. and Buneman O. 1992 Rigorous charge conservation for local electromagnetic field solvers *Comput. Phys. Commun.* **69** 306
[215] Wang C.-L., Joyce G. and Nicholson D.R. 1981 *J. Plasma Phys.* **25** 225–31
[216] Weibel E.S. 1959 Spontaneous growing transverse waves in a plasma due to an anisotropic velocity distribution *Phys. Rev. Lett.* **2** 83–4
[217] Welch D.R., Rose D.V., Oliver B.V. and Clark R.E. 2001 Simulation techniques for heavy ion fusion chamber transport *Nucl. Instrum. Methods Phys. Res.* A **464** 134
[218] Welch D.R. *et al* 2006 *Phys. Plasmas* **13** 063105
[219] Wilks S.C., Kruer W.L., Tabak M. and Langdon A.B. 1992 Absorption of ultra-intense laser pulses *Phys. Rev. Lett.* **69** 1383–6
[220] Wilson B., Sonnad V., Sterne P. and Isaacs W. 2006 Purgatorio—a new implementation of the Inferno algorithm *J. Quant. Spectrosc. Radiat. Transfer* **99** 658–79
[221] Wright T.P. and Hadley G.R. 1975 Relativistic distribution functions and applications to electron beams *Phys. Rev.* A **12** 686–97
[222] Yabuuchi T., Das A., Kumar G.R., Habara H., Kaw P.K., Kodama R., Mima K., Norreys P.A., Sengupta S. and Tanaka K.A. 2009 Evidence of anomalous resistivity for hot electron propagation through a dense fusion core in fast ignition experiments *New J. Phys.* **11** 093031
[223] Yang T.-Y.B., Arons J. and Langdon A.B. 1994 Evolution of the Weibel instability in relativistically hot electron–proton plasmas *Phys. Plasmas* **1** 3059–77
[224] Yokota T., Nakao Y., Johzaki T. and Mima K. 2006 Two-dimensional relativistic Fokker–Planck model for core plasma heating in fast ignition targets *Phys. Plasmas* **13** 022702
[225] Yoon P.H. and Davidson R.C. 1987 Exact analytical model of the classical Weibel instability in a relativistic anisotropic plasma *Phys. Rev.* A **35** 2718–21
[226] Yoon P.H. 1989 Electromagnetic Weibel instability in a fully relativistic bi-Maxwellian plasma *Phys. Fluids* B **1** 1336–8
[227] Yoon P.H. 2007 Relativistic Weibel instability *Phys. Plasmas* **14** 024504
[228] Zaitsev V.V., Kunilov M.V., Mityakov N.A. and Rapoport V.O. 1974 Generation of type III radio bursts by electron fluxes having a large injection time *Sov. Astron.* **18** 147
[229] Ziman J.M. 1961 *Phil. Mag.* **6** 1013